



Chair of Petroleum and Geothermal Energy Recovery

Master's Thesis



Electric Submersible Pump Behavior with
Viscous Fluids

Hans-Peter Pratscher, BSc

September 2019

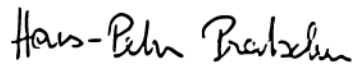
EIDESSTATTLICHE ERKLÄRUNG

Ich erkläre an Eides statt, dass ich diese Arbeit selbständig verfasst, andere als die angegebenen Quellen und Hilfsmittel nicht benutzt, und mich auch sonst keiner unerlaubten Hilfsmittel bedient habe.

Ich erkläre, dass ich die Richtlinien des Senats der Montanuniversität Leoben zu "Gute wissenschaftliche Praxis" gelesen, verstanden und befolgt habe.

Weiters erkläre ich, dass die elektronische und gedruckte Version der eingereichten wissenschaftlichen Abschlussarbeit formal und inhaltlich identisch sind.

Datum 03.09.2019



Unterschrift Verfasser/in
Hans-Peter, Pratscher
Matrikelnummer: 01435139

Danksagung / Acknowledgement

This thesis was composed at the Chair for Petroleum and Geothermal Energy Recovery at the Montanuniversität Leoben for OMV as the contracting company. I want to thank the following persons for their support:

First, I have to thank Dipl.-Ing. Dipl.-Ing. Dr. mont. Clemens Langbauer for giving me the chance to commerce this thesis and for his helpful advice and dedication.

At second I want to thank Andreas Öfler, for his time and effort working with me at the testing facility.

I also wish to thank my supervisor, Dipl.-Ing. Alexandru-Cosmin Ciufu, who was my main contact for company related questions and was always encouraged to help me.

Furthermore, I have to thank all other stakeholders from OMV, who have been involved in this project and contributed their time and knowledge.

Special thanks are addressed to the Department of Polymer Engineering, PCCL and the Institute of Electrical engineering for their support.

I owe a great gratitude to my parents, Doris and Robert, who supported me my whole life in all respect.

Finally, many thanks are addressed to my sister Ines, my grandparents, and all my other relatives and friends for their support and motivating attitude.

Kurzfassung

Das Ziel dieser Arbeit war es, die Leistung von Tauchkreiselpumpen unter polymerhaltigen (nicht-newtonischen) Flüssigkeitsbedingungen zu untersuchen. Die Studie konzentriert sich auf die Leistungsreduzierung der Pumpe, die mechanische Scherung von polymeren Molekülketten in der Pumpe und die Anwendbarkeit bestehender Korrelationen.

Zwei verschiedene Tauchkreiselpumpen (82 Stufen und 7 Stufen) wurden in einem neu errichteten Pumpenteststand getestet. Die Messungen umfassten Druck, Durchfluss, Drehmoment, Drehzahl und Temperatur. Zunächst wurde die Leistung der Pumpe bei Wasser, konstantem Ansaugdruck und konstanter Drehzahl, mit der Katalogkurve des Herstellers verglichen. Die erhaltenen Ergebnisse wurden dann als Grundlage für die viskosen Experimente verwendet. Zusätzlich wurden während aller Experimente Flüssigkeitsproben entnommen und anschließend analysiert.

Die Experimente wurden für drei Polymerkonzentrationen unter drei verschiedenen Drehzahlen durchgeführt. Die Tests zeigten, dass die Leistungsminderungsfaktoren größer sind als erwartet obwohl eine niedrigviskose Flüssigkeit vorhanden war. Es wird vermutet, dass das nicht-newtonische Flüssigkeitsverhalten für diesen erheblichen Leistungsverlust verantwortlich ist. Darüber hinaus ist auch das Anlaufmoment für die polymerhaltige Flüssigkeit deutlich höher. Die mechanische Scherung der molekularen Polymerketten war im Gegensatz zu den Erwartungen jedoch nur gering. Diese Beobachtung könnte durch die während der Experimente herrschenden Flüssigkeitsbedingungen beeinflusst worden sein. Zuletzt, vergleicht man die experimentelle Leistung mit bestehenden Korrelationen, kann man sagen, dass diese nicht für die gepumpte nicht-newtonische Flüssigkeit Geltung finden.

Die Neuheit dieser Experimente war das Testen einer, mit 82 Stufen, sehr leistungsstarken Tauchkreiselpumpe mit einer nicht-newtonschen Flüssigkeit, um deren Pumpenleistung und Schereffekte zu untersuchen.

Abstract

The objective of this work was to investigate electric submersible pumps performance within polymer-laden (non-Newtonian) fluid conditions. The study focuses on the pump performance derating, mechanical shearing of polymer molecular chains in the pump, and the applicability of existing correlations.

Two different ESPs (82 stages and 7 stages) were tested in a newly-build Pump Testing Facility. The measurements included pressure, flow rate, torque, rotational speed, and temperature. First, the pump's experimental water performance under constant intake pressure and constant rotational speed were compared to the manufacturer's catalog curves. The obtained performance was then used as the basis for the viscous experiments. Additionally, fluid samples were taken during all tests and were subsequently analyzed.

The experiments were conducted for three polymer concentrations and three rotational speeds. The tests showed that the performance derating factors are much higher than expected, although a low viscous fluid was present. Most likely, the non-Newtonian fluid behavior was responsible for this substantial performance loss. Moreover, also the startup torque is significantly higher for the polymer-laden liquid. Mechanical shearing of the molecular polymer chains was minor. The fluid conditions present during the experiments might have affected these observations. Lastly, when comparing the experimental performance data with existing correlations, it can be said that they do not hold for the non-Newtonian fluid pumped.

The novelty of those experiments was the testing of a powerful 82-stage electric submersible pump using a non-Newtonian fluid, in order to investigate the pump performance and fluid shearing effects.

Table of Content

	Page
1 INTRODUCTION.....	1
2 LITERATURE REVIEW	3
2.1 ESP and EOR Applications in the Industry	3
2.2 Characteristics of Polymer-laden Fluids and Microemulsions	6
2.3 API RP 11S2 “Electric Submersible Pump Testing”	15
2.4 ESP Start Characteristics	19
2.5 Performance Prediction for Newtonian Fluids	19
2.6 Performance Prediction for Non-Newtonian Fluids	29
2.7 Polymer Effects and Expectations on the Pump Performance.....	31
3 METHODOLOGY.....	33
3.1 Experimental Setup (Pump Test Facility).....	33
3.2 Experimental Program	34
3.3 Data Acquisition	38
3.4 Pump Performance Curves.....	39
3.5 Data Processing.....	39
4 RESULTS	40
4.1 Sensitivity Analysis – Intake Pressure with Water.....	40
4.2 Reference Pump Performance Curves with Water	41
4.3 Pump Performance Curves for viscous Fluids	47
4.4 Dynamic Viscosity Measurements	55
4.5 Investigation of Stage Degradation	57
4.6 Polymer Loop Circulation	61
5 EVALUATION	65
5.1 Intake Pressure Analysis	65
5.2 Derating Factors for polymer-laden Fluids	65
5.3 Input versus Output Viscosities.....	66
5.4 Experiments versus Empirical Correlations	68
5.5 Derating Curves for Head Correction.....	69
6 CONCLUSION	73
REFERENCES	74

LIST OF TABLES	78
LIST OF FIGURES	79
ABBREVIATIONS	84
NOMENCLATURE	85
APPENDICES	86
Appendix A – Pump Test Facility.....	86
Appendix B – Electric Submersible Pumps	90
Appendix C – Additional Pump Test Plots.....	95
Appendix D – Rheology Measurements	106
Appendix E – Polymer Solution Preparation and Transport	112
Appendix F – Pump Testing Table	113

1 Introduction

In general, reservoirs comprising insufficient pressure to produce the hydrocarbons naturally use artificial lifting systems. About one-half of the world's two million operated wells use artificial lifting methods. Therefore, different kinds of pumping systems play an essential role in the modern oil and gas industry. Electric submersible pumps (ESPs) are one type of them. Although sucker road pumps remain the most used system by the number of units, ESPs are in the first place in terms of worldwide market share by product revenue (Grand View Research 2017).

One problem with ESPs is that manufacturers usually test their pumps only with fresh water. However, the pump performance is prone to change when used with fluids with much higher viscosities than water. For example, such viscous fluids are polymer-laden fluids used in enhanced oil recovery, but also emulsions are part of this group. The resulting performance degradation would cause a lower production volume than expected with water. Therefore, it is crucial for operators to know the resulting performance loss and subsequently adjust the number of stages during the design process.

There are a few correlations for viscous fluid effects on centrifugal pump performance degradation, explained in Chapters 0 to 2.7. Most of them are related to oil or other Newtonian liquids. In the case of non-Newtonian fluids, even less literature is available, and most of the publications are modified Hydraulic Institute Method approaches. The main problem with non-Newtonian fluids is their complex flow behavior compared to Newtonian liquids. Figure 1 shows, for example, the head degradation of a higher viscous Newtonian fluid (a) and a possible head curve of a non-Newtonian shear thinning fluid (b).

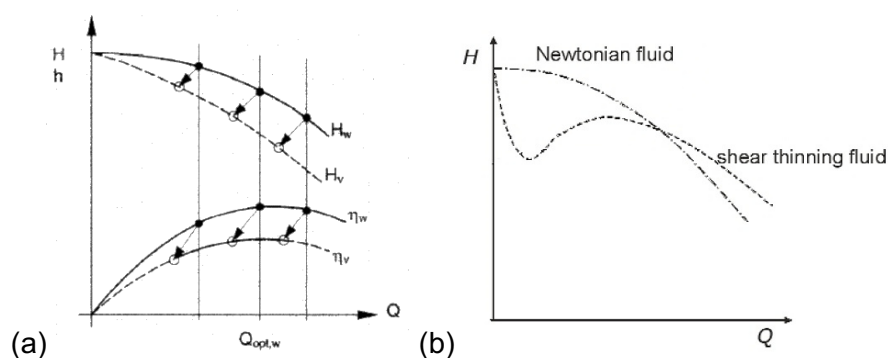


Figure 1: (a) Head degradation of a Newtonian fluid¹ (b) and a non-Newtonian fluid²

¹ Gülich, J. F. 1999. Pumping highly viscous fluids with centrifugal pumps — Part 1. *World Pumps* 1999(395):30–34.

² Pullum, L., L. Graham, and M. Rudman. 2007. Centrifugal pump performance calculation for homogeneous and complex heterogeneous suspensions. *The Journal of The Southern African Institute of Mining and Metallurgy* 107:373–379. [online] URL: https://journals.co.za/content/saimm/107/6/AJA0038223X_3327.

Altogether it can be said that there is no universal correlation for viscous performance degradation, which can be used for random pump types (Morrison et al. 2018). Hence, The main objective of the thesis is to investigate the performance degradation in electric submersible pumps due to highly viscous fluids. In an electric submersible pump test facility, we conducted experiments with different polymer mixtures. The generated data were analyzed and then evaluated. Also, existing correlations for performance prediction are compared with the experimental data to prove or refute their reliability. Furthermore, for the polymeric fluid, the evaluation of molecular breakdown due to shear forces within the pump was part of the investigation.

2 Literature Review

This chapter gives a brief overview of electric submersible pumps and the occurrence of viscous fluids in the industry. Additionally, the fundamental characteristics and rheological behavior of polymer-laden liquids and emulsions are explained. Furthermore, the state-of-the-art industry standard for ESP testing is discussed in detail. The last part of this chapter summarizes common industry models correlations and research regarding pump performance correction.

2.1 ESP and EOR Applications in the Industry

The major advantages of ESPs are the capability of producing large volumes of liquid, the minor environmental footprint and the usage in deviated wells. Some disadvantages, for example, are complications with the electrical power connection downhole or issues in the presence of free gas (Takács 2009). A typical ESP installation consists of the following components shown in Figure 2.

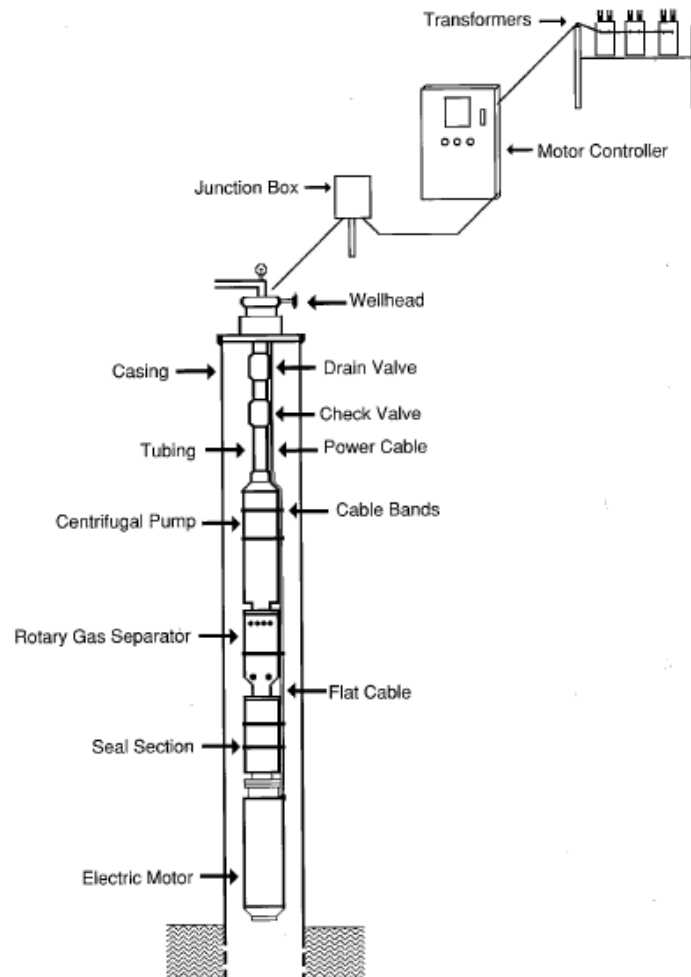


Figure 2: Schematic illustration of an electric submersible pump installation¹

¹ Centrilift. 1997. *Submersible Pump Handbook*. 6th edition, Claremore, Oklahoma.

From bottom to top, we see an asynchronous motor, which is a three-phase induction motor that drives the pump (Takács 2009). At 60 Hz power, the engine runs approximately at 3,500-RPM operation speed compared to the 3,600-RPM synchronous speed (Clegg and Lake 2007). A cable reaching from the surface down to the motor provides the electric power. In many cases, the installation includes a variable speed drive (VSD), which allows controlling the pump's rotational speed. The next component atop of the motor is the seal chamber section, also called "protector." The seal chamber functions are to protect the engine against the reservoir fluids and ensure pressure equalization between the motor interior and the wellbore. Moreover, it absorbs the pump's axial thrust (Clegg and Lake 2007). The next component is the intake, located between the seal chamber and the pump section. An additional gas separator should be integrated if a high percentage of free gas is expected (Takács 2009).

The pump section is a multi-stage centrifugal pump. Every single stage consists of a stator and a rotor, shown in Figure 3. Commonly, the stator is called "diffuser" and the rotating part "impeller" (Takács 2009). In the oil industry, we usually use radial or mixed flow stages, which are distinguished by the impeller and diffuser design (Clegg and Lake 2007). Another pump type distinction is between the handling of the axial thrust. In a compression pump, the main thrust bearing in the protector carries the entire axial load. In contrast, in a floater pump, the washer pads located at each diffuser take the majority of the axial forces (Takács 2009).

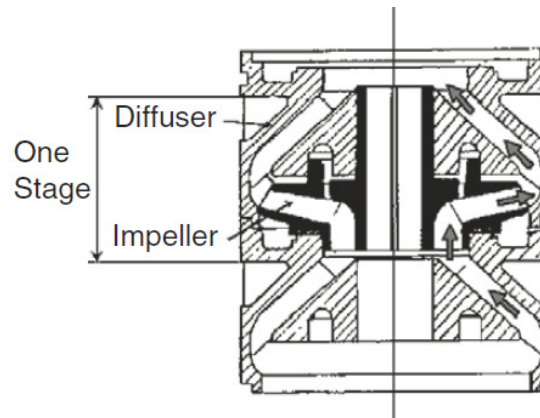


Figure 3: Electric submersible pump stage²

The basic principle of a centrifugal pump stage can be explained as follows. The wellbore fluid enters the impeller, where the impeller vanes increase the fluid velocity due to the high rotational speed. This high kinetic energy fluid is then converted into pressure energy within the diffuser. Then the fluid enters the next stage, and the process repeats itself while each stage adds a certain pressure increment, developing the total pump head (Takács 2009).

² Takács, G. 2009. *Electrical submersible pumps manual: Design, operations, and maintenance*. Gulf Professional Publ./Elsevier, Amsterdam.

The energy conversion follows Bernoulli's principle, assisted by the increased area of the diffuser.

A schematic pump performance curve is shown in Figure 4. The actual pump curve is the theoretical head curve reduced by friction (hydraulic) losses, shock losses, and leakage losses. One conventional notation associated with centrifugal pump performance is using a pump “head” as a performance indicator, rather than a pressure value. The head is simply the pressure differential produced by the pump divided by gravitational acceleration and the liquid density. Hence, the developed head is constant and independent of the fluid for a given pump (Takács 2009). However, the developed head is prone to change when pumping fluids with significant larger viscosity than water. This head degradation issue is explained in a later paragraph and is one of the primary investigations of this thesis.

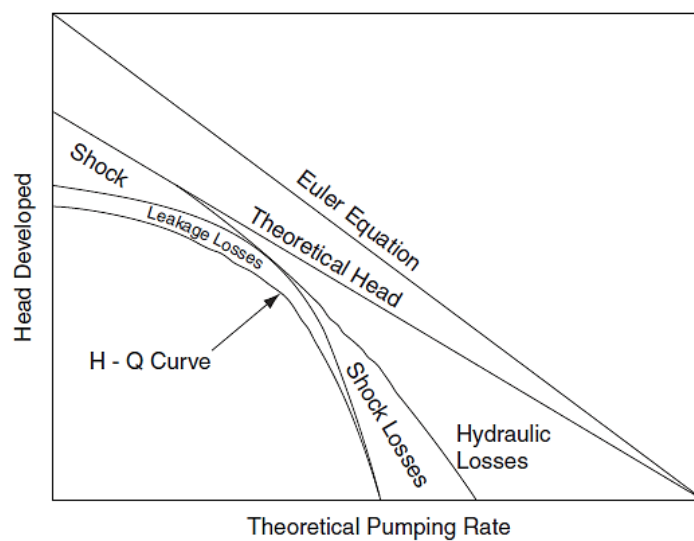


Figure 4: Pump performance curve and the associated losses³

As mentioned earlier, ESPs can be used if the reservoir pressure is too low to lift the fluid naturally. Especially depleted reservoirs with a long production history face those issues. In such cases, water injection might be implemented as a secondary recovery measure. Hence, over the lifetime of a reservoir, the hydrocarbons in place are decreasing while the water cut is steadily increasing. Nowadays, so-called “enhanced oil recovery (EOR) techniques” are tested in a relatively small number of fields. The fundamental principles of these tertiary recovery techniques are either to lower the mobility ratio or to increase the capillary number (Ott 2018). Figure 5 gives a brief overview of the main EOR methods.

³ Takács, G. 2009. *Electrical submersible pumps manual: Design, operations, and maintenance*. Gulf Professional Publ./Elsevier, Amsterdam.

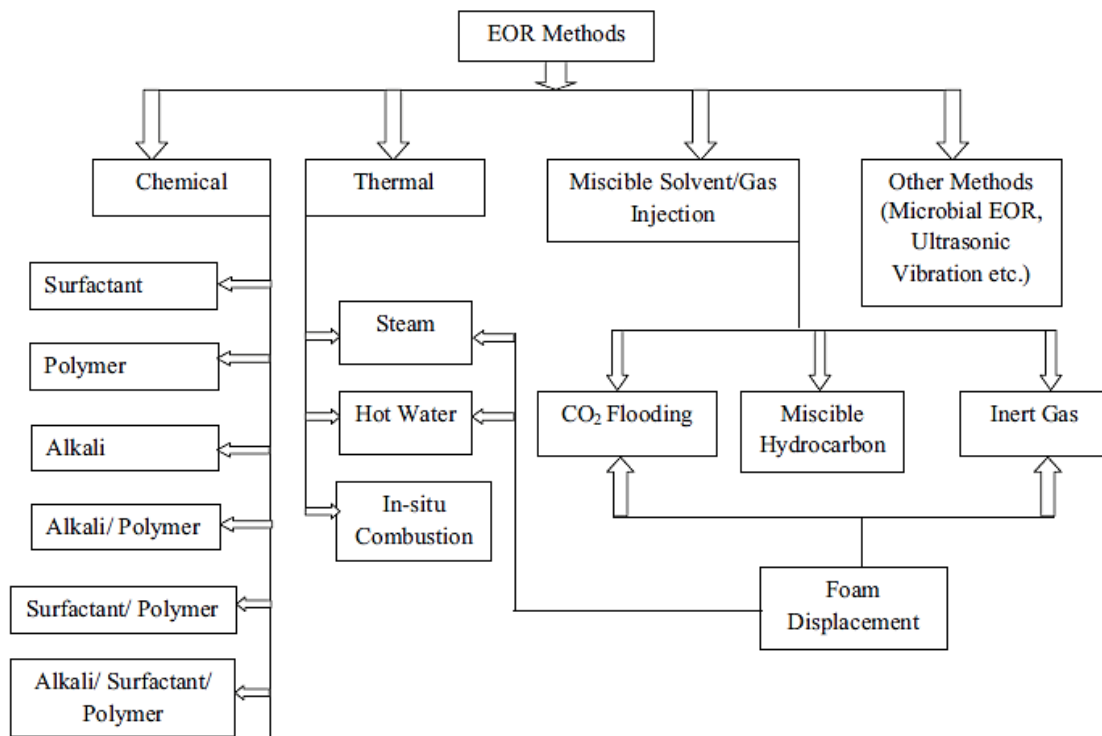


Figure 5: Enhanced oil recovery methods overview⁴

Two of the most common methods are polymer and surfactant injection. Polymer flooding is a common way to increase the viscosity of the displacing fluid by adding polymers to the injection water, which in return, decrease the mobility ratio. On the other hand, surfactants are added to the injected fluid to lower the interfacial tension and hence increase the capillary number. The combination of oil, water, and surfactant results in the formation of micro-emulsions. Similar to a polymer-water mixture, micro-emulsions show non-Newtonian fluid behavior, where the viscosity can be significantly higher than the single fluid viscosity (Petrowiki).

Emulsions can also form within pumps due to turbulent mixing. In contrast to surfactant-stabilized emulsions, this emulsion type is much more unstable. Furthermore, the flow behavior of emulsions may change depending on the droplet concentrations. A low emulsion droplet concentration system might be assumed to have Newtonian flow behavior, whereas a high droplet concentration system behaves like a non-Newtonian fluid (Lim et al. 2015).

2.2 Characteristics of Polymer-laden Fluids and Microemulsions

For the investigation of the viscous effect on pump performance, it is necessary to understand the fundamental characteristics of polymer-laden fluids and emulsions.

⁴ Bera, A., and A. Mandal. 2015. Microemulsions: a novel approach to enhanced oil recovery: a review. *Journal of Petroleum Exploration and Production Technology* 5(3):255–268. [online] URL: <https://doi.org/10.1007/s13202-014-0139-5>.

Therefore, this part of the thesis explains the rheological behaviors of these fluids with a particular focus on viscosity affecting phenomena.

2.2.1 Polymer-laden Fluids

In general, HPAM (partially hydrolyzed polyacrylamide) and Xanthan gum are the two main polymer types used for polymer flooding. The first one is a synthetic polymer, whereas the latter one is a biopolymer. Table 1 summarizes the characteristics of these polymer types, and Figure 6 shows the respective molecular structure.

Table 1: Summary of polymer types⁵

Xanthan	HPAM
Non-ionic	Anionic carboxyl groups (30%)
Insensitive to salinity and hardness	Sensitive to salinity and hardness
More rigid structure	Better water solubility
More expensive than HPAM	Cheaper than Xanthan gum
No retention (no permeability reduction)	Retention (polymer reduction)

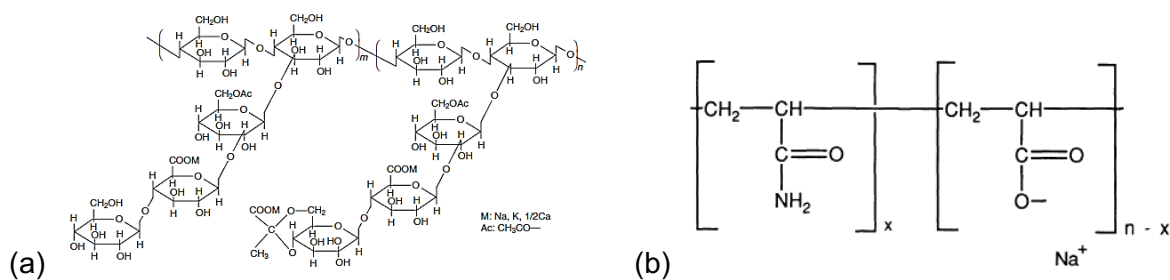


Figure 6: (a) Xanthan gum⁶ (b) Partially hydrolyzed polyacrylamide (HPAM)⁷

For EOR purposes, polymers are normally mixed with water to obtain a higher-viscous polymer solution. Therefore, the most important aspect of a polymer solution's rheology is its viscosity behavior. We can distinguish between the dynamic viscosity and the kinematic viscosity. The dynamic viscosity is a measure of the flow resistance if an external force is applied, for example, in a rotational viscometer. In contrast, the kinematic viscosity is a measure under the weight of gravity without an external force (Alfa Laval 2002). The relationship between the two viscosities is shown in Eq.1⁸:

⁵ Ott, H. 2018. *Enhanced Oil Recovery Lecture Slides: Polymer Methods*, Montanuniversität Leoben.

⁶ Sheng, J. J. 2011. *Modern Chemical Enhanced Oil Recovery: Theory and Practice*. Gulf Professional Publ, Burlington, Mass.

⁷ Sheng, J. J. 2013. *Enhanced Oil Recovery Field Case Studies*. Elsevier/GPP Gulf Professional Publ, Amsterdam.

⁸ https://www.engineeringtoolbox.com/dynamic-absolute-kinematic-viscosity-d_412.html, accessed 05.01.2019

$$\nu = \frac{\mu}{\rho} \quad (\text{Eq. 1})$$

where μ is the dynamic viscosity (SI Unit: N.s/m², CSG Unit: cP), ν is the kinematic viscosity (SI: m²/s, CGS: cSt), and ρ is the fluid density (SI: kg/m³, CSG: S.G.). Some helpful conversions are 0.01 P = 1 cP = 0.001 Pa.s = 1 mPa.s = 0.001 N.s/m² and 0.01 St = 1 cSt = 10⁻⁶ m²/s = 1 mm²/s.

There are five fundamental rheology properties connected to the viscosity: the temperature effect, the salinity effect, the concentration effect, the shear effect, and the pH effect. The following descriptions focus particularly on liquids rather than gases, which can behave differently.

1. The temperature effect can be visualized through a liquid's resistance to flow. Generally, for liquids, the viscosity decreases with increasing temperature and vice versa (Alfa Laval 2002).
2. An increasing polymer concentration leads to a higher bulk fluid viscosity. The Flory-Huggins equation shown in Eq.2⁹ can be used to model the concentration effect at zero shear rate:

$$\mu_p^0 = \mu_w(1 + A_{p1}C_p + A_{p2}C_p^2 + A_{p3}C_p^3) \quad (\text{Eq. 2})$$

where μ_p^0 is the polymer solution viscosity (cP) at zero shear rate, and μ_w is the corresponding water viscosity (cP). A_{px} represents fitting constants, and C_p is the polymer concentration in water, whereby $A_p C_p$ is dimensionless. Figure 7 shows a typical viscosity-concentration relation:

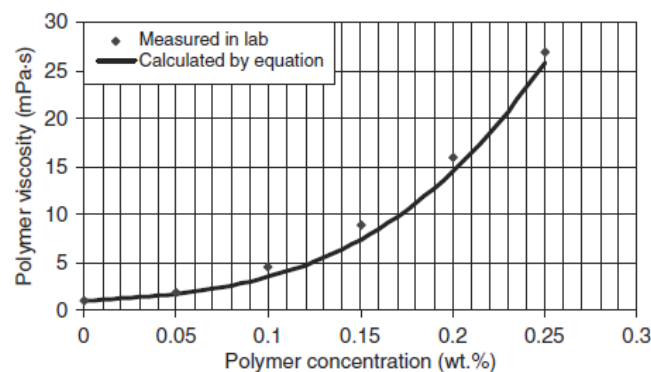


Figure 7: Effect of polymer concentration on polymer viscosity¹⁰

3. The salinity and hardness of a solution affect mainly ionic polymers (HPAM). This effect (at zero shear rate) can be modeled by a slightly modified Flory-Huggins

⁹ Sheng, J. J. 2013. *Enhanced Oil Recovery Field Case Studies*. Elsevier/GPP Gulf Professional Publ, Amsterdam.

¹⁰ Sheng, J. J. 2011. *Modern Chemical Enhanced Oil Recovery: Theory and Practice*. Gulf Professional Publ, Burlington, Mass.

equation shown in Eq.3¹¹. The introduced effective salinity factor (C_{sep}^{Sp}) is a parameter based on the water, anion and divalent concentrations in the aqueous phase.

$$\mu_p^0 = \mu_w(1 + (A_{p1}C_p + A_{p2}C_p^2 + A_{p3}C_p^3)C_{sep}^{Sp}) \quad (\text{Eq. 3})$$

Overall, the HPAM solution viscosity is decreased with increasing brine salinity. Therefore, it is essential to adjust the polymer concentration to the reservoir brine salinity to achieve the anticipated viscosity.

4. The shear effect is probably the most influential rheological property. The best way to illustrate this effect is to plot the shear stress versus the shear rate. On the highest level, there are Newtonian fluids ($n=1$) and non-Newtonian fluids (pseudo-plastic $n<1$, dilatant $n>1$), illustrated in Figure 8.

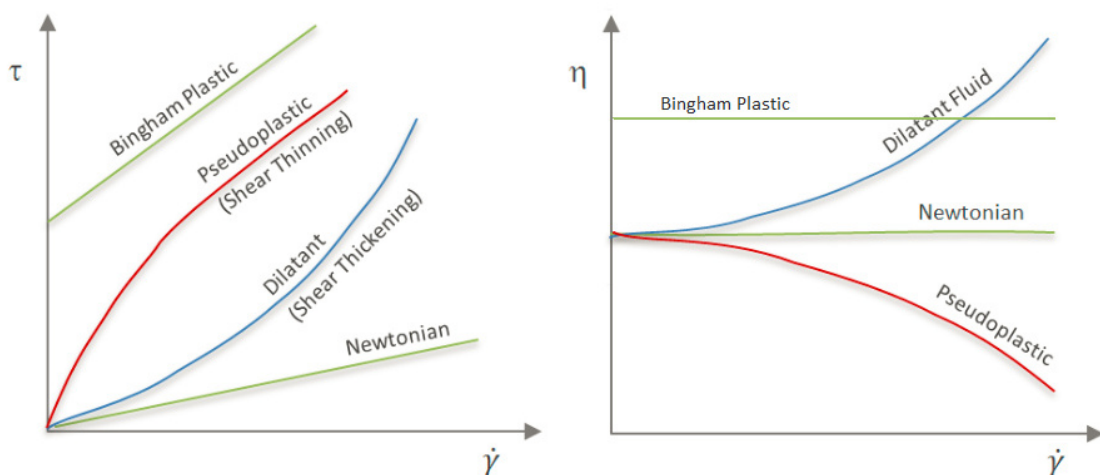


Figure 8: Shear stress versus shear rate - behavior types¹²

The slope of the respective curves in Figure 8 (left) describes the apparent viscosity of the fluid. For Newtonian fluids, this shear stress (τ) and shear rate (du/dy) is directly proportional and result in a constant viscosity. However, for example, for non-Newtonian pseudo-plastic fluids, the shear stress and rate are not directly proportional (Fox et al. 2012). Most polymer solutions belong to the group of pseudo-plastic fluids and hence show shear thinning behavior (Sorbie 1991). The shear thinning behavior can be explained by the disentanglement of the molecular chains during flow; whereas the polymers are randomly orientated in a state of rest (Polymerdatabase 2017). Two models are common to describe such a viscosity

¹¹ Sheng, J. J. 2013. *Enhanced Oil Recovery Field Case Studies*. Elsevier/GPP Gulf Professional Publ, Amsterdam.

¹² Polymerdatabase. 2017. Flow Properties of Polymers. [online] URL: <http://polymerdatabase.com/polymer%20physics/Viscosity2.html>.

reduction. The first one is a simple power-law model shown in Eq.4¹³; the second model was developed by Carreau and is given by Eq.5¹⁴:

$$\mu_p = K\dot{\gamma}^{(n-1)}, \quad \text{with} \quad \tau = K \left(\frac{du}{dy} \right)^{(n-1)} \frac{du}{dy} = \mu_p \frac{du}{dy} \quad (\text{Eq. 4})$$

$$\mu_p - \mu_\infty = (\mu_p^0 - \mu_\infty) [1 + \lambda\dot{\gamma}^\alpha]^{(n-1)/\alpha} \quad (\text{Eq. 5})$$

where μ_p is the apparent polymer solution viscosity, μ_∞ the limiting viscosity (converging viscosity at very high shear rates), K represents the flow consistency index, n the flow behavior index and $\dot{\gamma}$ the applied shear rate. λ is a polymer-related constant and α is usually 2. Figure 9 shows that in a specific shear rate region both models produce the identical curve. Furthermore, it can be seen that at low shear rates, polymer solutions follow Newtonian fluid behavior. However, at higher shear rates, this changes to a viscoelastic one, hence pseudoplastic or dilatant behavior.

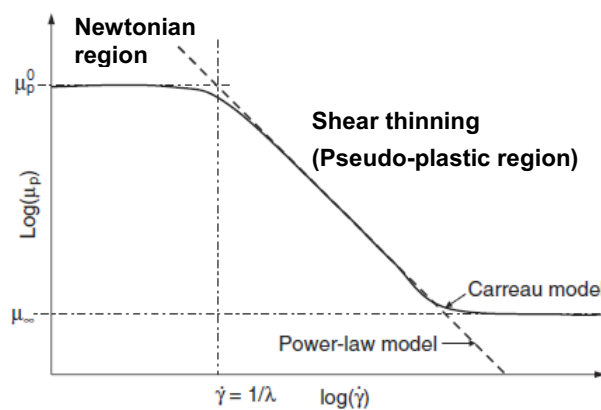


Figure 9: Comparison of power-law and Carrerau model¹⁵

5. The pH effect occurs due to hydrolysis. An increasing pH causes a higher hydrolysis degree, which results in a viscosity increase. However, if pH is increased by adding an alkali salt, the salinity effect is more dominant than the pH effect and would decrease the HPAM solution viscosity (Sheng 2013).

Another factor, which determines the viscosity of a polymer solution, is the molecular weight. It can be said that higher molecular weights are responsible for higher solution viscosity (Sorbie 1991). Figure 10 shows the viscosity of HPAM for different molecular weights and concentrations:

¹³ Fox, R. W., A. T. McDonald, P. J. Pritchard, and J. C. Leylegian. 2012. *Fluid mechanics*. 8th ed., SI version edition. John Wiley, Hoboken, NJ.

¹⁴ Sheng, J. J. 2013. *Enhanced Oil Recovery Field Case Studies*. Elsevier/GPP Gulf Professional Publ, Amsterdam.

¹⁵ Sheng, J. J. 2013. *Enhanced Oil Recovery Field Case Studies*. Elsevier/GPP Gulf Professional Publ, Amsterdam.

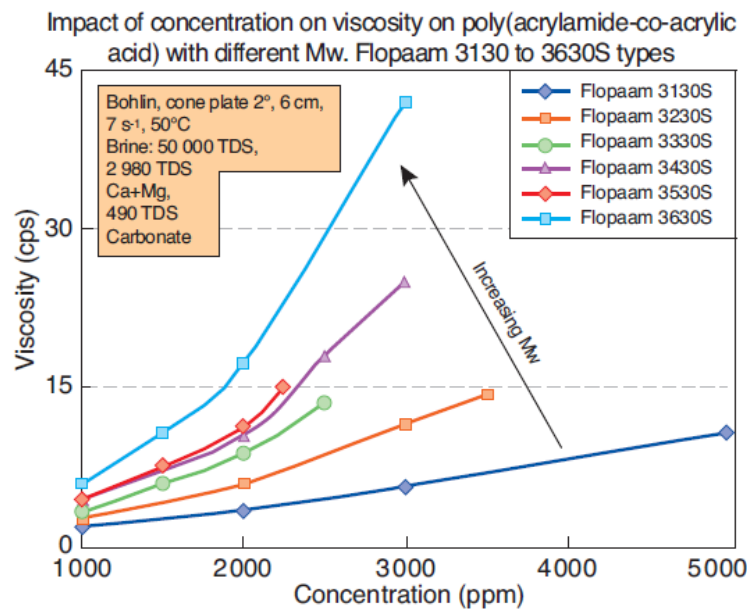


Figure 10: Viscosity of different polymers versus concentration and different molecular weights¹⁶

Another unique concept besides the apparent viscosity is the so-called intrinsic viscosity $[\eta]$. It is the limiting viscosity value of a dilute polymer solution extrapolated to zero concentration. The Mark-Houwink equation shown in Eq.6¹⁷ correlates the intrinsic viscosity of a dilute polymer solution with the molar mass.

$$[\eta] = K' \times M^a; \text{ where } [\eta] = \lim_{c \rightarrow 0} \frac{\eta_{sp}}{c} = \lim_{c \rightarrow 0} \frac{(\eta - \eta_0)}{c} \quad (\text{Eq. 6})$$

where $[\eta]$ is the intrinsic viscosity (dl/g), K' ($3 \cdot 10^{-5} - 700 \cdot 10^{-5}$) and a ($0.5 - 1$) are polymer type dependent constants, and M represents the average molecular weight (g/mol). Furthermore, η is the solution's viscosity, c the polymer concentration in (g/dl) and η_0 the viscosity of the pure solvent.

Lastly, the polymer stability and degradation is a crucial aspect during injection, also in terms of back-production. Different polymer degradation factors should be considered for reliable measurements of the viscosity and molecular weight. In the context of this thesis, polymer stability regarding oxygen, iron, and mechanical shear degradation are of high importance. Therefore, the handling and storage of polymer samples regarding oxygen and iron contamination require great caution. Mechanical degradation can occur on the production side, especially inside centrifugal pumps and chokes (Sheng 2011).

¹⁶ Thomas, A., N. Gaillard, and C. Favero. 2012. Some Key Features to Consider When Studying Acrylamide-Based Polymers for Chemical Enhanced Oil Recovery. *Oil & Gas Science and Technology – Revue d'IFP Energies nouvelles* 67(6):887–902.

¹⁷ Sorbie, K. S. 1991. *Polymer-Improved Oil Recovery*. Springer Netherlands, Dordrecht, s.l.

By definition, mechanical degradation is the molecular breakdown of polymer chains because of applied mechanical stress (shearing off). One simple rule is that the higher the average polymer molecular weight, the higher the shear sensitivity (Thomas 2016). Although the effect is highly unwanted on the injection side of a polymer flood, this attribute may be beneficial or even desired inside producing pumps. In other words, mechanical degradation would help to increase pump efficiency and decrease the required horsepower.

2.2.2 Microemulsions

Generally, microemulsions are optically clear, thermodynamically stable mixtures of two immiscible liquids and a surfactant. The surfactant lowers the interfacial tension between water and oil to ultra-low values (IFT < 0.001 mN/m, compared to a value around 20 mN/m), which causes it to be energetically stable (Klier et al. 2000). In contrast, pure oil-in-water or water-in-oil emulsions are typically thermodynamically unstable, but high molecular weight impurities in the crude can act as natural surfactants and stabilize it (Moura Junior 2016). Table 2 gives an overview of various emulsion types.

Table 2: Emulsion types and classification¹⁸

Type	Size (µm)	Shape	Stability
Micelle	< 0.01	Spherical, cylindrical, dishlike, lamellar	Stable
Microemulsion	0.01 – 0.1	Spherical	Stable
Miniemulsion	0.1 – 0.5	Spherical	Unstable
Macroemulsion	0.5 – 50	Spherical	Unstable

Microemulsions can be divided into three subgroups, which are type II(-), type III, and type II(+) microemulsions. This subdivision is a function of salinity and affects the microemulsion's external fluid phase. Figure 11 illustrates the three types and the respective phase behavior. For enhanced oil recovery purposes, microemulsions feature higher viscosity and induce lower IFT, hence increasing the recovery efficiency (Bera and Mandal 2015).

¹⁸ Sheng, J. J. 2011. *Modern Chemical Enhanced Oil Recovery: Theory and Practice*. Gulf Professional Publ, Burlington, Mass.

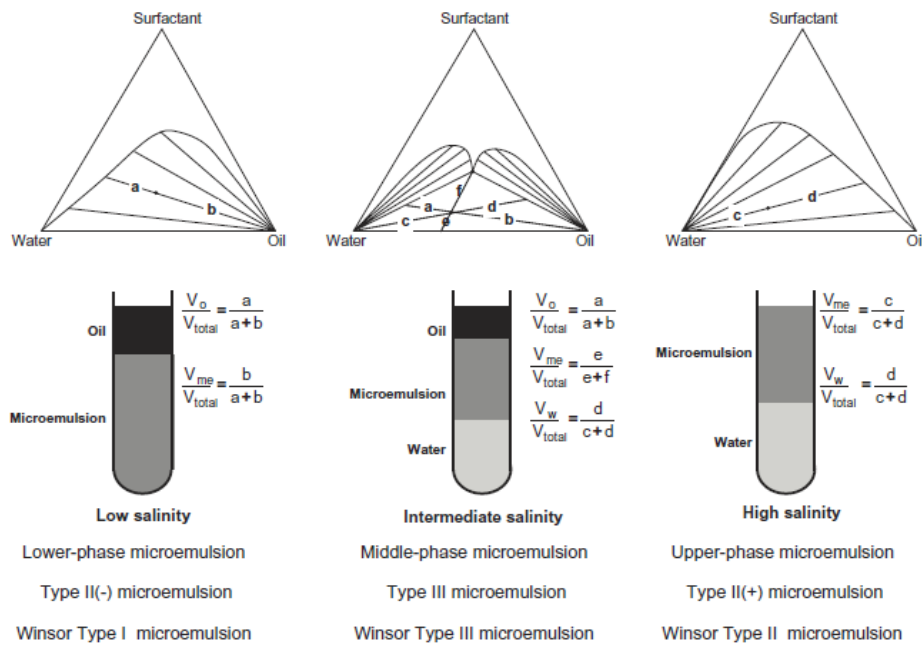


Figure 11: Micro-emulsion types and phase behavior¹⁹

It can be seen that the phase behavior is strongly affected by the brine salinity. In a low salinity brine, a surfactant would show poor solubility in the oil phase. Hence, a water-external microemulsion with little solubilized oil would develop. In case of very high salinity, an oil-external micro-emulsion would develop, because of decreasing electrostatic forces. Only with an optimum saline concentration, a middle-phase microemulsion can be achieved, where the interfacial tension is at its minimum (Lake 1989). The Winsor ration concept explains this phenomenon. It says that the IFT is ultra-low if the attractive energy on both sides of the interface is large and equal in magnitude (Buijse et al. 2012).

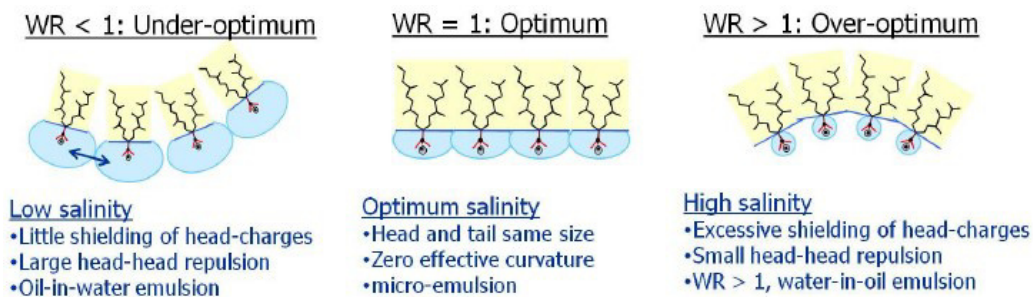


Figure 12: Winsor ratio concept and the interfacial curvature²⁰

As mentioned above, emulsions can also form due to the turbulent flow regime inside a centrifugal pump. Although such emulsion types are not as stable as a microemulsion, they

¹⁹ Sheng, J. J. 2013. *Enhanced Oil Recovery Field Case Studies*. Elsevier/GPP Gulf Professional Publ, Amsterdam.

²⁰ Buijse, M. A., K. Tandon, S. Jain, J.-W. Handgraaf, and J. Fraaije. 2012. Surfactant Optimization for EOR using Advanced Chemical Computational Methods *in SPE Improved Oil Recovery Symposium* (Tulsa, Oklahoma, USA, 2012-04-14). Society of Petroleum Engineers.

still show an increment viscosity. Emulsion stability is strongly affected by continuous phase properties, volume fractions, crude oil composition, droplet size distribution, system temperature, shear rate, and the presence of solids (Bellary et al. 2017). Similarly, the emulsion's viscosity is a function of these factors. For example, the viscosity of an oil-external system increases with increasing water content and starts decreasing after inversion to a water-external system (Bera and Mandal 2015). Figure 13 schematically illustrates this viscosity behavior of emulsions in general. Tagavifar (2018) concluded that emulsion viscosities could be 5 – 10 times greater compared to the underlying oil viscosity (Tagavifar et al. 2018).

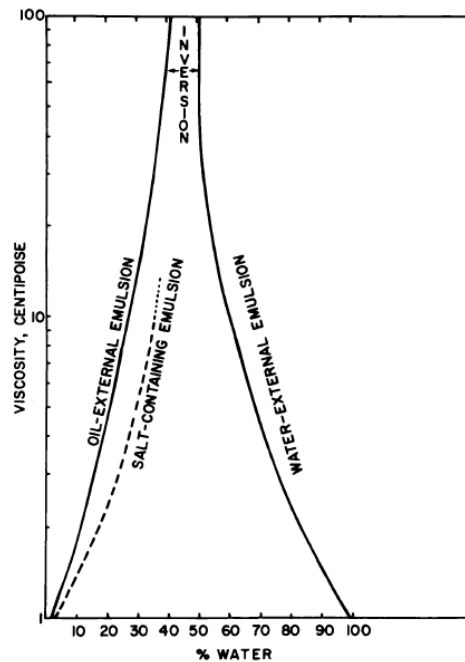
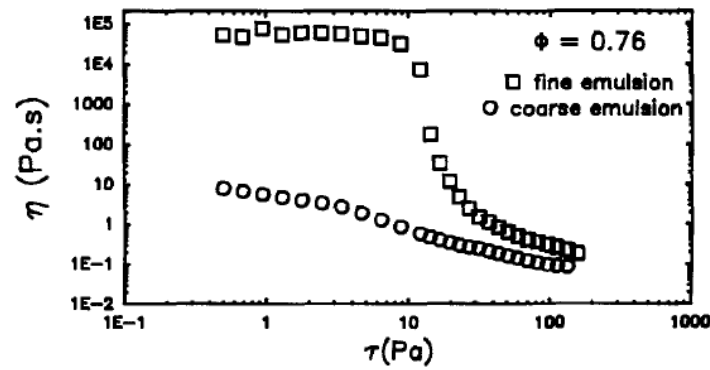


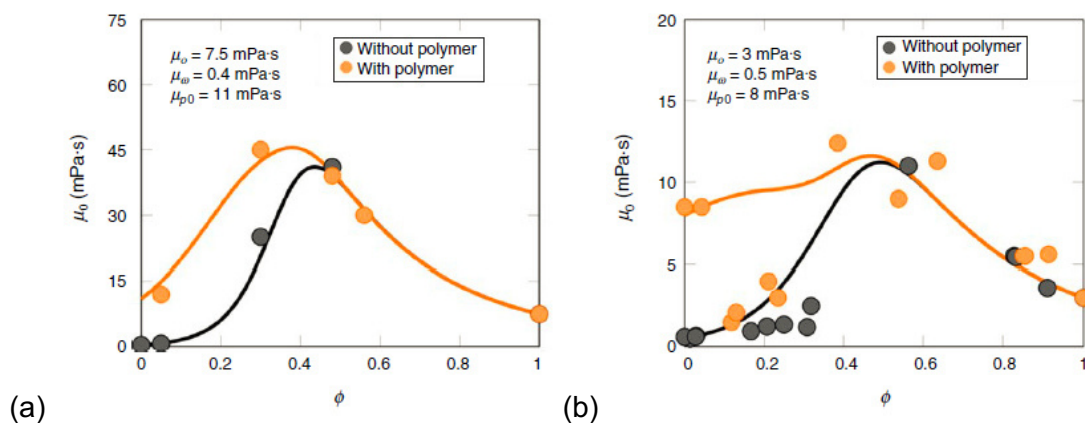
Figure 13: Microemulsion viscosity as a function of oil/water content²¹

The hydrodynamic forces acting on the droplets are one explanation for the higher emulsion viscosity. Hydrodynamic forces due to shear flow cause the emulsion-droplet doublets to rotate. This rotation results in energy dissipation and a consequential higher emulsion viscosity as a function of the droplet concentration (Lim et al. 2015). Pal (1996) performed various experiments with oil-in-water emulsions. Figure 14 shows a 76% water fraction emulsion, where the fine system has an average droplet diameter of 12 μm and the coarse 30 μm . It can be seen that an emulsion with smaller droplets shows a higher developed shear-thinning behavior.

²¹ Prince, L. M. 1977. *Microemulsions: Theory and practice*. Academic Press, New York.

Figure 14: Emulsion viscosity versus shear rate²²

Additionally, polymers might be added to increase the viscosity of the emulsion system (Bera and Mandal 2015). Tagavifar (2018) showed that polymers affect especially water-external emulsions. In contrast, oil-external and middle-phase microemulsion viscosities do not change as can be seen in Figure 15, where ϕ is the oil fraction in these plots (Tagavifar et al. 2018).

Figure 15: (a) 3000 ppm HPAM 70°F, (b) 2000 ppm HPAM 60°C²³

2.3 API RP 112S “Electric Submersible Pump Testing”

The American Petroleum Institute created the API RP 112S “Electric Submersible Pump Testing.”, to assure product consistency among electric submersible pump manufacturers, vendors, and operators. It provides a predefined test procedure, acceptance limits, and other relevant definitions, which are described in the following paragraphs.

The API RP 112S “Electric Submersible Pump Testing” (Version April 2008) suggests the testing of five specific points during a performance test (American Petroleum Institute 1997):

²² Pal, R. 1996. Effect of droplet size on the rheology of emulsions. *AIChE Journal* 42(11):3181–3190.

²³ Tagavifar, M., S. Herath, U. P. Weerasooriya, K. Sepehrnoori, and G. Pope. 2018. Measurement of Microemulsion Viscosity and Its Implications for Chemical Enhanced Oil Recovery. *SPE Journal* 23(01):66–83. [online] URL: <https://doi.org/10.2118/179672-PA>.

1. Test open flow rate (maximum test-achievable flow rate).
2. Maximum recommended flow rate (minRR).
3. Rated flow rate (at best efficiency point, BEP).
4. Minimum recommended flow rate (maxRR).
5. Test shut-off rate (minimum test-achievable flow rate).

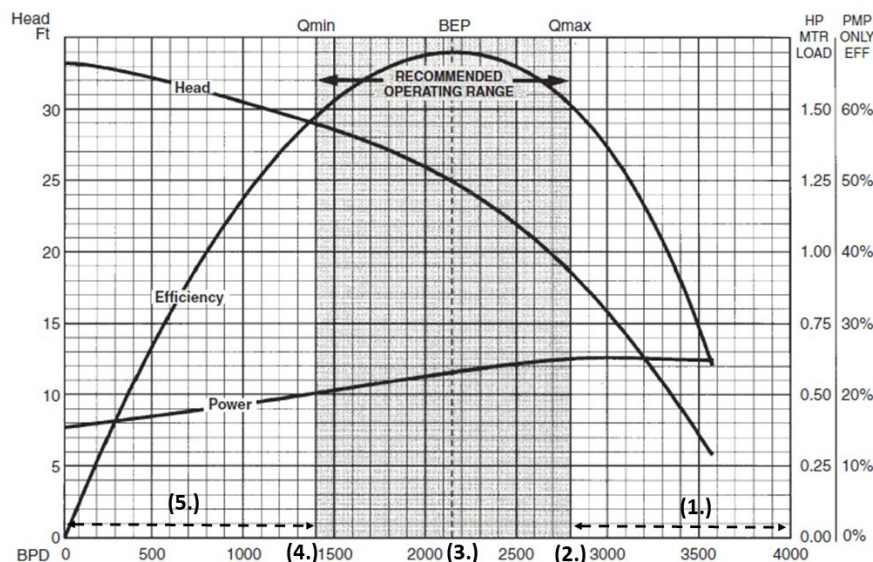


Figure 16: API RP 11S2 - Five performance test points, modified from Takács (2009)²⁴

Based on the rated flow rate, the efficiency is calculated, as shown in Eq.7²⁵:

$$EFF = \frac{H \times Q \times \rho \times g}{BHP} \text{ (Metric units); or } EFF = \frac{H \times Q \times \gamma}{CF \times BHP} \text{ (US units)} \quad (\text{Eq. 7})$$

where EFF is the efficiency (-), H is the produced pump head (m or ft), Q the flow rate (m³/s or gpm), BHP represents the brake horsepower (W or hp), ρ (kg/m³) the density and γ the specific gravity (-) of the pumped fluid. Lastly, g (m/s²) is the gravitational acceleration, and CF is a unit conversion factor (3960 in case of US-Units).

The test data need to be corrected if tests with fluids different from freshwater (specific gravity = 1) at 60°F are performed. Such corrections are essential for fluids with higher viscosity or a different specific gravity. The viscosity correction factors are usually derived empirically (American Petroleum Institute 1997). The most straightforward approach would be to use correction factor tables, published by the pump manufacturers. Chapters 0 and 2.6 provide a detailed literature overview of the available correction approaches. The basic

²⁴ Takács, G. 2009. *Electrical submersible pumps manual: Design, operations, and maintenance*. Gulf Professional Publ./Elsevier, Amsterdam.

²⁵ Stepanoff, A. J. 1957. *Centrifugal and axial flow pumps: Theory, design, and application*. Krieger, Malabar (Florida).

equations to convert test data of a fluid with a specific viscosity into a basic water test are shown in Eq.8 – Eq.10²⁶:

$$H_w = H_{total,test} \times H_{vis} \quad (\text{Eq. 8})$$

$$Q_w = Q_{test} \times Q_{vis} \quad (\text{Eq. 9})$$

$$BHP_w = \left(\frac{BHP_w}{\gamma} \right) \times BHP_{vis} \quad (\text{Eq. 10})$$

where H_w , Q_w , BHP_w are the head (m or ft), flow rate (m^3/s or bbl/day) and brake horsepower (W or hp) of a standard water test case. $H_{total\ test}$, Q_{test} , BHP_{test} are the head (m or ft), flow rate (m^3/s or bbl/day) and brake horsepower (hp) for the viscous fluid test case with the respective specific gravity γ . H_{vis} , Q_{vis} , BHP_{vis} are the empirically derived correction factors.

Moreover, the tests should be run at 3500 rpm for 60 Hz or 2917 rpm for 50 Hz (Takács 2009). In case of variations from those speeds, the application of the so-called affinity laws is recommended for correcting speed. The affinity laws are shown in Eq.11 – Eq.13²⁷:

$$Q_2 = Q_1 \times \left(\frac{N_2}{N_1} \right)^1 \quad (\text{Eq. 11})$$

$$H_2 = H_1 \times \left(\frac{N_2}{N_1} \right)^2 \quad (\text{Eq. 12})$$

$$BHP_2 = BHP_1 \times \left(\frac{N_2}{N_1} \right)^3 \quad (\text{Eq. 13})$$

where N is the pumping speed (rpm), Q are the flow rates (m^3/s or bbl/day), H are the developed heads (m or ft), and BHP represent the brake horsepower (W or hp) for the respective speed.

According to API RP 112S, the pump performance curves published by a manufacturer need to be within a specific tolerance band, shown in Figure 16, while Table 3 shows the limits for each parameter (American Petroleum Institute 1997).

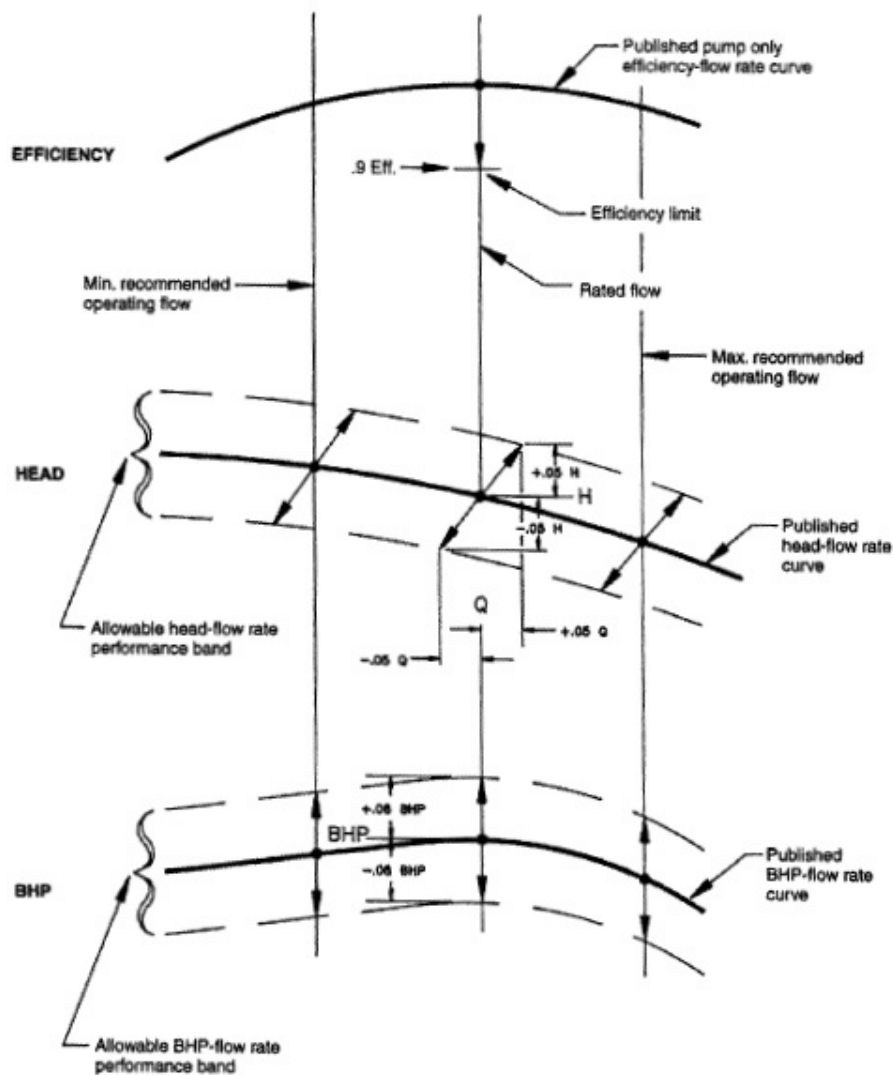
²⁶ American Petroleum Institute. 1997. API RP 11S2 - Recommended Practice for Electric Submersible Pump Testing. American Petroleum Institute, Dallas, Texas.

²⁷ Takács, G. 2009. *Electrical submersible pumps manual: Design, operations, and maintenance*. Gulf Professional Publ./Elsevier, Amsterdam.

Table 3: Acceptance limits for the manufacturer's published performance curves²⁸

Curve	Limits (Tolerance Band)	Where Applicable
Head (vs. flow rate)	$\pm 5.0\%$	Recommended operating range
Flow rate	$\pm 5.0\%$	Recommended operating range
BHP (vs. flow rate)	$\pm 8.0\%$	Recommended operating range
Efficiency vs. flow rate	90.0% of efficiency	At rated flow (generally BEP)

Figure 17 shows how the API tolerance bands are derived from the manufacturers' published performance curves.

Figure 17: API – pump test acceptance limits²⁹

²⁸ American Petroleum Institute. 1997. API RP 11S2 - Recommended Practice for Electric Submersible Pump Testing. American Petroleum Institute, Dallas, Texas.

²⁹ American Petroleum Institute. 1997. API RP 11S2 - Recommended Practice for Electric Submersible Pump Testing. American Petroleum Institute, Dallas, Texas.

2.4 ESP Start Characteristics

The ESP start-up requires substantial power to set the fluid in the tubing string into motion. However, the electric motor accelerates to its predefined speed within seconds. Due to the instantaneous power requirement, the electric motor draws significantly higher currents, 4-5 times higher than usual. Additionally, the high current at the engine causes a voltage drop in the electrical cable. To ensure a proper ESP startup, the voltage at the motor terminals should be at least 50% of the nameplate voltage. Another factor to consider during startup is the much higher or maximum occurring torque. As a result, a variable speed drive is a piece of essential equipment, which allows a “soft startup” of the ESP (Takács 2009). The VSD can be used to slowly ramp up the frequency of the ESP, while reducing peak currents and high starting torques (Centrilift 1997).

2.5 Performance Prediction for Newtonian Fluids

This chapter gives an overview of standard models and ongoing research for viscosity correction of pump performance curves. Their fundamental approach is either experimental or theoretical. The dimensions analysis is the basis of many of these models. Therefore, it is necessary to give a brief overview of the most critical dimensionless parameters. One primary metric is the specific speed given by Eq.14³⁰ and shown by the impeller design in Figure 18.

$$n_s = \frac{n \times \sqrt{Q}}{H^{3/4}} = 51.6 \times n_q ; n_q = \frac{n_{met} \times \sqrt{Q_{met}}}{H_{met}^{3/4}} ; \omega_s = \frac{\omega \times \sqrt{Q_{met}}}{(g \times H_{met})^{3/4}} = \frac{n_q}{52.9} \quad (\text{Eq. 14})$$

Here, n_s is the specific speed in US-units, with n being the pump speed at the BEP (rpm), Q represents the pumping rate at the BEP (gpm), and H is the head per stage at the BEP (ft). Next, n_q is the specific speed in metric units, with n_{met} being the pump speed at the BEP (rpm), Q_{met} represents the pumping rate at the BEP (m^3/s), and H_{met} is the head per stage at the BEP (m). Moreover, ω is the dimensionless specific speed, with ω being the pump speed at the BEP (1/s), Q_{met} represents the pumping rate at the BEP (m^3/s), and H_{met} is the head per stage at the BEP (m). Sometimes ω is also required in (rad/s) with 1 (1/s) being 2π (rad/s).

³⁰ Gülich, J. F. 2014. *Centrifugal Pumps*. 3rd ed. 2014 edition. Springer Berlin Heidelberg, Berlin, Heidelberg, s.l.

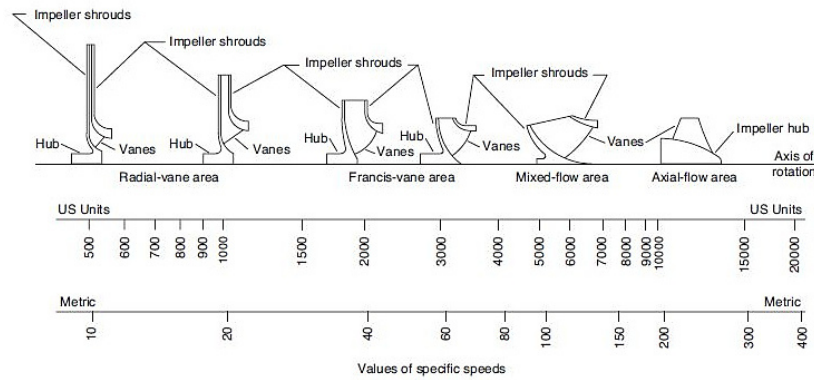


Figure 18: Impeller type vs. specific speed (n_s and n_q)³¹

Other parameters are the flow, head, and power coefficients as well as the rotational Reynolds number and the hydraulic efficiency, given by Eq.15 – Eq.19^{32,33}. It should be mentioned that the affinity laws are derived from those dimensionless groups (Stepanoff 1957).

$$\text{Flow coefficient} = \phi = \frac{Q}{\omega \times D^3} \quad (\text{Eq. 15})$$

$$\text{Head coefficient} = \psi = \frac{g \times H}{\omega^2 \times D^2} = \frac{\Delta p}{\rho \times \omega^2 \times D^2} \quad (\text{Eq. 16})$$

$$\text{Power coefficient} = \Pi = \frac{T \times \omega}{\rho \times \omega^3 \times D^5} \quad (\text{Eq. 17})$$

$$\text{Rotational Reynolds number} = \frac{\rho \times \omega \times D^2}{\mu} = \frac{\omega \times D^2}{\nu} \quad (\text{Eq. 18})$$

$$\text{Hydraulic efficiency} = \frac{\psi \times \phi}{\Pi} = \frac{\rho \times g \times Q \times H}{T \times \omega} \quad (\text{Eq. 19})$$

The units of these equations should be in fundamental units to obtain the dimensionless value, whereby g is the gravity acceleration (length/time²), and D represents the pump impeller diameter (length).

2.5.1 Hydraulic Institute Model

The Hydraulic Institute Model is one of the most commonly used empirical procedures for viscosity correction of pump performance curves using Newtonian fluids. The procedure is based on experimental data, from which several correction charts (e.g., Figure 19) have

³¹ pumps.org. Classification by Specific Speed. [online] URL: <http://pumps.org/Source/Wireframes/PumpBasicsDiagramPage.aspx?pageid=2535>.

³² Stepanoff, A. J. 1957. *Centrifugal and axial flow pumps: Theory, design, and application*. Krieger, Malabar (Florida).

³³ White, F. M. 2011. *Fluid mechanics*. 7. ed. in SI units edition. McGraw-Hill, Singapore.

been developed (Takács 2009). With these factors, the water performance curve can be adjusted for viscosity by using Eq.20 – Eq.22³⁴:

$$Q_{visc} = C_Q \times Q_w \tag{Eq. 20}$$

$$H_{visc} = C_H \times H_w \tag{Eq. 21}$$

$$EFF_{visc} = C_{EFF} \times EFF_w \tag{Eq. 22}$$

where Q_{visc} , H_{visc} , EFF_{visc} are the flow rate (bbl/day), head (ft) and efficiency for the viscous fluid case. Q_w , H_w , EFF_w is the flow rate (bbl/day), head (ft) and efficiency for the water case. C_Q , C_H , C_{EFF} are the flow rate, head and efficiency correction factors.

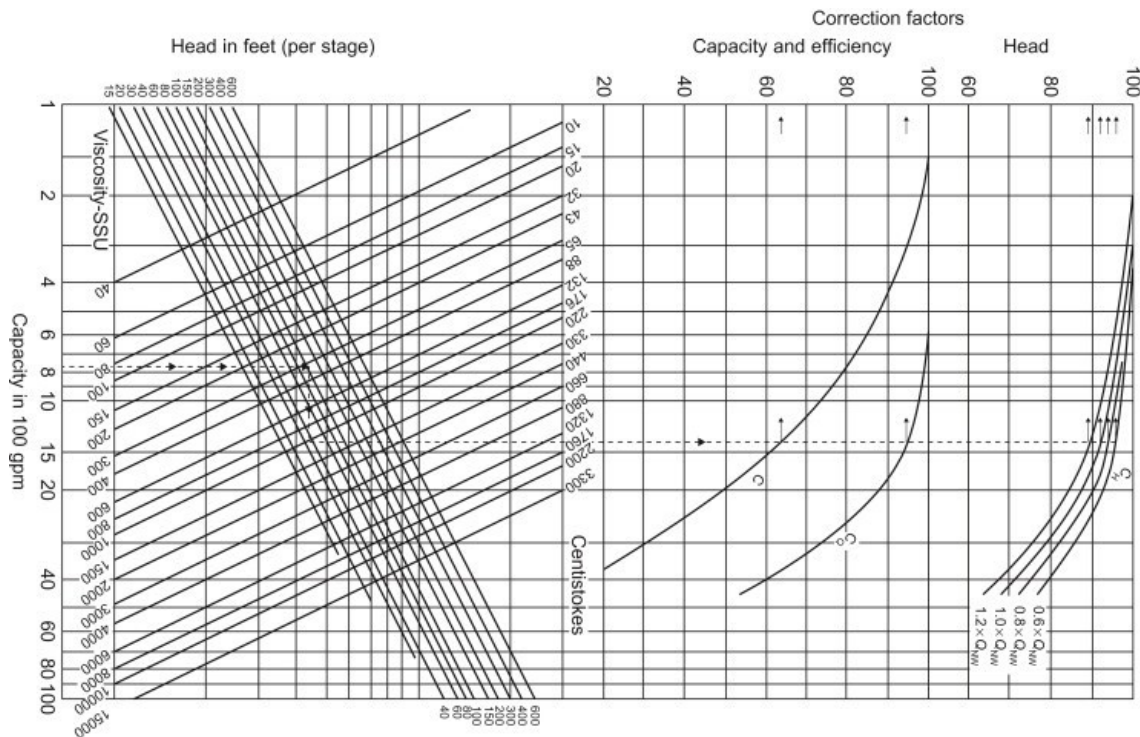


Figure 19: Typical Hydraulic Institute viscosity correction chart for 2 – 8-inch pumps³⁵

In 2000, Turzo et al. developed a numerical model, which curve-fitted the Hydraulic Institute diagrams (Takács 2009). The result was a corrected liquid rate, which is calculated as shown in Eq.23– Eq.24³⁶:

$$Q^* = e^{\left(\frac{39.5276+26.5605 \times \ln(v)-y}{51.6565}\right)} \tag{Eq. 23}$$

³⁴ Takács, G. 2009. *Electrical submersible pumps manual: Design, operations, and maintenance*. Gulf Professional Publ./Elsevier, Amsterdam.

³⁵ Menon, E. S., editor. 2011. *Pipeline Planning and Construction Field Manual*. Elsevier/GPP Gulf Professional Publ, Amsterdam.

³⁶ Turzo, Z., G. Takacs, and J. Zsuga. 2000. Equations correct centrifugal pump curves for viscosity. *Oil and Gas Journal* 98.

with:

$$y = -7.5946 + 6.6504 \times \ln(H_{wBEP}) + 12.8429 \times \ln(Q_{wBEP}) \quad (\text{Eq. 24})$$

where Q^* is the corrected liquid rate (100 gpm), Q_{wBEP} represents the water rate at the BEP (100 gpm), H_{wBEP} is the pump head (ft) at the BEP, and ν represents the liquid kinematic viscosity (cSt).

By using the corrected liquid rate, the C-values can be determined, as shown in Eq.25 – Eq.30³⁷ and additionally illustrated in Figure 20. The head correction uses four specific points, which are 60%, 80%, 100%, and 120% of the best efficiency water capacity (Turzo et al. 2000).

$$C_Q = 1.0 - 4.0327 \times 10^{-3} \times Q^* - 1.7240 \times 10^{-4} \times Q^{*2} \quad (\text{Eq. 25})$$

$$C_{EFF} = 1.0 - 3.3075 \times 10^{-2} \times Q^* + 2.8875 \times 10^{-4} \times Q^{*2} \quad (\text{Eq. 26})$$

$$C_{H0.6} = 1.0 - 3.6800 \times 10^{-3} \times Q^* - 4.3600 \times 10^{-5} \times Q^{*2} \quad (\text{Eq. 27})$$

$$C_{H0.8} = 1.0 - 4.4723 \times 10^{-3} \times Q^* - 4.1800 \times 10^{-5} \times Q^{*2} \quad (\text{Eq. 28})$$

$$C_{H1.0} = 1.0 - 7.00763 \times 10^{-3} \times Q^* - 1.4100 \times 10^{-5} \times Q^{*2} \quad (\text{Eq. 29})$$

$$C_{H01.2} = 1.0 - 9.0100 \times 10^{-3} \times Q^* + 1.3100 \times 10^{-5} \times Q^{*2} \quad (\text{Eq. 30})$$

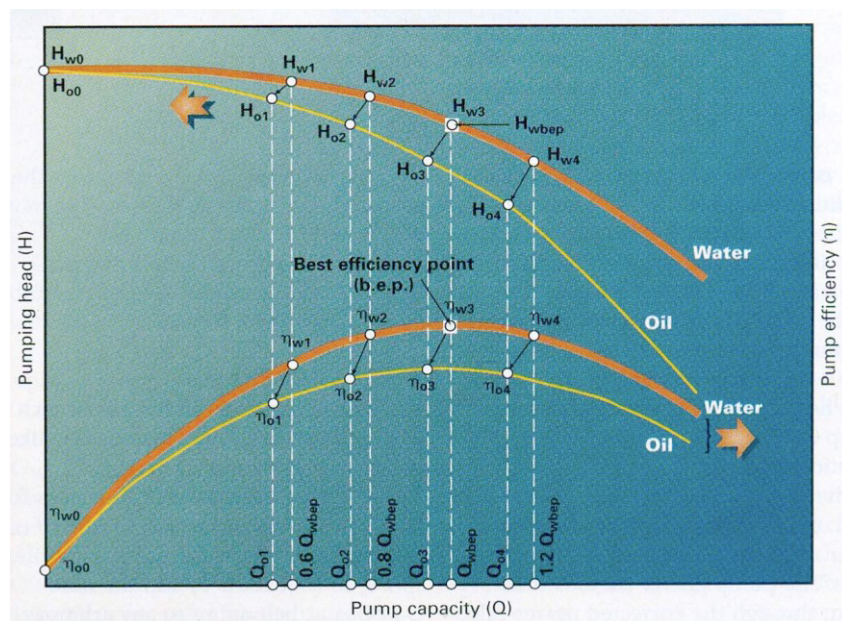


Figure 20: Illustration of the Hydraulic Institute correction method³⁸

³⁷ Turzo, Z., G. Takacs, and J. Zsuga. 2000. Equations correct centrifugal pump curves for viscosity. *Oil and Gas Journal* 98.

³⁸ Turzo, Z., G. Takacs, and J. Zsuga. 2000. Equations correct centrifugal pump curves for viscosity. *Oil and Gas Journal* 98.

Furthermore, the head and efficiency at shut-in conditions are known because those values are independent of the viscosity and are the same as in the water case (Turzo et al. 2000). The last step is then to calculate and plot each viscosity corrected performance curve and compare them with the freshwater curves. For the calculation of the brake horsepower at each rate, the following Eq.31³⁹ can be used:

$$BHP = 7.368 \times 10^{-6} \frac{Q \times H \times \gamma_l}{\eta} \quad (\text{Eq. 31})$$

where BHP is the brake horsepower (hp), Q represents the pump capacity (bpd), H is the pump head (ft), γ_l represents the liquid specific gravity (-), and η is the pump efficiency (%).

2.5.2 Stepanoff Model

Stepanoff (1957) created a procedure for pump head and efficiency correction at the best efficiency point. His empirical method resulted in a diagram for the BEP (Figure 21) which is based on a Reynolds number-like parameter, given by Eq.32⁴⁰. The calculation procedure is straightforward. The first step is the correction of H_{wBEP} to obtain H_{oBEP} . Secondly, calculate the Q_{oBEP} from Eq.33⁴¹:

$$Re_{Stepanoff} = 248,387 \frac{Q_{wBEP}}{D \times \nu} \quad (\text{Eq. 32})$$

$$\frac{Q_{wBEP}}{Q_{oBEP}} = \left(\frac{H_{wBEP}}{H_{oBEP}} \right)^{1.5} \quad \text{or} \quad F_Q = F_H^{1.5} \quad (\text{Eq. 33})$$

where Q_{wBEP} is the water capacity at BEP (100 gpm), H_{wBEP} is the water head at the BEP (ft), Q_o represents the corrected capacity (100 gpm), H_o is the adjusted pumping head (ft), D the given pump impeller OD (in), and ν is the kinematic liquid viscosity (cSt).

³⁹ Takács, G. 2009. *Electrical submersible pumps manual: Design, operations, and maintenance*. Gulf Professional Publ./Elsevier, Amsterdam.

⁴⁰ Turzo, Z., G. Takacs, and J. Zsuga. 2000. Equations correct centrifugal pump curves for viscosity. *Oil and Gas Journal* 98.

⁴¹ Turzo, Z., G. Takacs, and J. Zsuga. 2000. Equations correct centrifugal pump curves for viscosity. *Oil and Gas Journal* 98.

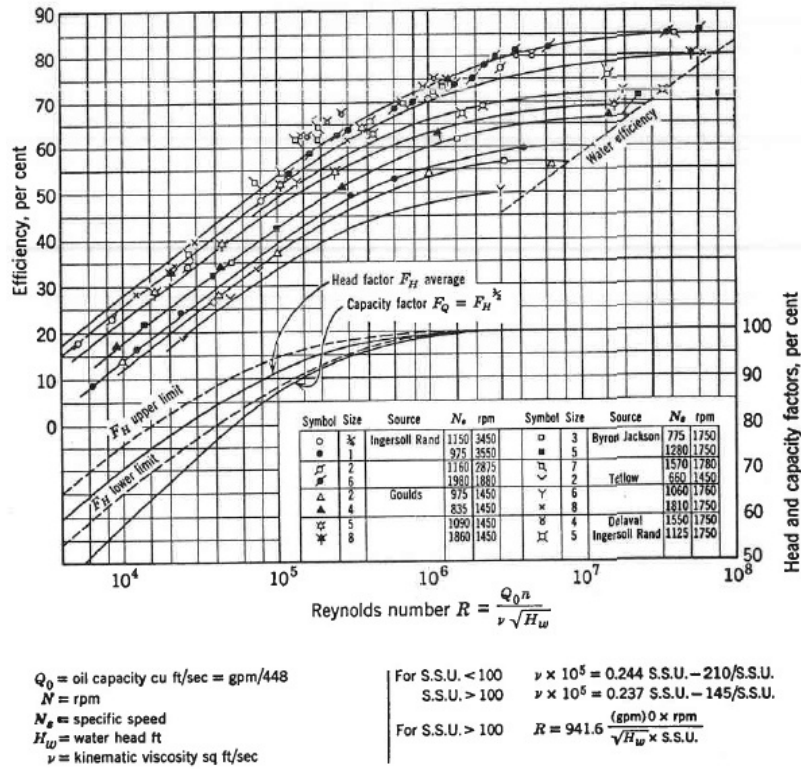


Figure 21: Correction factors for head and efficiency⁴²

As a result, two curve points are known. One is the corrected head performance at the BEP and the second the shut-in point, which is independent of the fluid viscosity. The next step is to calculate the corrected break horsepower (Eq. 25) by using the adjusted values at the BEP. Lastly, the efficiency curve (Eq. 7) is determined by values of the new head and break horsepower curves (Stepanoff 1957). One disadvantage is that the approximated curves between the best efficiency and the shut-off point are prone to human error. Therefore, Stepanoff’s model should be used only around the BEP (Turzo et al. 2000). However, recent research has shown that the Stepanoff model also holds in regions different from the best efficiency point (Paternost et al. 2015) (Trevisan and Prado 2011). Additionally, the author states that the specific speed remains constant at the best efficiency point for different viscosities. Also, the affinity laws hold with little inaccuracies for fluids with viscosities other than water (Stepanoff 1957).

2.5.3 Paciga Model

Paciga produced a Reynolds number-like model similar to the Stepanoff model, calculated by Eq.34⁴³. He developed correction charts for each performance metric by using the specific speed and Q_w/Q_{WBEP} as correlation parameters (Turzo et al. 2000).

⁴² Stepanoff, A. J. 1957. *Centrifugal and axial flow pumps: Theory, design, and application*. Krieger, Malabar (Florida).

⁴³ Turzo, Z., G. Takacs, and J. Zsuga. 2000. Equations correct centrifugal pump curves for viscosity. *Oil and Gas Journal* 98.

$$Re_{Paciga} = 10.753 \frac{n \times D^2}{\nu} \quad (\text{Eq. 34})$$

$$n_s = 0.7067 \times n \times Q_{wBEP}^{1/2} \times H_{wBEP}^{-3/4} \quad (\text{Eq. 35})$$

where n is the pump speed (1/min), n_s the respective specific speed (-), D represents the pump impeller OD (in), ν the kinematic liquid viscosity (cSt), Q_{wBEP} the water capacity at BEP (100 gpm), and H_{wBEP} is the water head at BEP (ft).

Different from the Stepanoff model, the Paciga model allows the determination of complete performance curves. However, the model poses some problems with highly viscous fluids. It might be unreliable in highly viscous applications related to the petroleum industry (Turzo et al. 2000).

2.5.4 Solano's Performance Map

Solano (2009) conducted an ESP performance analysis with single-phase viscous fluids (Trevisan and Prado 2011). The author concluded that the head coefficient should be a unique function of the flow coefficient and the Reynolds number (Stel et al. 2014). Four normalized dimensionless parameters shown in Eq.38 – Eq.39^{44,45} are used to describe the pump performance. The normalization can be done either with the maximum value or with the design value, which is at the best efficiency point.

$$\psi_n = \frac{H}{H_{des}} \times \left(\frac{n_{des}^2}{n^2} \right) \quad (\text{Eq. 36})$$

$$\phi_n = \frac{q}{q_{des}} \times \left(\frac{n_{des}}{n} \right) \quad (\text{Eq. 37})$$

$$Re_n = \frac{\omega}{\omega_{des}} \times \frac{\nu_{des}}{\nu} \quad (\text{Eq. 38})$$

$$n_n = \frac{n_s}{n_{s,des}} \quad (\text{Eq. 39})$$

where ϕ_n is the normalized flow coefficient ψ_n is the normalized head coefficient, Re_n represents the normalized rotational Reynolds number and n_n the normalized rotational speed.

⁴⁴ Paternost, G. M., A. C. Bannwart, and V. Estevam. 2015. Experimental Study of a Centrifugal Pump Handling Viscous Fluid and Two-Phase Flow. *SPE Production & Operations* 30(02):146–155. [online] URL: <https://doi.org/10.2118/165028-PA>.

⁴⁵ Ofuchi, E. M., H. Stel, T. Sirino, R. Dunaiski, and R. E. M. Morales. 2015. Numerical Analysis of Performance Degradation in Multistage Electric Submersible Pumps in H. S. d. C. Mattos, editor. *23rd ABCM International Congress of Mechanical Engineering* (Rio de Janeiro, Brazil, 06.12.2015 - 11.12.2015). ABCM Brazilian Society of Mechanical Sciences and Engineering Rio de Janeiro, Brazil.

The author observed a performance degradation with constant specific speed and proposed two correction factors based on the normalized coefficients, calculated with Eq.40 – Eq.41⁴⁶:

$$C_H = \frac{\psi_n}{\psi_{n,w}} = \frac{H}{H_w} \times \left(\frac{n_w^2}{n^2} \right) \text{ at a constant } n_n \quad (\text{Eq. 40})$$

$$C_Q = \frac{\phi_n}{\phi_{n,w}} = \frac{q}{q_w} \times \left(\frac{n_w}{n} \right) \text{ at a constant } n_n \quad (\text{Eq. 41})$$

where C_H and C_Q are the head and rate correction factors, the subscript w represents values for the water case at the given catalog speed.

Ofuchi (2015) found that there is a relation $C_Q=C_H^{1.5}$, which is similar to the relation proposed by Stepanoff (1957). It should be mentioned that Solano's approach is purely based on test data and does not allow the determination of correction factors without experiments (Paternost et al. 2015). Solano also validated the Stepanoff proposal, that the specific speed remains constant in case of viscous performance degradation (Ofuchi et al. 2015).

In 2015, Paternost et al. developed a theoretical model based on Salanos's experimental data. With his polynomial correlation approach, the performance of a specific pump under a broad range of conditions can be predicted. However, a few experiments are still necessary to determine the correlation constants for the pump under testing. The basis of the author's model is the theoretical Euler head curve (Figure 4) reduced by the losses. For the pump power correlation, he considered the hydraulic power and its losses, as well as the friction losses occurring within the pump (Paternost et al. 2015). The result were two polynomial correlations, shown in Eq.42 - Eq.43⁴⁷:

$$\psi = a_o - (a_1 + a_2X)\phi - \left[a_3 + a_4 \left(\frac{X}{\phi} \right)^n \right] \phi^2 \quad (\text{Eq. 42})$$

$$\Pi = b_o + b_1X + (b_2 + b_3X)\phi + b_4\phi^2 \quad (\text{Eq. 43})$$

where ψ and π are the pump head and power coefficient, ϕ represents the capacity coefficient, and X is the inverse rotational Reynold number. The correlation constants a_i and n are obtained by fitting Eq. 42 and Eq. 43 to experimental data. These parameters are constant and only valid for a given pump type (Paternost et al. 2015).

⁴⁶ Ofuchi, E. M., H. Stel, T. Sirino, R. Dunaiski, and R. E. M. Morales. 2015. Numerical Analysis of Performance Degradation in Multistage Electric Submersible Pumps in H. S. d. C. Mattos, editor. *23rd ABCM International Congress of Mechanical Engineering* (Rio de Janeiro, Brazil, 06.12.2015 - 11.12.2015). ABCM Brazilian Society of Mechanical Sciences and Engineering Rio de Janeiro, Brazil.

⁴⁷ Paternost, G. M., A. C. Bannwart, and V. Estevam. 2015. Experimental Study of a Centrifugal Pump Handling Viscous Fluid and Two-Phase Flow. *SPE Production & Operations* 30(02):146–155. [online] URL: <https://doi.org/10.2118/165028-PA>.

2.5.5 Morrison's Modified Affinity Law

Morrison (2017) developed the “modified affinity law,” which produces a single universal pump specific curve for varying operation and viscosity conditions (Morrison et al. 2017). In his approach, the author makes use of the dimensionless analysis variables, such as the head coefficient, the flow coefficient, the rotational Reynolds number, and the specific speed. Morrison proposes the independent variable ϕ^*Re^{-a} , where a is the so-called Morrison number (Patil et al. 2018). Plotting this independent variable for different viscosity cases against the flow coefficient, ends up with overlapping curves, which approach a single universal curve. This curve is used as a “modified affinity law” to predict the pump head under viscous conditions. (Morrison et al. 2018). The benefit of this model is that only the water performance curve is required for the performance prediction, similar to the HI Method.

The procedure is as follows: The first step is to calculate the dimensionless coefficients for the water case using the catalog data. Secondly, the Morrison number can be calculated for the water and viscous cases as a function of specific speed and the rotational Reynolds number by using Eq.44 – Eq.46⁴⁸. It should be mentioned that these equations are empirically derived correlations based on available data, and might be refined or updated in the future (Patil and Morrison 2019).

1. Laminar regime (Re up to ≈ 17.000 , $1000 < n_s < 3200$)

$$Mo = a = 8147.6 \times n_s^{-1.59} \times \ln(Re) - 2 \times 10^6 \times n_s^{-2.059} \quad (\text{Eq. 44})$$

2. Transition zone (Re from ≈ 17.000 - 65.000)

$$Mo = a = (1 \times 10^{-6} \times n_s - 0.0008) \times Re^{(-8 \times 10^{-5} \times n_s + 0.5474)} \quad (\text{Eq. 45})$$

$$Mo_{max} = Mo \pm c, \quad c \dots \text{peak value adjustment}$$

3. Turbulent regime (Re larger ≈ 65.000)

$$Mo = a = \left(-\frac{n_s}{20000} + 0.2698 \right) \times Re^{\left(\frac{n_s}{50000} - 0.11 \right)} \quad (\text{Eq. 46})$$

From Figure 22 we can see that calculating the dimensionless parameters for the water case and the viscous cases based on experimental data the plot ψ versus ϕ can be produced. Applying now the equation ϕ^*Re^{-a} and plotting this value against ψ , we obtain the proposed universal curve.

⁴⁸ Patil, A., and G. Morrison. 2019. Affinity Law Modified to Predict the Pump Head Performance for Different Viscosities Using the Morrison Number. *Journal of Fluids Engineering* 141(2):21203.

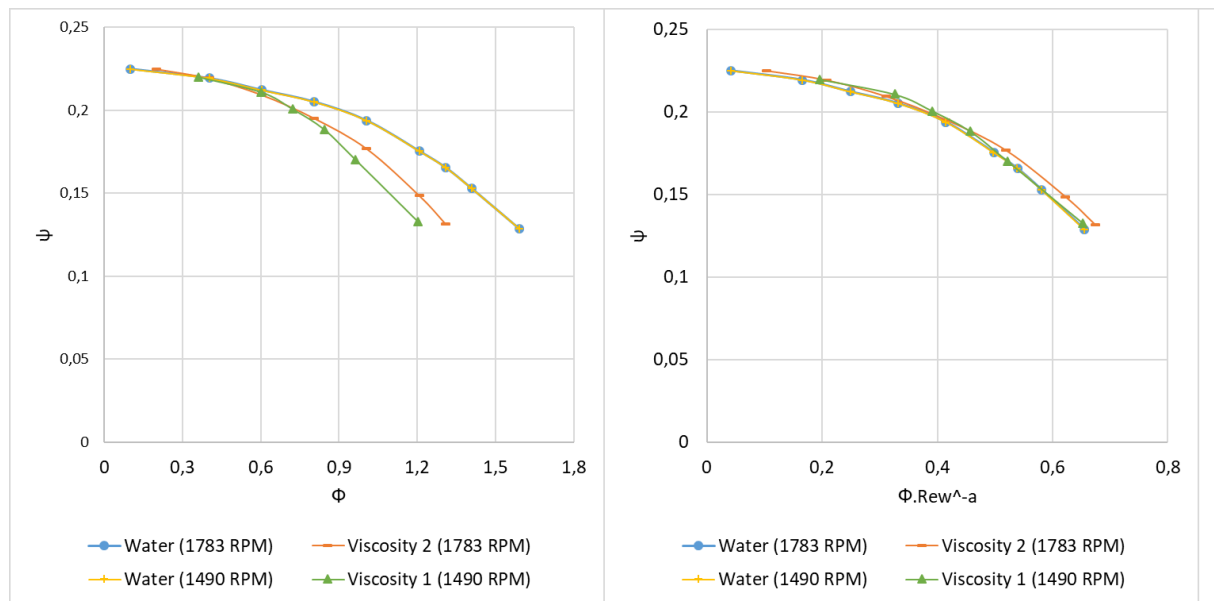


Figure 22: Morrison's modified affinity law charts with data based on Le Fur⁴⁹

The advantages are that all different cases overlap in one single curve. The flow coefficient (ϕ_{visc}) for the viscous situation is calculated from the resulting relationship $\phi_{\text{water}} * \text{Re}_{\text{water}}^{-a(\text{water})} = \phi_{\text{viscous}} * \text{Re}_{\text{visc}}^{-a(\text{viscous})}$. This method requires only the knowledge of the pump specific speed and the rotational Reynolds number and no experimental data, except maybe for validation purposes.

2.5.6 Manufacturers' Correction Factors and Detailed Procedures

Some pump manufacturers have also developed in-house viscosity correction factors and provide tables for a wide range of viscosities. For example, Centrilift (Baker Hughes) publishes such tables (Table 4). The Saybolt seconds universal unit (SSU) is calculated with Eq.47⁵⁰:

$$SSU = 2.273 \times \left(cSt + \sqrt{cSt^2 + 158.4} \right) \quad (\text{Eq. 47})$$

where the liquid viscosity is given in SSU and calculated from the fluid viscosity in cSt.

⁴⁹ Le Fur, B., M. Cato Knutsen, and C. Becki. 2015. High Viscosity Test Of A Crude Oil Pump. [online] URL: <http://www.eureka.no/wp-content/uploads/2016/02/lecture-project-V30-2.pdf>.

⁵⁰ Takács, G. 2009. *Electrical submersible pumps manual: Design, operations, and maintenance*. Gulf Professional Publ./Elsevier, Amsterdam.

Table 4: Centrifugal viscosity correction factors⁵¹

Viscosity (SSU)	Correction Factors			
	Capacity	Head	Efficiency	BHP
50	1.000	1.000	0.945	1.058
80	0.980	0.990	0.870	1.115
100	0.970	0.985	0.825	1.158
150	0.947	0.970	0.736	1.248
200	0.924	0.958	0.674	1.341
300	0.886	0.933	0.566	1.460
400	0.847	0.909	0.497	1.549
500	0.819	0.897	0.462	1.590
600	0.792	0.883	0.434	1.611
700	0.766	0.868	0.410	1.622
800	0.745	0.858	0.390	1.639
900	0.727	0.846	0.368	1.671
1,000	0.708	0.833	0.349	1.690
1,500	0.659	0.799	0.307	1.715
2,000	0.621	0.771	0.272	1.760
2,500	0.590	0.750	0.245	1.806
3,000	0.562	0.733	0.218	1.890
4,000	0.518	0.702	0.278	2.043
5,000	0.479	0.677	0.149	2.176

Similar to the table above, Ippen (1946) produced viscosity correction charts for specific pump types and sizes (Ippen 1946). Furthermore, Gülich proposed different approaches to centrifugal pump performance correction. For example, loss analysis is a very detailed and accurate procedure (Gülich 2014). However, it requires a considerable amount of input data and might be feasible for single stage centrifugal pumps, but not for much more complex multistage ESPs.

2.6 Performance Prediction for Non-Newtonian Fluids

Non-Newtonian fluids and their rheological characteristics are much more complex and very difficult to model. Takas (2009) recommends complete ESP performance tests, performed with a non-Newtonian fluid under investigation. Nevertheless, a few publications can be found related to viscous pump performance degradation using non-Newtonian fluids. However, all of them are based on single-stage centrifugal pumps, mainly in the laminar flow regime. It is not clear whether these approaches hold if transferred to multistage ESPs and highly turbulent flow.

2.6.1 Walker and Goulas

Walker and Goulas (1984) applied the Hydraulic Institute method. The only difference was that they used a representative viscosity value for the calculations. Therefore, they replaced

⁵¹ Takács, G. 2009. *Electrical submersible pumps manual: Design, operations, and maintenance*. Gulf Professional Publ./Elsevier, Amsterdam.

the kinematic viscosity against the plastic viscosity of their investigated Bingham fluid (Walker and Goulas 1984). In the case of shear-thinning fluids, one option would be to use the apparent or limiting viscosity for the performance prediction. Additionally, as the viscosity of non-Newtonian fluids is a function of the shear rate, a characteristic pump shear rate should be defined, which they suggested between 100 s^{-1} and 1500 s^{-1} (Buratto et al. 2017).

2.6.2 Pullum and Graham

Pullum's et al. (2007) approach also draws on the Hydraulic Institute method. The author proposed an "equivalent pipe" representing the centrifugal pump, which models the complex flow behavior inside the pump (Pullum et al. 2007). This "pipe" is based on the pump geometry and can be used to determine a suitable shear rate, which in return provides a representative viscosity. Eq.48 – Eq.49⁵² give the equivalent pipe diameter (D_h) and the "pipe" velocity (V):

$$D_h = \frac{4 \times w \times \pi \times D_{imp}}{2 \times (\pi \times D_{imp} + w)} \quad (\text{Eq. 48})$$

$$V = \frac{4 \times Q}{\pi \times D_h^2} \quad (\text{Eq. 49})$$

where Q is the flow rate, and w is an experimentally determined pump characteristic dimension. The first step is to assume an initial value for the characteristic dimension and calculate the pump head with the HI Method. Next, a global non-linear minimization procedure is applied, which corrects w and minimizes the error between the experimental head data and the calculated one (Graham et al. 2009) This characteristic dimension can be used for different fluids but only for the same pump (Buratto et al. 2017).

Next, the shear rate for the laminar flow case is calculated with the Rabinowitsch-Mooney equation, given by Eq.50⁵³. Finally, the apparent viscosity can be determined from the shear rate. In the case of turbulent flow ($\dot{\gamma} > 4000 \text{ s}^{-1}$), the limiting viscosity should be used. The last step is then a straight-forward application of the HI Method using the acquired viscosity value (Pullum et al. 2007).

$$\dot{\gamma} = \left(\frac{3 \times n' + 1}{4 \times n'} \right) \times \frac{8 \times V}{D_h} \quad (\text{Eq. 50})$$

⁵² Pullum, L., L. Graham, and M. Rudman. 2007. Centrifugal pump performance calculation for homogeneous and complex heterogeneous suspensions. *The Journal of The Southern African Institute of Mining and Metallurgy* 107:373–379. [online] URL: https://journals.co.za/content/saimm/107/6/AJA0038223X_3327.

⁵³ Pullum, L., L. Graham, and M. Rudman. 2007. Centrifugal pump performance calculation for homogeneous and complex heterogeneous suspensions. *The Journal of The Southern African Institute of Mining and Metallurgy* 107:373–379. [online] URL: https://journals.co.za/content/saimm/107/6/AJA0038223X_3327.

where n' is the slope of the log-log plot of τ_0 versus the pseudo shear rate ($8.V/D_h$).

Walker and Goulas (1984) reported head and efficiency accuracies of ± 5 percent between test and predicted data (Walker and Goulas 1984). Pullum (2007) and Graham (2009) achieved accuracies of ± 10 percent for the head data and stated an average value of 25% for w/D_{imp} . Kalombo (2014) conducted similar tests and used both techniques to evaluate the prediction accuracy compared to his experimental data. However, the accuracies obtained by the author did not match the anticipated limits and were inferior to the published data in the earlier mentioned papers (Kalombo et al. 2014).

2.6.3 Sery and Kabamba

Sery and Kabamba (2006) proposed a third method. They calculate the viscosity from the underlying rheology model based on the average shear rate of the pump impeller (Buratto et al. 2017). The concept described by Metzner and Otto (1957) was used, which suggests that the impeller's average shear rate is in linear relation⁵⁴ to the rotational speed of the impeller (Metzner and Otto 1957).

$$\dot{\gamma}_{avg} = k \times N \quad (\text{Eq. 51})$$

where $\dot{\gamma}_{avg}$ is the average shear rate (1/s), N represents the rotational speed (1/s) and, k is an impeller specific proportionality constant (-). It should be mentioned that Metzner's and related work focuses on agitator impellers rather than actual centrifugal pumps.

2.7 Polymer Effects and Expectations on the Pump Performance

Demin et al. (2004) concluded, after a polymer flood in the Daqing field, that the energy efficiency of their ESPs decreased over 50% during back-production of the polymer (550 mg/L PAM) solution. Besides, the highly viscous fluid reduced the service lifetime of their pumps by one-half (Demin et al. 2004). The reason for this issue can be explained by looking at Figure 23:

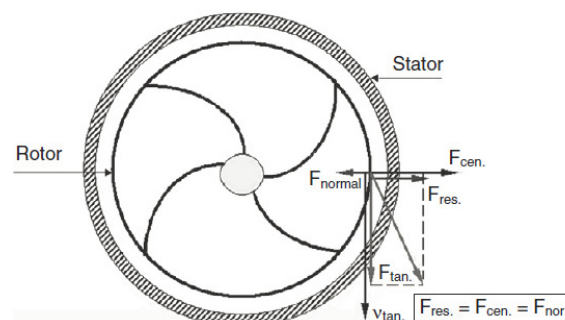


Figure 23: Viscoelastic fluid effect on centrifugal pumps⁵⁵

⁵⁴ Metzner, A. B., and R. E. Otto. 1957. Agitation of non-Newtonian fluids. *AIChE Journal* 3(1):3–10.

⁵⁵ Demin, W., J. Youlin, W. Yan, G. Xiaohong, and W. Gang. 2004. Viscous-Elastic Polymer Fluids Rheology and Its Effect Upon Production Equipment. *SPE Production & Facilities* 19(04):209–216. [online] URL: <https://doi.org/10.2118/77496-PA>.

Centrifugal pumps rotate with high speed, causing a centrifugal force (F_{cen}). Nevertheless, the viscoelasticity of PAM-polymer fluids also creates a normal force (F_{normal}) pointing in the opposite direction. Together, they result in a lower cumulative force (F_{res}), causing a reduced pump fluid head, while at the same time reducing the efficiency. In order to compensate for the lost fluid head, more electric energy would be required (Demin et al. 2004).

The viscous pump tests will be conducted with KCl-brine and different HPAM concentrations. The HPAM mixed with the iron-free brine is expected to be stable during the transport to the test facility. The highest polymer concentration of 2000 ppm is expected to have a maximum viscosity of 26 cP at 30°C. We expect a head curve degradation, meaning we would produce less fluid at a constant head compared to the water performance. Additionally, we await an increasing power consumption, resulting in a lower pump efficiency. Moreover, we believe that the turbulence and high shear forces within the impellers and diffusers will cause a breakdown of the polymer chains. The result would be a lower-viscous fluid leaving the pump than entering it.

3 Methodology

This chapter gives a description of the pump test facility setup, the electric submersible pumps, the fluids under investigation, and the testing procedure. One of the biggest issue with setting up a testing facility is that the pump manufacturers do not disclose their way of performing performance tests.

3.1 Experimental Setup (Pump Test Facility)

The pump flow loop was newly built for the purpose of testing ESPs within viscous fluid conditions. The detailed specifications and pictures of all components of the pump test facility are listed in Appendix A. A fully-closed flow loop is used for fluids, which are not affected by molecular shear destruction (e.g., water or oil), as illustrated by the “water loop line“ or later also called “closed-loop” in Figure 24.

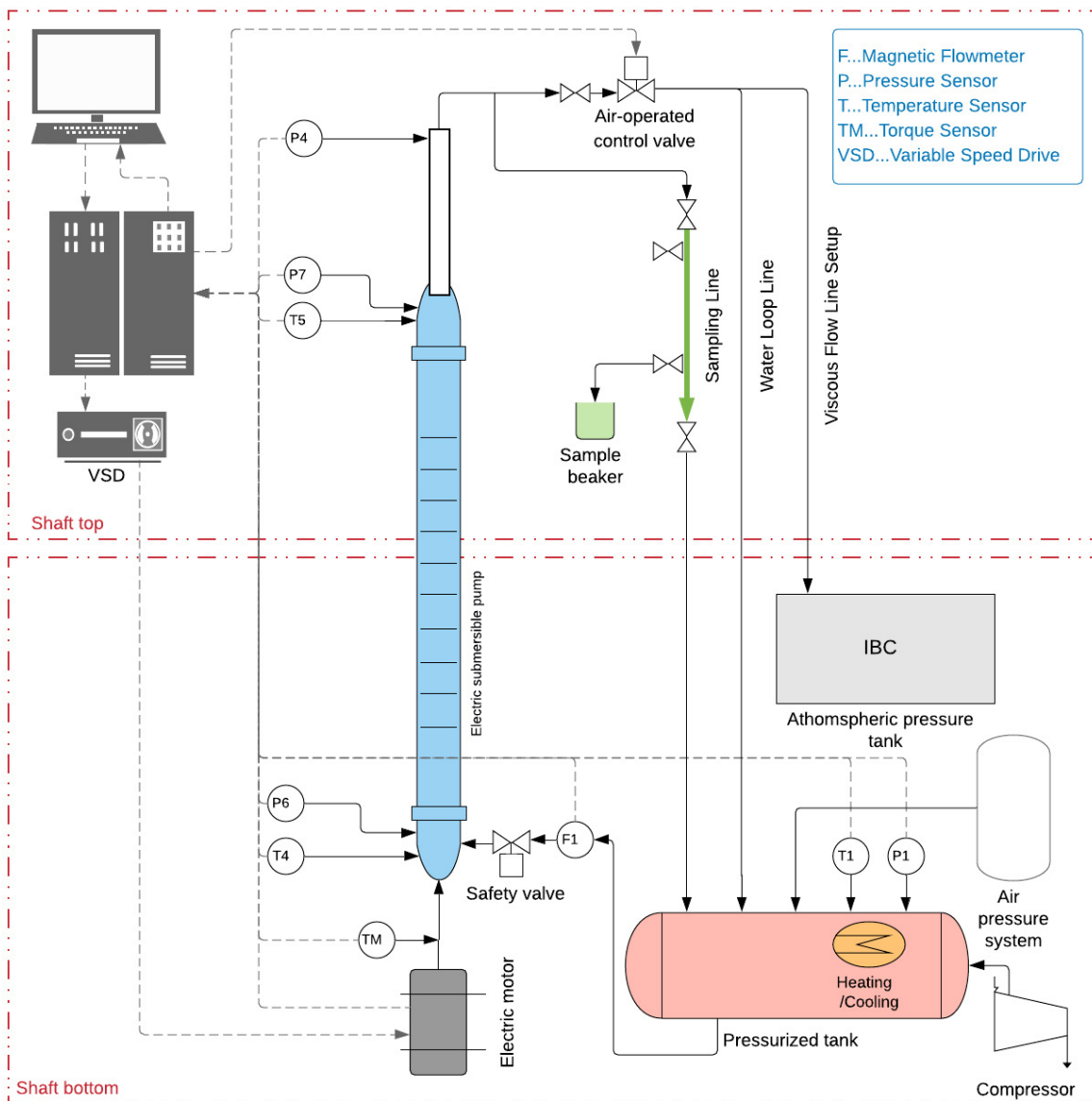


Figure 24: Pump test facility – flow loop

In case of fluids, which are affected by shear destruction (e.g., polymer-laden fluids), it is not reasonable to pump the liquid in a closed-loop, because the shear forces inside the pump would alter the polymer chains continuously. Therefore, it was necessary to modify the setup for those experiments. The polymer tests consist of only one single flow circle from the pressurized “reservoir” tank into a second independent tank (i.e., intermediate bulk container), illustrated by the “viscous-flow line setup” or later called “open-loop”. This setup ensures the acquisition of reliable data based on unsheared polymer solution properties.

In the testing loop, we do not use a booster pump to establish the required pump intake pressure. A booster pump would alter the polymer molecular chains before entering the ESP. As one investigation target is exactly the ESP’s shear effect on the polymer solution, a pressurized tank provides the required intake pressure. In case of the closed-loop setup, an air compressor builds up the prescribed pressure inside the tank. In contrast, for the viscous-test setup, the liquid level in the tank will drop during the pumping operation, and more air volume needs to be compressed. As the capacity of the compressor alone is too low, an additional air-pressure bottle system keeps the intake pressure at a constant value during the tests.

Another crucial issue is the sampling of the polymer solution for the viscosity measurement. The shear forces within the pneumatic control valve, located after the ESP, would again shear the polymer mixture properties. Therefore, a 4-valve sampling device was designed to minimize those shear effects. Chapter 3.2.3 describes the sampling device construction and sampling procedure in detail.

3.1.1 Test Pumps

The first tested ESP is a REDA D2100EZ (Schlumberger) 400 Series with 82 stages, which is able to produce a head of 857 m at 3,500 rpm. It has a mixed flow impeller with an outer diameter of 81.3 mm. At the best efficiency point, the pump delivers 2,100 bpd at 3,500 rpm. The recommended operating range at 3,500 rpm is 1,400 bpd to 2,650 bpd flow rate, and its specific speed is around 2,300 (n_s in US units) at the BEP. The manufacturer’s pump reference curves can be found in Appendix B.

The second ESP is a REDA D2400N (Schlumberger) 400 Series with 7 stages, which can produce a head of 81 m at 3,500 rpm. It has a mixed flow impeller with an outer diameter of 81 mm. At the best efficiency point, the pump delivers 2,400 bpd. The recommended operating range at 3,500 rpm is 1,500 to 3,200 bpd (199 to 424 m³/d at 2,917 rpm) flow rate. The pump’s specific speed is around 2,600 (n_s in US units) at the BEP. The manufacturer’s pump reference curves can be found in Appendix B.

3.2 Experimental Program

This chapter describes the testing procedure for the various fluid types and the prevailing test conditions.

3.2.1 Test Fluids and Experimental Matrix

In order to verify the manufacturer's pump reference curves, freshwater was used at ambient temperature. The subsequent viscous performance tests use salt water (3%-KCl brine) with different polymer concentrations. The brine has a total salinity of around 30,000 ppm KCl and is mixed with a hydrolyzed polyacrylamide (HPAM). The trade name of the polymer is SNF FLOPAAM HPAM 3630S. It has an approximate molecular weight of 20 million Daltons (g/mole) and a hydrolysis rate of 20-30 mole percentage. The different polymer test concentrations are listed in the experimental matrix (Table 5).

Table 5: Experimental Matrix and Boundary Conditions

Test Pump	Fluid Type	Polymer Con. [ppm]	Temp. [°C]	Intake Pres. [bar]	Frequency [Hz]	Add. Information
REDA D2100EZ	Freshwater	0	Ambient (16°C)	5 (from intake pressure analysis)	58.33 (3500 rpm) 55 45 35	Test Points: Shut-in 40% of Q_{BEP} Q_{minRR} 85% of Q_{BEP} Q_{BEP} 115% of Q_{BEP} Q_{maxRR} 140% of Q_{BEP} 160% of Q_{BEP} Open and closed loop tests with pressure measurement at the pump intake and discharge
	Brine (3% KCl) + Polymer (HPAM Flopaam 3630S)	2000 1000 500	Variable (25°C, 20°C, 15°C)	5	55 45 35	
REDA D2400N	Freshwater	0	Ambient (16°C)	5	55 48.62 (2917 rpm) 45 35	
	Brine (3% KCl) + Polymer (HPAM Flopaam 3630S)	1000 500	Ambient (16°C)	5	45	

REDA D2400N	Freshwater	0	Ambient (15°C)	5	48.62 (2917 rpm) 45 35	Open and closed loop tests with pressure measurement at the pump intake and discharge and also at each single pump stage
	Brine (3% KCl) + Polymer (HPAM Flopaam 3630S)	1000	Ambient (20°C)	5	45	

Table 6 summarizes the range of parameters measured for each fluid type during the test or later in the lab.

Table 6: Measurements

Freshwater	Brine + Polymer
Pressure	Pressure
Temperature	Temperature
Flowrate	Flowrate
Motor torque	Motor torque
	Density (OMV lab)
	Viscosity (MUL and OMV lab)
	Molecular weight (OMV lab)

3.2.2 Test Procedure

All test curves are obtained under constant fluid temperature, constant rotational speed, and constant intake pressure. The pump's rotational speed is ramped up with 2 seconds per 1 Hz until the target frequency is reached. The fluid is circulated in a closed-loop while various points on the head curve are recorded according to API RP 11S2. For each point, the sensor measurements are recorded for a pre-defined period until a stabilized flow regime has developed, in order to get representative pressure and flowrate data. In the case of the open-loop tests, the number of test points is based on the volumetric limitations (1,500 liters) caused by the tank size and available polymer solution volume. The tests start at shut-in conditions, and then the pneumatic valve opens step by step along the head curve. This approach offers better control over the liquid rate, in contrast to a procedure in the reverse direction. In addition, the pump performance trials from open-flow conditions to the shut-in point show slightly less data quality.

After the performance tests with water, the pump loop was modified to the "open-loop" setup. The reliability of this setup was again tested with freshwater, and the data were compared

with the closed-loop measurements. Next, the polymer solution experiments were started. In general, the following steps were performed for each polymer concentration:

1. General test preparations with 2,000 ppm, 1,000 ppm, and 500 ppm polymer solutions made from 3% KCl-brine and HPAM powder. The detailed process is explained in Appendix E.
2. Sampling of the unsheared viscous fluid.
3. Filling the “reservoir” tank with 1,500 liters polymer solution.
4. Conducting the pump test and taking fluid samples (explained in Chapter 3.2.3) during the tests at each frequency. All sensor data were stored on a server for later processing.
5. Viscosity measurement of the different fluid samples at the test temperature using a rotational viscometer on-site (Brookfield) and in the lab (Anton Paar Physica MCR 501 Rheometer).
6. Molecular weight determination of the samples in the lab (OMV, Gänserndorf).

3.2.3 Liquid Sampling Procedure and Measurement

The sampling of the polymer-laden fluid during the test is one of the most critical parts of the experiments. First of all, it was not possible to pump the liquid in a loop like in the tests conducted with water. This is due to the fact that the polymer molecular chains are broken down inside the centrifugal pump. As a result, the unshared polymer in the pressurized tank would be mixed with the back-produced sheared polymer mixture. This mixing would decrease the overall viscosity and falsify the pump performance data. Therefore, the ESP-sheared polymer had to be pumped into another tank, disconnected from the initial mixture. The next problem was the pneumatic-regulation valve after the ESP, whose purpose is to control the flow rate. Similar to the pump, this choke creates shear forces on the polymer chains. Hence, it was not possible to sample the polymer fluid from the second tank after the choke, because the investigation targets the molecular chain degradation caused by the ESP. Therefore, the polymer mixture had to be sampled directly after the ESP and before the regulation valve. Two main issues were associated with this setup. One is that the D2100EZ pump builds pressures up to 85 bars, with intake pressures of 5 bars; this would mean peak pressures of 90 bars at shut-in conditions. Secondly, as shearing-off effects had to be avoided by any valve, it was not possible to tap the fluid at a single valve.

The solution was to build a 4-valve sampling system. The test fluid enters the sampling line through a bypass. Then the liquid enters the sampling device (see Figure 24).

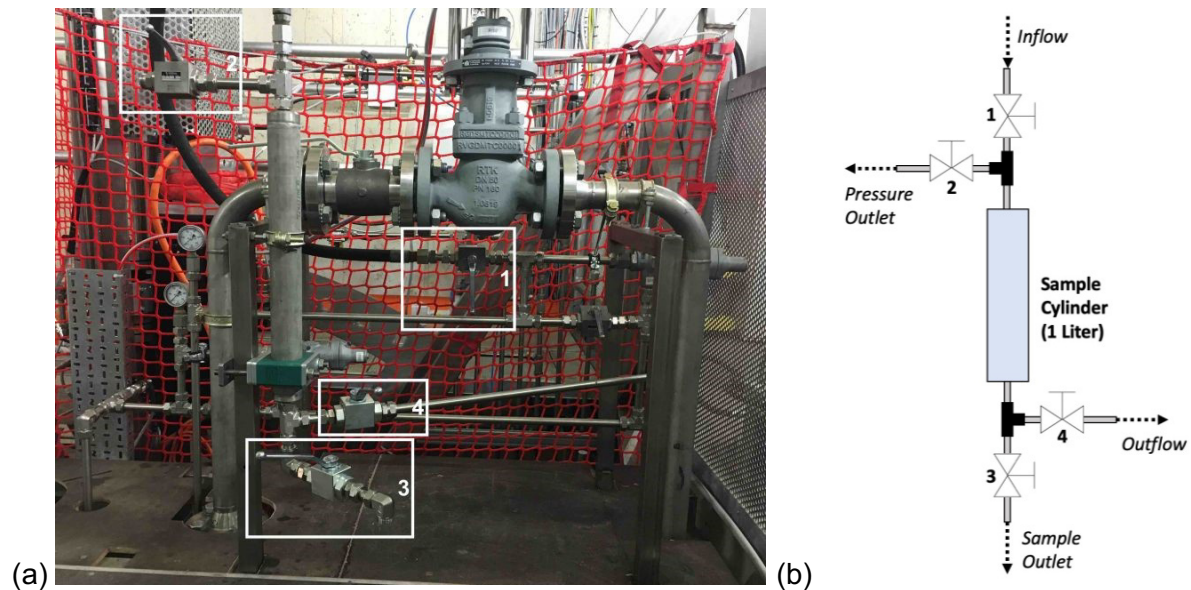


Figure 25: (a) Sampling device mounted in the facility, (b) Schematic of the sampling device

The fluid sampling is done at the minimum recommended flowrate ($Q_{\min RR}$) and the best efficiency flow rate (Q_{BEP}). The sampling process follows steps 1.-7.:

1. At the beginning of the sampling procedure, all valves are closed.
2. Then valve 1 is slowly opened, allowing the fluid to enter the sampling chamber.
3. Next, valve 4 is slowly opened, so that the ESP-sheared fluid replaces the pre-sheared fluid (sheared by valve 1) in the sampling chamber.
4. Now, having only ESP-sheared fluid in the sampling chamber, first, valve 4 and subsequently valve 1 is closed.
5. With the help of valve 2, the pressure inside the sample chamber can be released.
6. Finally, the target fluid is extracted by opening valve 3.
7. As soon as the sample chamber is fluid free, valves 3 and 2 are closed, and the process starts from the beginning.

Immediately after a new sampling process, the first viscosity measurements were carried out on-site with a Brookfield viscometer. The following days, additional viscosity measurements were performed with an Anton Paar Physica MCR 501 Rheometer using a double gap geometry cylinder-cup. Detailed information about the measuring principle can be found in Appendix D.

3.3 Data Acquisition

The data acquisition is based on a programmable logic controller (PLC) and various sensors. The PLC consists of various analog and digital input/output modules. The analog signals (e.g., from the pressure sensor, temperature sensor) use a current of 4 to 20 mA, which can be converted into engineering units (e.g., bar, °C, Nm, etc.) for each sensor type. The data acquisition program and the graphical user interface are written in LabVIEW. The raw data is continuously stored on a server and can be extracted for the period desired.

3.4 Pump Performance Curves

In this thesis, the pump performance plots in the Results Section (Chapter 4) will comprise of three main curves types. First, there is the “(Catalogue) Reference Curve”, which is the curve published by the pump manufacturer for a specific rotational speed. Second, there is the “(Affinity Law) Reference Curve”, which is the performance curve for a specific rotational speed. The manufacturer does not publish the performance curve with this speed. Therefore, the “Affinity Laws” described in Chapter 2.3 are used for conversion. Lastly, there is the “Polynomial Model”, which is a higher order polynomial fit of the obtained experimental data points.

3.5 Data Processing

The raw sensor data are cleaned in various steps in Microsoft Excel and MATLAB. The processing steps include, e.g., removing non-representative unstable data, removing outliers, averaging, unit conversions, or curve fitting. To sum up, with the help of all the sensor data and lab measurements, the pump head, the pump hydraulic power, and the brake horsepower were calculated in total and as well as per stages. The pump head is calculated, as shown in Eq. 52:

$$Head = \frac{\Delta p_{pump}}{g \times \rho} \quad (\text{Eq. 52})$$

where H is the pump head (m), ΔP_{pump} (Pa) is the pump discharge pressure minus the pump intake pressure, g represents the earth acceleration (m/s^2), and ρ is the fluid density (kg/m^3).

The hydraulic power of the pump is calculated, as shown in Eq. 53:

$$P_{hydr} = \frac{\Delta p_{pump} \times Q}{36} \quad (\text{Eq. 53})$$

where P_{hydr} is the pump hydraulic power (kW), ΔP_{pump} (bar) is the pump discharge pressure minus the pump intake pressure, and Q represents the flow rate (m^3/h).

The motor power or pump input power is calculated with Eq. 54:

$$BHP = \frac{T \times N}{9,549} \quad (\text{Eq. 54})$$

where BHP is the brake horsepower (kW), T is the torque (Nm) applied to the pump, and N represents the rotations per minute (RPM).

Lastly, the pump efficiency is calculated, as shown in Eq. 55:

$$EFF_{pump} = \frac{P_{hydr}}{BHP} \quad (\text{Eq. 55})$$

where EFF_{pump} , the pump efficiency (-), is the hydraulic power (kW) divided by the brake horsepower (kW).

4 Results

This chapter presents the results acquired during the pump experiments.

4.1 Sensitivity Analysis – Intake Pressure with Water

First, a sensitivity analysis for different pump intake pressures was conducted. Two main reasons were associated with this analysis. One was that there is no information about a minimum required intake pressure for the tested pumps available. A too low suction pressure could lead to cavitation and the resulting damage of the impeller blades. In the oilfield, a minimum intake pressure is usually desired to keep the associated gas in solution. The second reason was related to the testing facility. A lower intake pressure would mean less HSE-risk during the testing operations. In addition, all pipe and equipment sealing would be less stressed, and their lifetime enhanced. The last reason was that the flow loop does not have a booster pump to establish the intake pressure. Therefore, the lower the required suction pressure, the easier the compressor and air-pressure bottle system can handle the pressure variations.

Figure 26 shows the experiments for 35 Hz rotational speed. The tested intake pressures are 5, 10, and 15 bars. The tests showed that there is no difference in the pump performance between the various suction pressures.

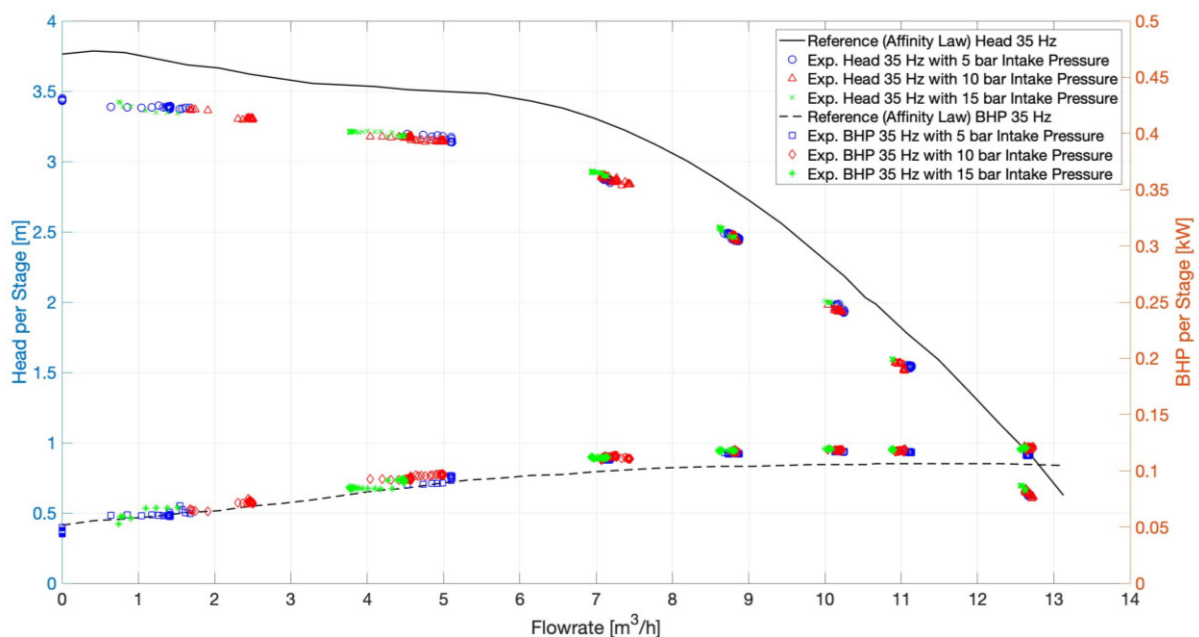


Figure 26: Intake pressure analysis with 35Hz rotational speed (REDA D2100EZ)

The 45 Hz experiments show a similar picture that there is no apparent difference in pump performance. For 55 Hz rotational speed, only 5 and 10 bar intake pressure were tested because of the higher total pressure at the pump discharge. Both cases show the same pump performance for different intake pressures again.

4.2 Reference Pump Performance Curves with Water

The following sub-chapters show the manufacturers' reference curve, compared with the experimental data for the tested pumps.

4.2.1 REDA D2100EZ

Figure 27 shows the pump performance for the closed-loop setup at 3,500 rpm. The electric motor in the testing facility is fully controlled with a variable speed drive, and therefore, slippage is not an issue. Without slippage, 60 Hz would result in 3,600 rpm. However, the manufacturer's catalog curves are based on 60 Hz and 3,500 rpm operating speed. Therefore, the validation experiments have been conducted with 58.33 Hz, which are 3,500 rpm without motor slippage.

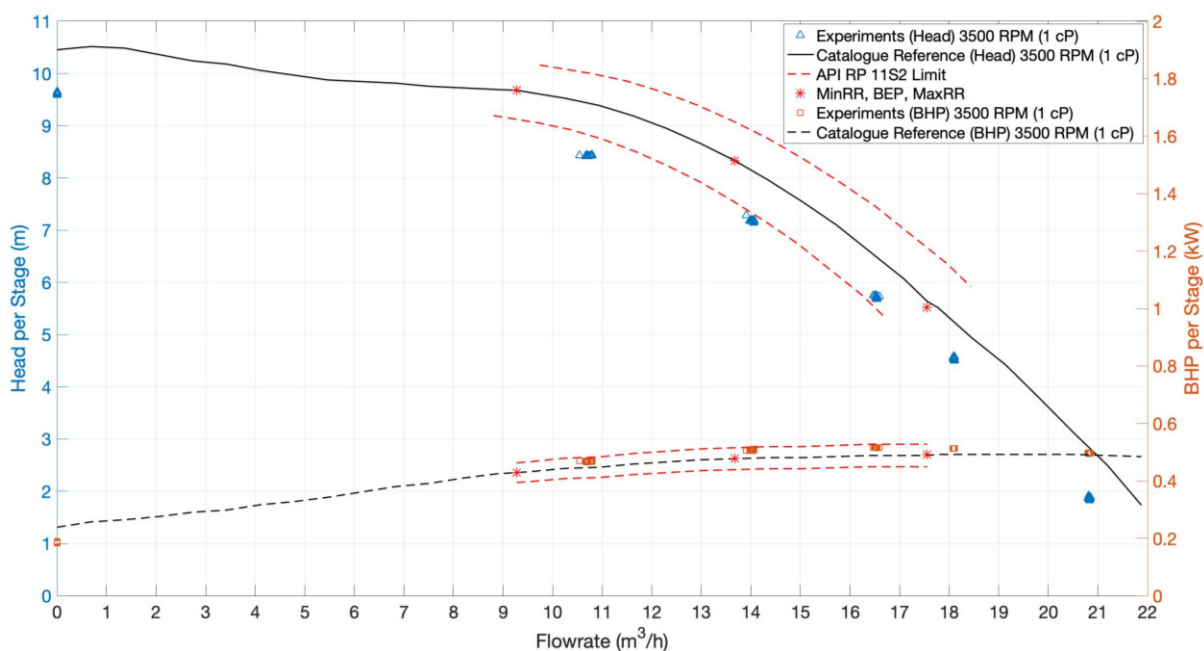


Figure 27: REDA D2100EZ head and brake horsepower curve – catalog versus 3500 RPM closed-loop experiments with water (1 cP and 1 S.G.)

The plot shows that the test head performance is slightly below the manufacturer's reference over the entire testing range, while the test brake horsepower is slightly above the benchmark. At higher flow rates, the experimental head data are, to the most part, within the API limits. Only at smaller flowrates, the head performance is below the API limit. It should be mentioned that it was very complicated to record stable data at low flow rates because the head differences from shut-in to the minimum recommended range flowrate are relatively small. The limiting factor was the pneumatic regulating valve, which made it challenging to capture small pressure changes at this overall high-pressure level, and establish a stable flow at this high rotational speed. Next, the dashed black line shows the brake horsepower for 3,500 RPM. The brake horsepower is the product of the rotational speed times the torque applied to the pump. The torque is measured with a torque sensor, which is attached to the shaft between the electric motor and the pump. In case of the brake horsepower, the test

data are above the benchmark, but still perfectly within the API limits. Lastly, the pump efficiency is simply the hydraulic power divided by mechanical power. Since the head performance is lower than the expected head and the brake horsepower slightly higher, decreased efficiencies can be observed. Additional plots can be found in Appendix C.

Next, the pump was tested with 35, 45, and 55 Hz rotational speed. The reference curves for those speeds are calculated with the help of the affinity laws. The underlying reference speed for the calculations was 3,500 rpm (58.33 Hz). The experiments with the lower frequencies show a similar trend as the 3,500-rpm tests. Figure 28 shows the head performance curves for the closed-loop runs.

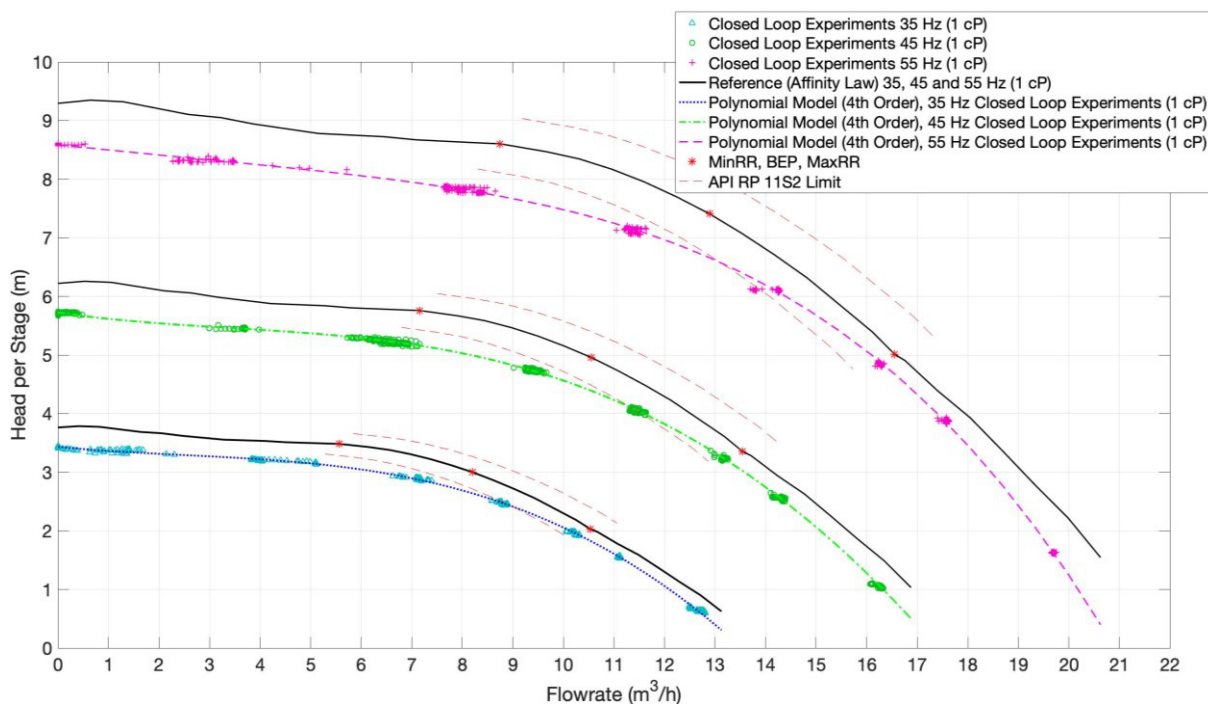


Figure 28: REDA D2100EZ head Curve – catalog versus 35, 45 and 55 Hz closed loop Experiments with water (1 cP and 1 S.G.)

At zero flow rate, the pressure difference between the pump intake and discharge is approximately about 6 percent below the reference value, which can be seen in the head per stage deviation from the reference curves. All experimental data are parallel below the manufacturer's performance. Banjar (2013) and Solano (2009) report a similar deviation from the catalog curve for their tests. The actual reason for this discrepancy is not entirely clear. One explanation could be the test and measurement setup, which might be different from the manufacturer's approach. Unfortunately, no information about the manufacturer's test setup is available. Another reason could be mechanical problems with the pump and its stages. However, as the second ESP REDA D2400N, which is a brand-new pump, showed similar discrepancies, the reason might not be due to mechanical damages. Nonetheless, despite the head discrepancies, the experimental ESP performance will be the basis for the viscous fluid tests.

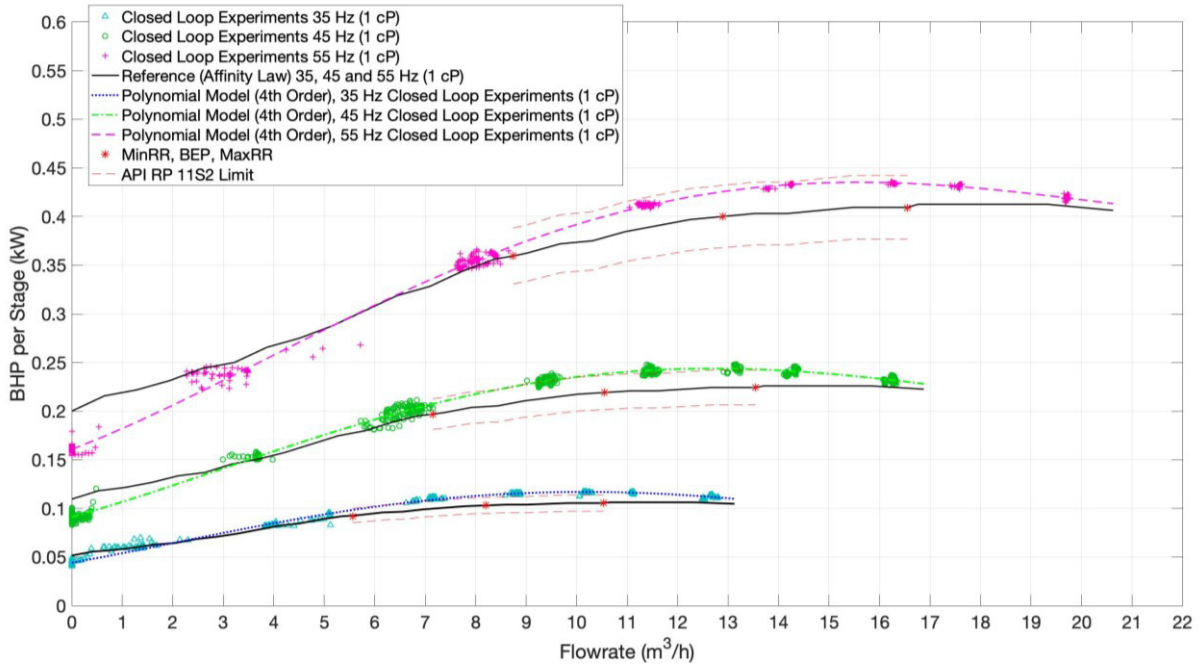


Figure 29: REDA D2100EZ brake horsepower curve – catalog versus 35, 45 and 55 Hz closed-loop experiments with water (1 cP and 1 S.G.)

Figure 29 shows the brake horsepower per stage for 35, 4, and 55 Hz rotational speed. The test data is nearly over the entire recommended operating range within the 8 percent API limits. The efficiency curves, in Figure 30, are below the 90 percent API limit. As I mentioned earlier, this can be explained by the head and brake horsepower discrepancies.

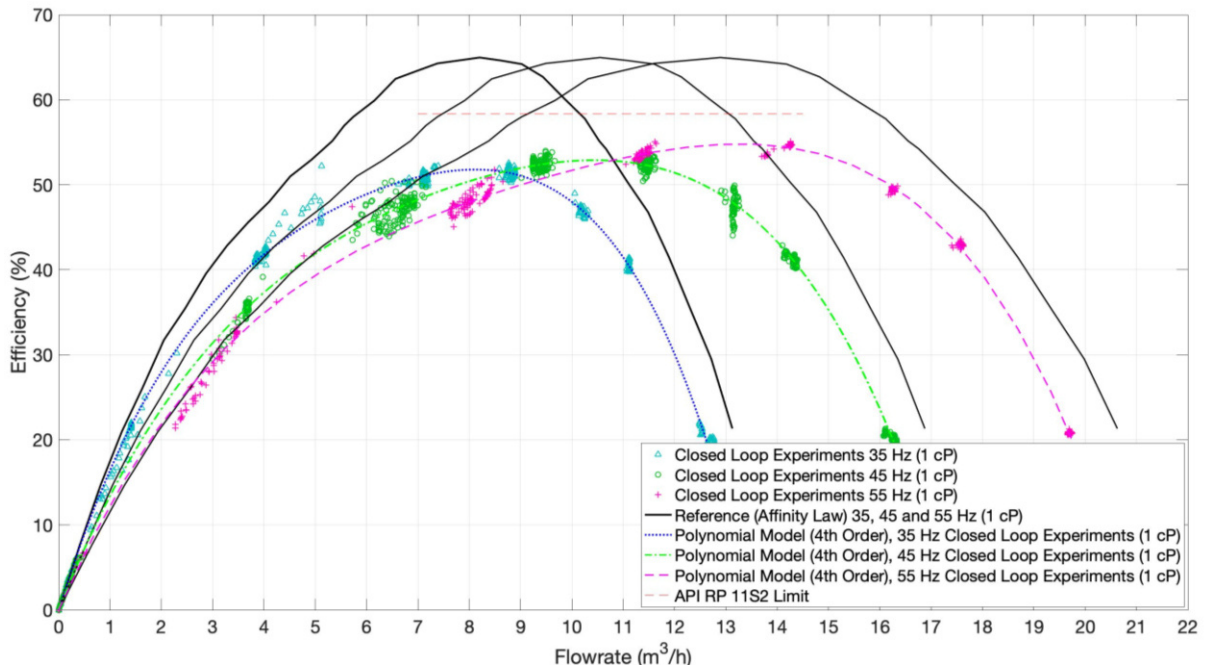


Figure 30: REDA D2100EZ efficiency curve – catalog versus 35, 45 and 55 Hz closed-loop experiments with water (1 cP and 1 S.G.)

The next step was to test the “open-loop” setup and validate the data reproducibility. The experiments showed that the open-loop test points match the polynomial closed-loop model to a very high degree. The plots can be found in Appendix C. The following equations show the final curve fitted polynomial models from the water experiments, which will be the basis for the viscous performance experiments. Eq. 56 gives the model equation for the REDA D2100EZ water head curve:

$$H \text{ per Stage } (x) = p_1 \times x^3 + p_2 \times x^2 + p_3 \times x + p_4 \quad (\text{Eq. 56})$$

With:

$$p_{1,35\text{Hz}} = -0.002292; p_{1,45\text{Hz}} = -0.001887; p_{1,55\text{Hz}} = -0.001263$$

$$p_{2,35\text{Hz}} = 0.01833; p_{2,45\text{Hz}} = 0.02125; p_{2,55\text{Hz}} = 0.01263$$

$$p_{3,35\text{Hz}} = -0.09936; p_{3,45\text{Hz}} = -0.1514; p_{3,55\text{Hz}} = -0.119$$

$$p_{4,35\text{Hz}} = 3.487; p_{4,45\text{Hz}} = 5.823; p_{4,55\text{Hz}} = 8.619$$

where H is the pump head (m), x is the flow rate in (m³/h), and p_i represents model coefficients.

The model equation for the REDA D2100EZ water brake horsepower curve is Eq. 57:

$$\text{BHP per Stage } (x) = p_1 \times x^4 + p_2 \times x^3 + p_3 \times x^2 + p_4 \times x + p_5 \quad (\text{Eq. 57})$$

with:

$$p_{1,35\text{Hz}} = 8.134 \times 10^{-6}; p_{1,45\text{Hz}} = 7.973 \times 10^{-6}; p_{1,55\text{Hz}} = 6.467 \times 10^{-6}$$

$$p_{2,35\text{Hz}} = -0.0002462; p_{2,45\text{Hz}} = -0.0002925; p_{2,55\text{Hz}} = -0.0002867$$

$$p_{3,35\text{Hz}} = 0.001676; p_{3,45\text{Hz}} = 0.002502; p_{3,55\text{Hz}} = 0.003085$$

$$p_{4,35\text{Hz}} = 0.007249; p_{4,45\text{Hz}} = 0.01162; p_{4,55\text{Hz}} = 0.01487$$

$$p_{5,35\text{Hz}} = 0.03735; p_{5,45\text{Hz}} = 0.07755; p_{5,55\text{Hz}} = 0.1546$$

where BHP is the brake horsepower (kW), x is the flow rate in (m³/h), and p_i represents model coefficients.

4.2.2 REDA D2400N

For the ESP REDA D2400N, the manufacturer’s catalog pump performance curve for 50 Hz was available, which are 2,917 rpm operating speed. As I mentioned before, our motor is fully controlled and equalizes slippage. Therefore, the experiment has been conducted with 48.61 Hz, which are 2,917 rpm.

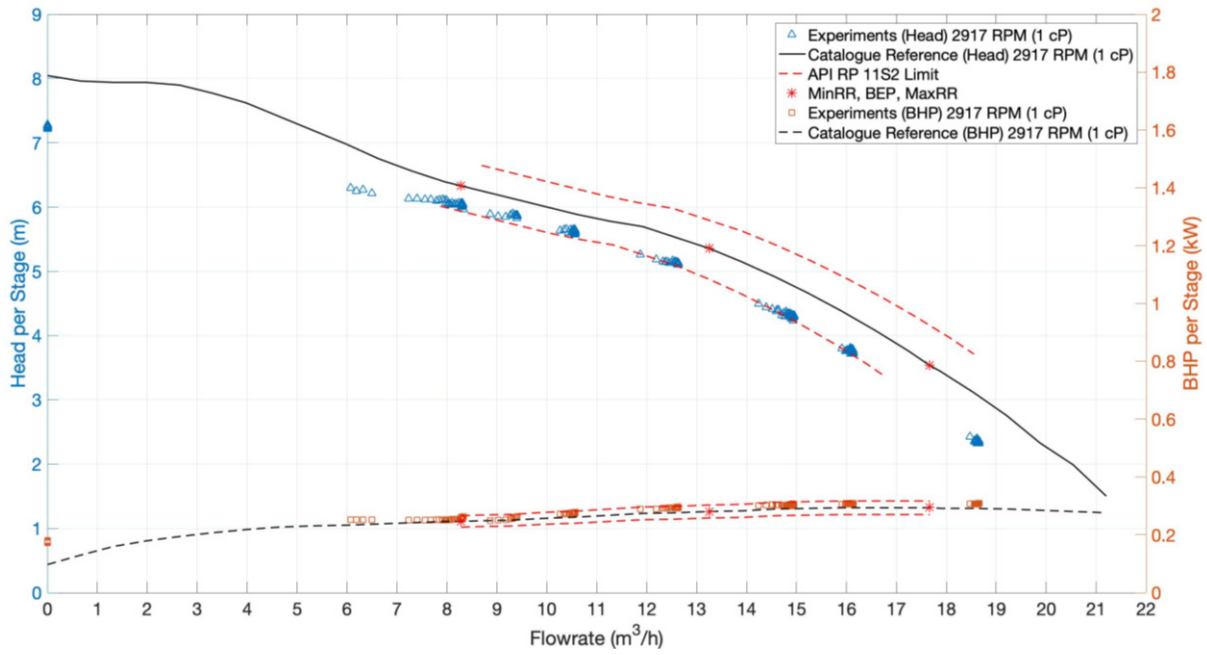


Figure 31: REDA D2400N head and brake horsepower curve – catalog versus 2917 RPM closed-loop experiments with water (1 cP and 1 S.G.)

Both head and brake horsepower are perfectly within the API Limits for the catalog speed. Comparing the data with the REDA D2100EZ pump, there is a similar trend that it was not possible to reach the catalog shut-in head and that the experimental data are consistently below the reference curve.

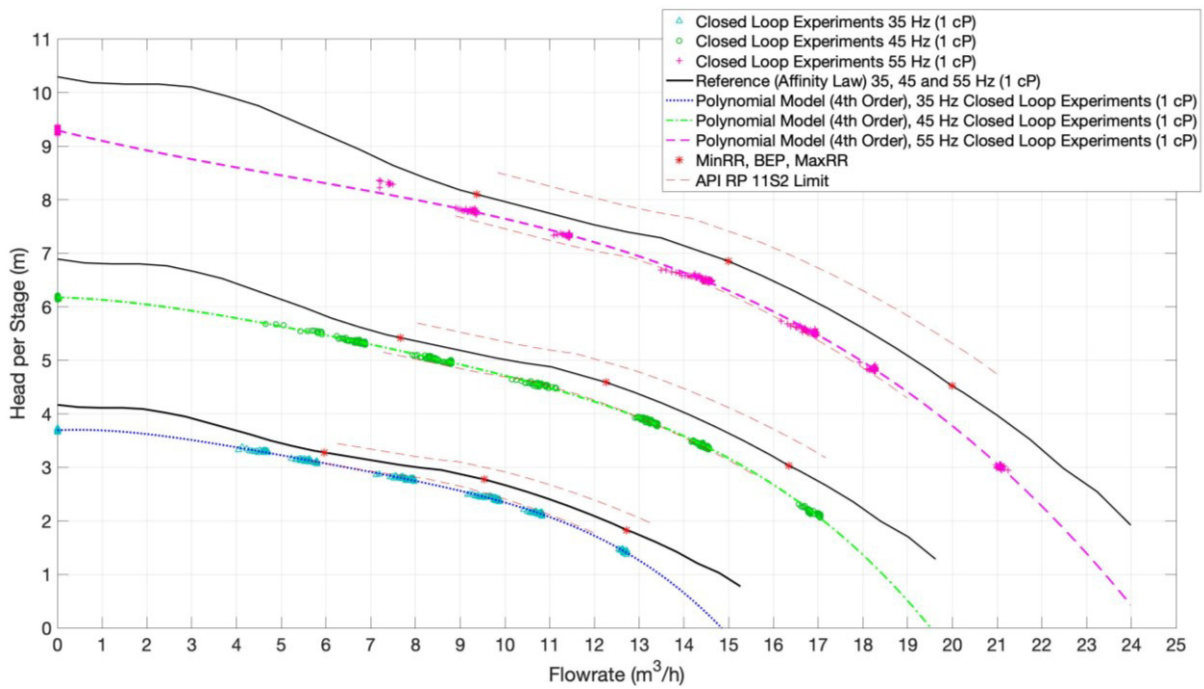


Figure 32: REDA D2400N head Curve – catalog versus 35, 45 and 55 Hz closed loop Experiments with water (1 cP and 1 S.G.)

The brake horsepower data are again within the API Limits for 45 and 55 Hz. Only for 35 Hz, the power is outside the threshold, shown in Figure 33. Another aspect is that the BHP at shut-in conditions is consistently above the manufacturer's data.

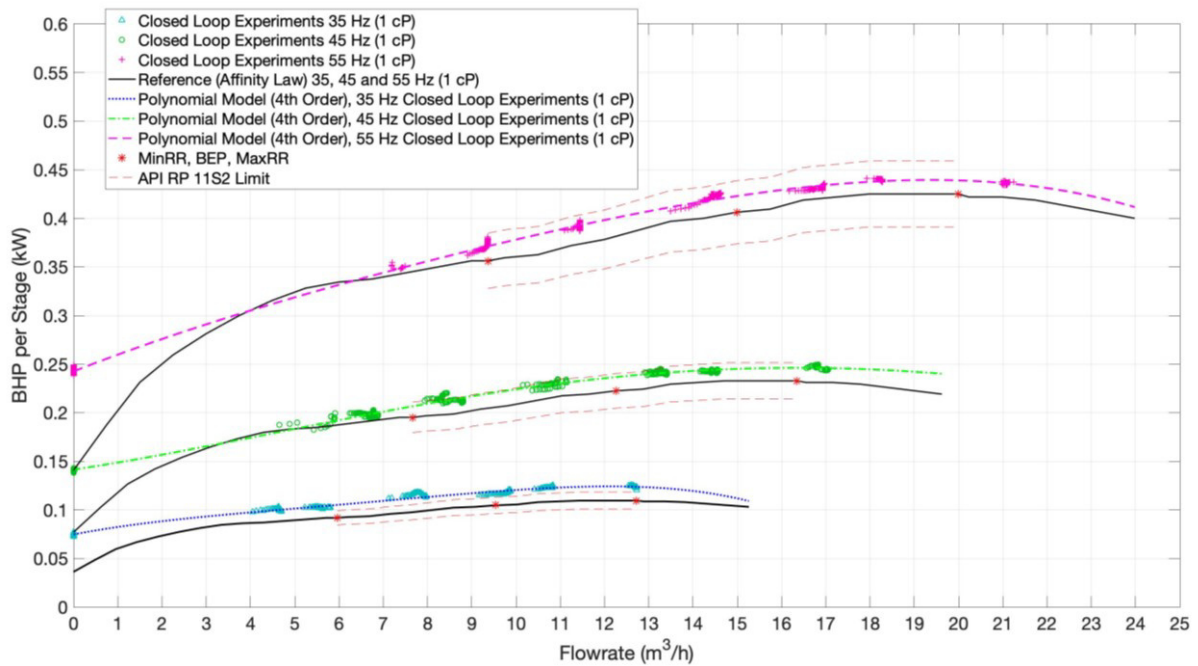


Figure 33: REDA D2400N brake horsepower curve – catalog versus 35, 45 and 55 Hz closed-loop experiments with water (1 cP and 1 S.G.)

Given the head and brake horsepower performance, it is interesting that the efficiency is better at higher frequencies.

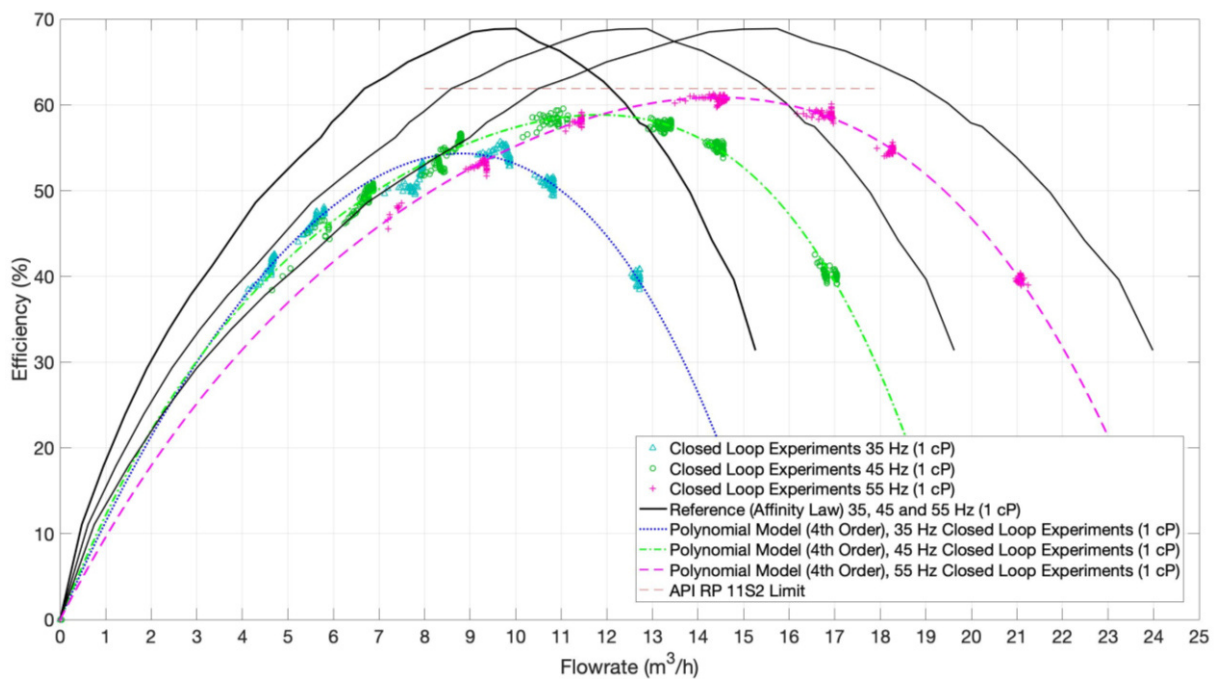


Figure 34: REDA D2400N efficiency curve – catalog versus 35, 45 and 55 Hz closed-loop experiments with water (1 cP and 1 S.G.)

The following equations show the final curve fitted polynomial models from the water experiments, which will be the basis for the viscous performance experiments. Eq. 58 gives the model equation for the REDA D2400N water head curve:

$$H \text{ per Stage } (x) = p_1 \times x^4 + p_2 \times x^3 + p_3 \times x^2 + p_4 \times x + p_5 \quad (\text{Eq. 58})$$

with:

$$p_{1,35\text{Hz}} = -0.0002262; p_{1,45\text{Hz}} = -8.518 \times 10^{-5}; p_{1,55\text{Hz}} = 5.37 \times 10^{-6}$$

$$p_{2,35\text{Hz}} = 0.005206; p_{2,45\text{Hz}} = 0.002227; p_{2,55\text{Hz}} = -0.0005943$$

$$p_{3,35\text{Hz}} = -0.04681; p_{3,45\text{Hz}} = -0.02603; p_{3,55\text{Hz}} = 0.01049$$

$$p_{4,35\text{Hz}} = 0.03882; p_{4,45\text{Hz}} = -0.02352; p_{4,55\text{Hz}} = -0.2051$$

$$p_{5,35\text{Hz}} = 3.695; p_{5,45\text{Hz}} = 6.178; p_{5,55\text{Hz}} = 9.296$$

where H is the pump head (m), x is the flow rate in (m³/h), and p_i represents model coefficients.

Eq. 59 gives the model equation for the REDA D2400N water brake horsepower curve:

$$\text{BHP per Stage } (x) = p_1 \times x^4 + p_2 \times x^3 + p_3 \times x^2 + p_4 \times x + p_5 \quad (\text{Eq. 59})$$

with:

$$p_{1,35\text{Hz}} = -5.352 \times 10^{-6}; p_{1,45\text{Hz}} = 7.033 \times 10^{-7}; p_{1,55\text{Hz}} = -1.087 \times 10^{-6}$$

$$p_{2,35\text{Hz}} = 0.0001336; p_{2,45\text{Hz}} = -4.568 \times 10^{-5}; p_{2,55\text{Hz}} = 3.551 \times 10^{-5}$$

$$p_{3,35\text{Hz}} = -0.001218; p_{3,45\text{Hz}} = 0.0005384; p_{3,55\text{Hz}} = -0.000678$$

$$p_{4,35\text{Hz}} = 0.008743; p_{4,45\text{Hz}} = 0.006736; p_{4,55\text{Hz}} = 0.01788$$

$$p_{5,35\text{Hz}} = 0.07474; p_{5,45\text{Hz}} = 0.1415; p_{5,55\text{Hz}} = 0.2425$$

where BHP is the brake horsepower (kW), x is the flow rate in (m³/h), and p_i represents model coefficients.

4.3 Pump Performance Curves for viscous Fluids

This sub-chapters show the viscous performance test in comparison with the water tests and the resulting performance loss.

4.3.1 REDA D2100EZ

The initial plan was to pump the polymer solution at 50°C. However, this plan slightly changed, due to different reasons, like technical issues or polymer degradation caused by oxygen and iron rust. As a result, the viscous pump experiments have been conducted with lower temperatures and their resulting viscosities (see Figure 35). The curves perfectly show the shear-thinning behavior of the polymer mixture. The actual shear rate and the corresponding viscosity, present inside the pump impeller, are complicated to evaluate.

Nonetheless, because of the high rotational speed and turbulence in the pump, a high shear rate viscosity might be the best assumption.

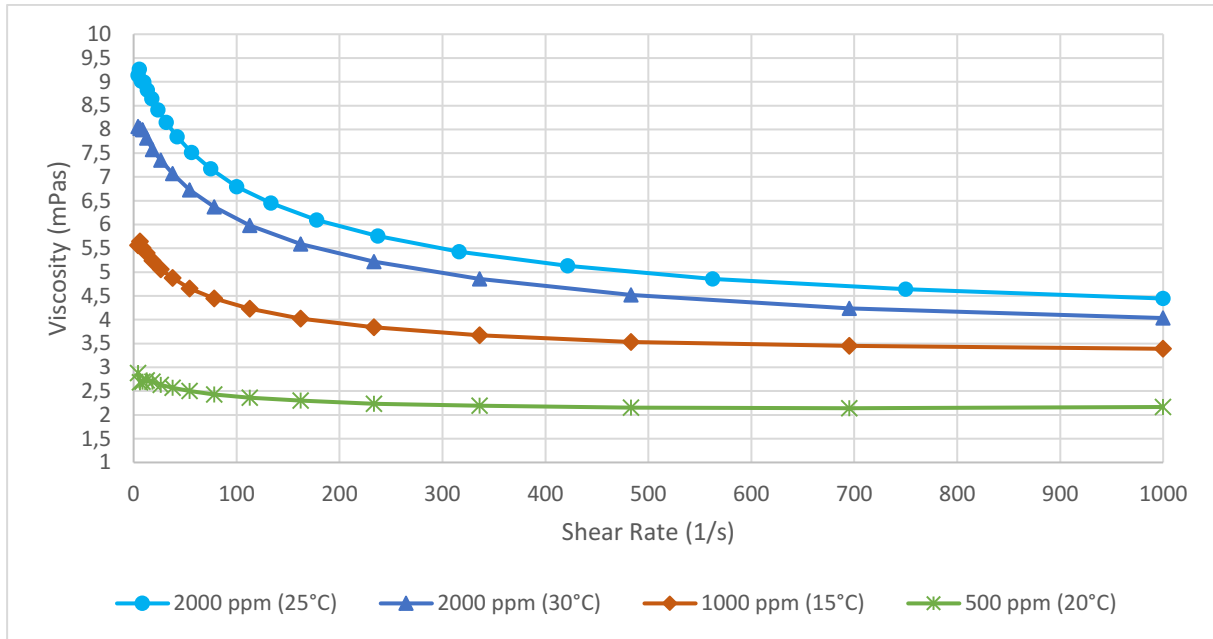


Figure 35: Viscosity profile for each polymer (HPAM) concentration at its test temperature (sample taken from the pressure tank before each test), REDA D2100EZ experiments

The viscous experiments show surprising results for all three tested polymer concentration. Figure 36 shows the 45 Hz water performance versus viscous performance. The 35 and 55 Hz tests have a similar trend and can be found in Appendix C.

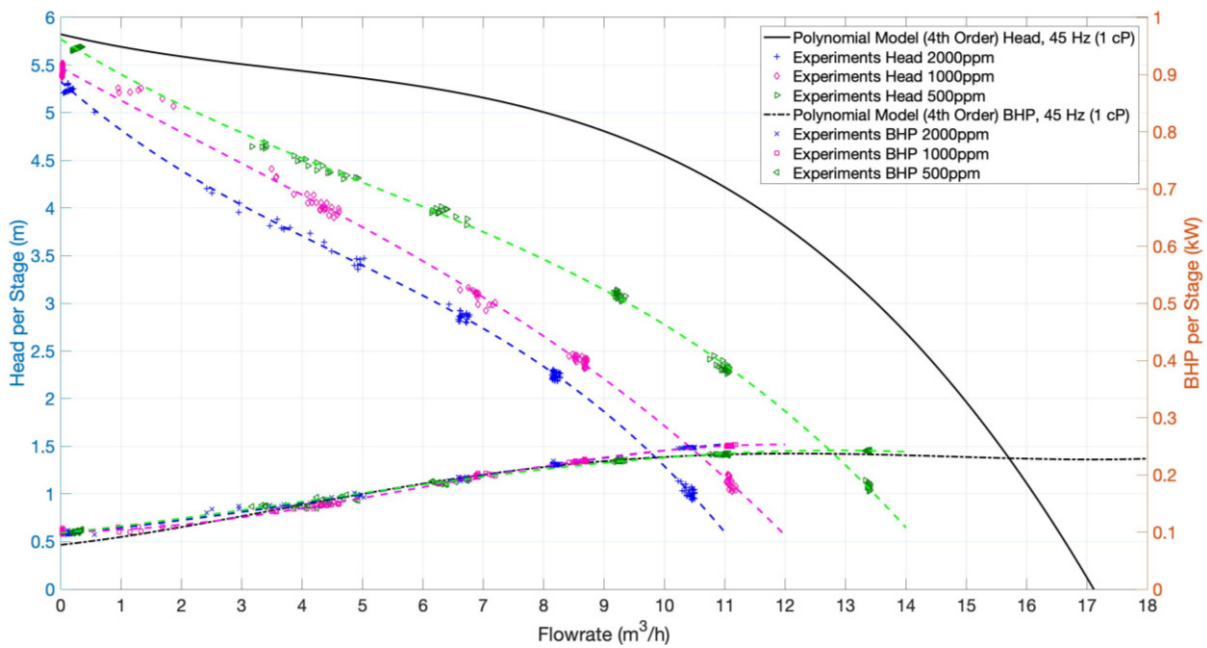


Figure 36: REDA D2100EZ head and brake horsepower curve – 45 Hz polynomial model (water, 1 cP and 1 S.G.) versus polymeric fluid performance (2000 ppm at 30°C)

The head curve shows a significant derating in terms of pressure and flow rate. In contrast, the brake horsepower stays almost the same level, which leads to a substantial decrease in the pump's efficiency.

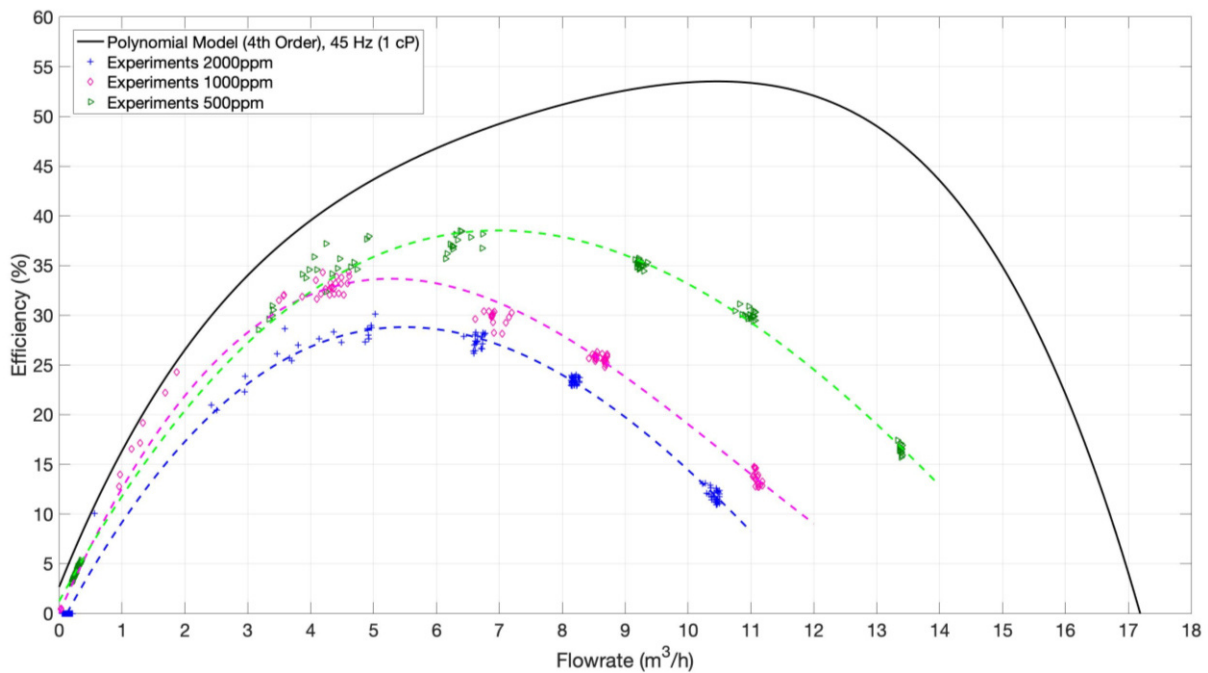


Figure 37: REDA D2100EZ efficiency curve – 45 Hz polynomial model (water, 1 cP and 1 S.G.) versus polymeric fluid performance (2000 ppm at 30°C)

Two main things were done to check the measured data reliability because of the surprising viscous test performance:

1. The test sequence was started with the 2000-ppm solution. After two initial runs with 35 Hz, the shut-in pressure level was lower than expected, and the produced volume was much lower compared to the freshwater tests. In order to prove the proper function of the pump, the polymeric fluid was changed against freshwater. The subsequent experiment with freshwater showed a typical ESP performance, which proved that the poor pump performance, was related to the viscous liquid.
2. Integrating the flowmeter measurement overtime allowed the comparison of the measured volume with the actual volume (produced into the intermediate bulk container). As both volumes matched up, there was the certainty that the flowmeter measurements have been correct, and the pump produced less viscous fluid than water at a certain pressure level.

Table 7 shows the flow rate, the head per stage, the brake horsepower per stage, and the pump efficiency for each fluid at the best efficiency point.

Table 7: REDA D2100EZ, water performance at the respective best efficiency point

Frequency	Q (m ³ /h)	H/Stage (m)	BHP/Stage (kW)	Eff. (%)
35 HZ	8.1	2.67	0.110	53.24
45 Hz	10.5	4.39	0.234	53.52
55 Hz	12.3	6.72	0.419	54.51

Table 8: REDA D2100EZ, 500-ppm performance at the respective best efficiency point

Frequency	Q (m ³ /h)	H/Stage (m)	BHP/Stage (kW)	Eff. (%)
35 HZ	4.3	2.70	0.084	41.84
45 Hz	7.0	3.75	0.197	38.53
55 Hz	9.2	6.05	0.364	43.80

Table 9: REDA D2100EZ, 1000-ppm performance at the respective best efficiency point

Frequency	Q (m ³ /h)	H/Stage (m)	BHP/Stage (kW)	Eff. (%)
35 HZ	3.2	2.53	0.060	33.84
45 Hz	5.3	3.69	0.165	33.66
55 Hz	7.2	5.70	0.317	36.74

Table 10: REDA D2100EZ, 2000-ppm performance at the respective best efficiency point

Frequency	Q (m ³ /h)	H/Stage (m)	BHP/Stage (kW)	Eff. (%)
35 HZ	2.8	2.22	0.0617	25.82
45 Hz	5.5	3.24	0.175	28.80
55 Hz	7.1	5.45	0.313	34.90

Furthermore, during startup, it was not possible to immediately reach the shut-in pump head. Figure 38 shows pump pressure developed with water, 500 ppm HPAM, 1000 ppm HPAM and with 2000 ppm HPAM for 35 and 45 Hz. The pump speed was ramped up with 2 seconds per Hertz, and when the curves start deviating from the ramp, the target frequency was reached. The plots show that in the viscous test, a lower head was developed until it started to increase.

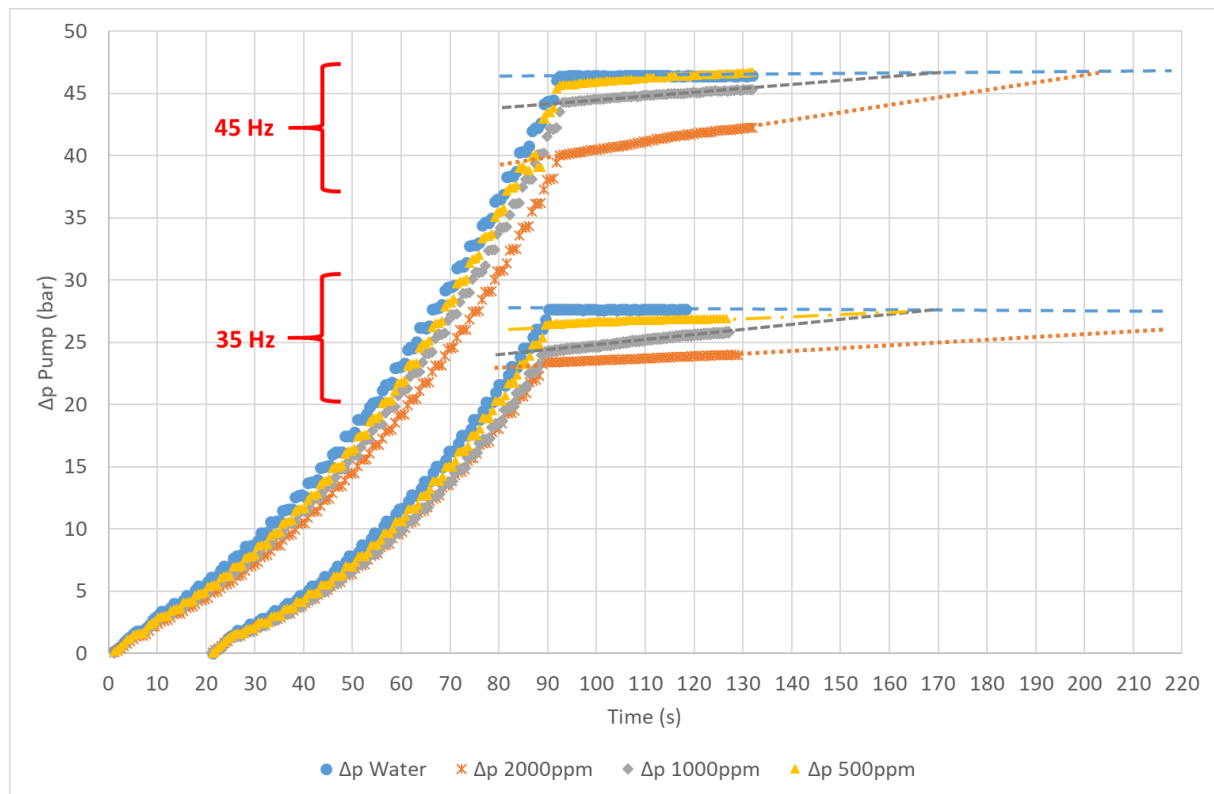


Figure 38: REDA D2100EZ shut-in pressure for water, 500 ppm, 1000 ppm, and 2000-ppm HPAM solution at 35 and 45 Hz

Table 11 summarizes the pressure development slope for each polymer concentration and frequency after the target frequency was reached. There is a general trend that the higher the frequency, the stronger the pressure increase over time for the polymeric fluid. This trend could indicate that the pump shears the liquid inside the pump. Only the 1000 ppm and 35 Hz data slightly deviate from this trend. Furthermore, the 500-ppm curve at 45 Hz even exceeds the water curve, which is also the case for the 500-ppm curve at 55 Hz. It is difficult to say where this behavior comes from but could be related to the fluid characteristics or the measurement itself. Additionally, the liquid temperature of all tests increases between 0.9 and 1.5°C during this shut-in period, which could also be a reason for this pressure increase as the viscosity decrease with increasing temperature.

Table 11: REDA D2100EZ, Pressure development (increase) at shut-in

Frequency	35 Hz	45 Hz	55 Hz
Water	constant	constant	constant
500 ppm	0.15 bar/10s	0.25 bar/10s	0.75 bar/10s
1000 ppm	0.5 bar/10s	0.25 bar/10s	0.71 bar/10s
2000 ppm	0.20 bar/10s	0.55 bar/10s	0.70 bar/10s

Comparing Figure 39 and Figure 40 gives insight into the hydraulic and mechanical power behavior between the water and viscous experiments.

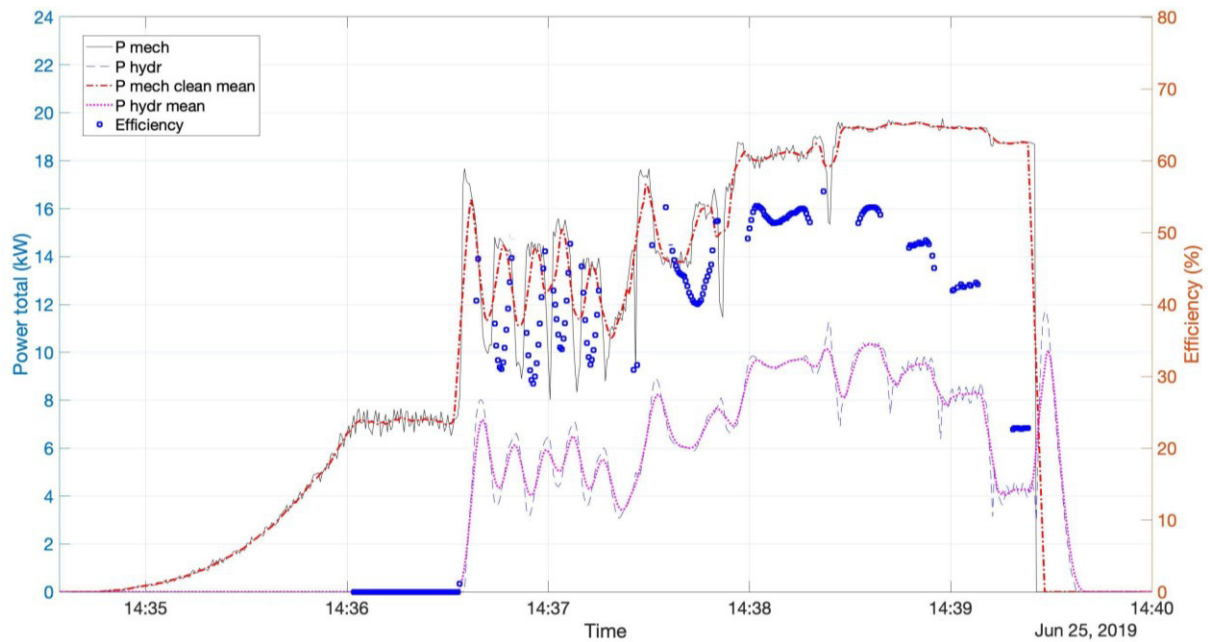


Figure 39: REDA D2100EZ hydraulic and mechanical power (open loop water test with 45 Hz)

For example, the mechanical power in the water test (Figure 39, from 14:38 to 14:39) is only slightly changing for the stabilized flow periods. In contrast, the difference in mechanical power during the viscous experiments (Figure 40, from 12:18 to 12:20) is much more distinctive, which might be again attributed to the polymer fluid rheology. Two possible explanations for this phenomenon are the non-Newtonian polymer fluid behavior, but also the slipperiness of the mixture. It shows that not only hydraulic power is responsible for the efficiency loss, but also the mechanical power contributes its share.

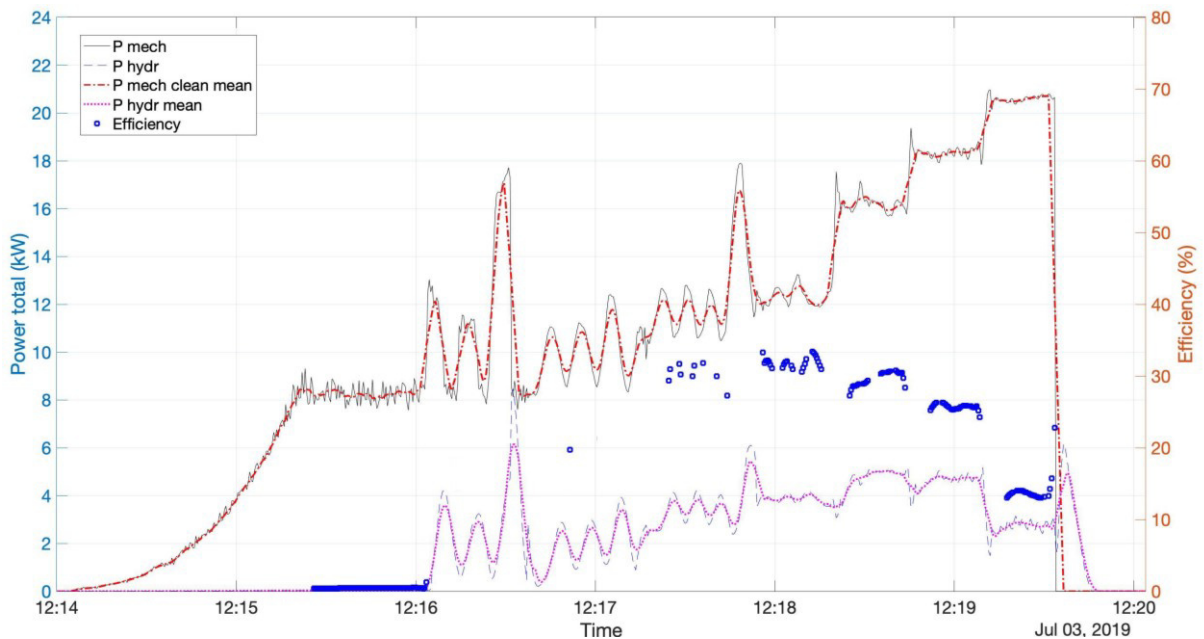


Figure 40: REDA D2100EZ hydraulic and mechanical power (open loop 1000-ppm HPAM with 45 Hz)

Looking at the mechanical power at shut-in conditions in both plots (Figure 39, from 14:35 to 14:36:50 and Figure 40, from 12:14 to 12:16) we can see that the polymer tests show a

higher power consumption than the water experiment. Moreover, the starting torque measurements, shown in Figure 41, are also quite interesting. For the viscous fluid, the starting torque is constantly higher than it is with water.

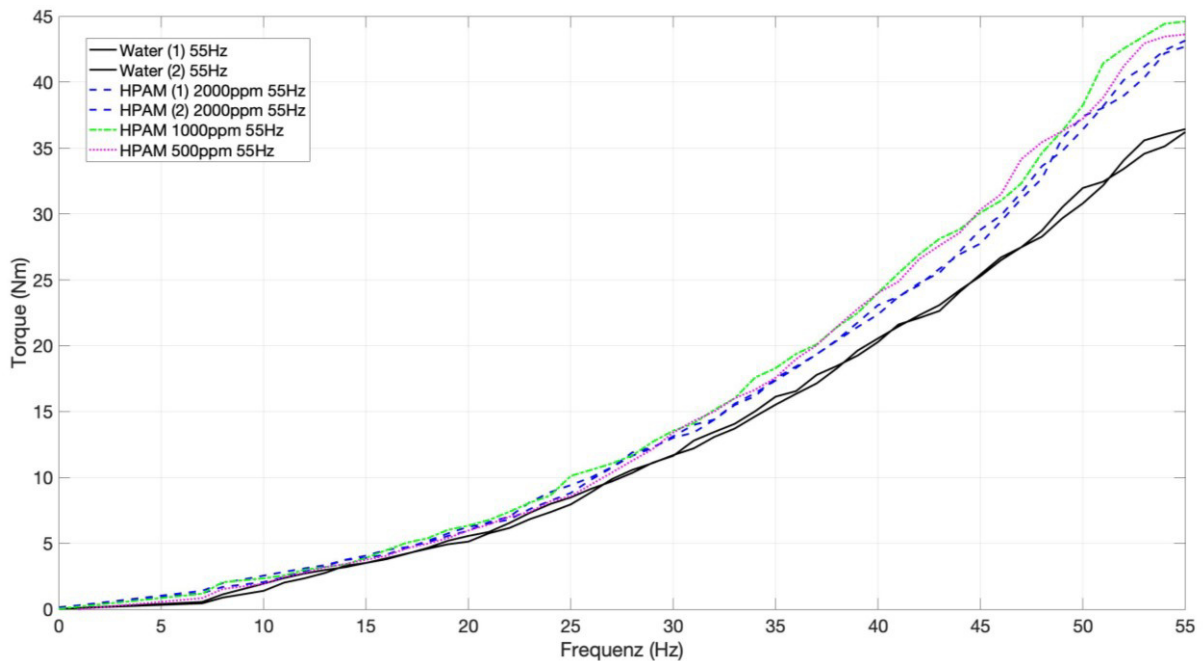


Figure 41: REDA D2100EZ startup torque measurements

All this observation have also been found for the other tested concentrations and rotational speeds.

4.3.2 REDA D2400N

After the 82-stage pump test, about 500 liters of the 500-ppm and 1000-ppm fluid were left over. Therefore, additional tests with the 7-stage pump were conducted with these two concentrations. This time, the casing next to the ESP string was used as the reservoir tank, instead of the 1,500-liter pressure tank. This decision was based on the fact that iron rust inside the 1,500-liter tank led to polymer degradation. Notably, the combination of oxygen and iron is unfavorable for polymer stability. Hence, using the stainless steel casing, it was possible to avoid the iron component. The major disadvantage of this setup was that the casing had only 200 liters of volume, which decreased the number of test points per run. Figure 42 shows the viscosity versus shear rate plot for the mixture at the test temperature. Although the fluid was stored since the 82-stage experiments (for 20 days at 16°C), the polymer solutions in the intermediate bulk containers remained stable.

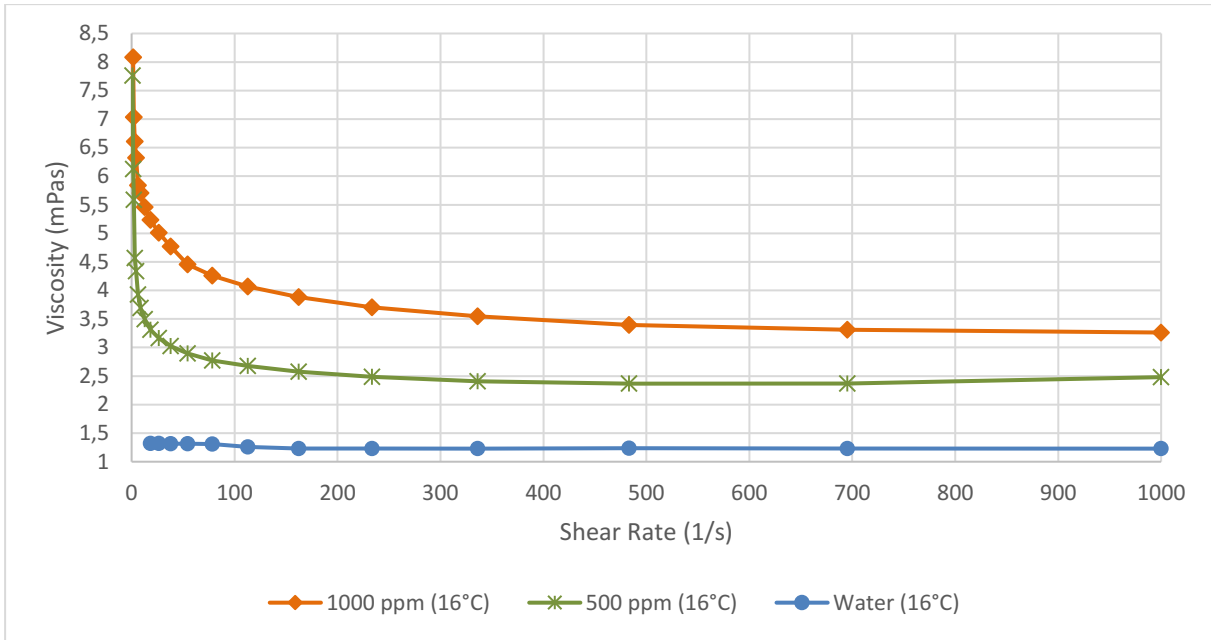


Figure 42: Viscosity profile for each polymer (HPAM) concentration at its test temperature (sample from the 200-liter casing before each test), REDA D2400N experiments

For this experimental sequence, only 45 Hz rotational speed has been tested due to the limited amount of viscous liquid. The head performance and brake horsepower of the polymeric fluid tests at 45 Hz is shown in Figure 43. The measurements exhibit a significant head curve derating, while the brake horsepower remained at the level of the pump test with water. This observation is similar to the 82-stage experiments and confirms that the performance losses are related to the non-Newtonian fluid itself.

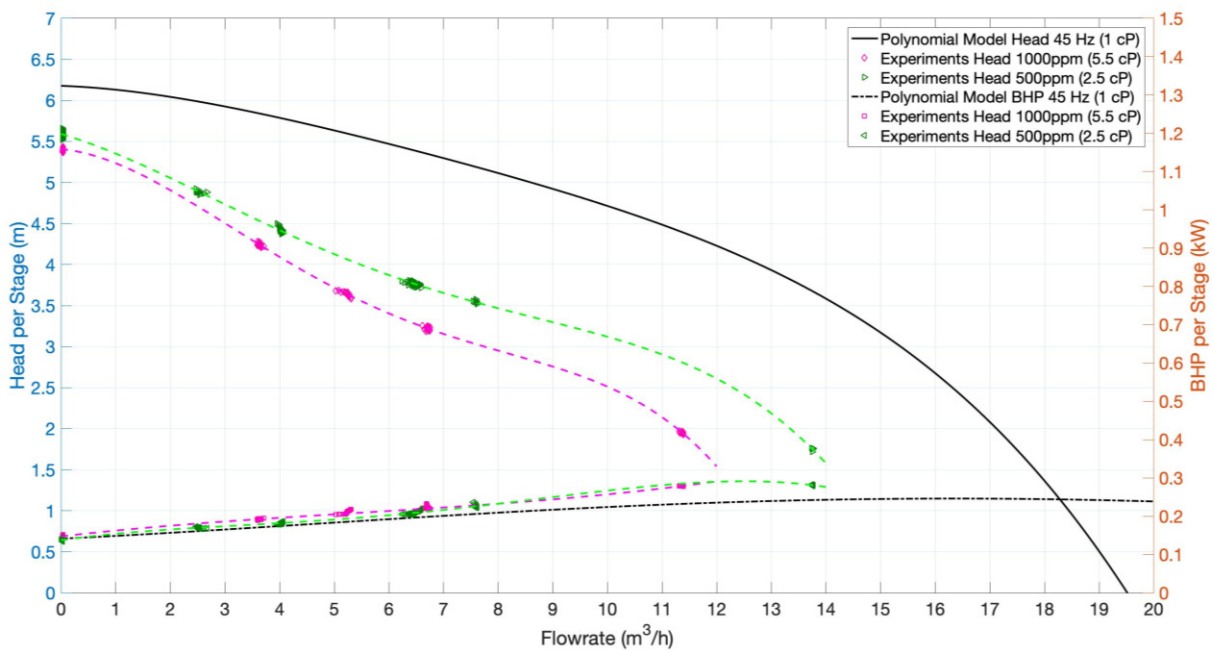


Figure 43: REDA D2400N head and brake horsepower curve – 45 Hz polynomial model (water, 1 cP and 1 S.G.) versus polymeric fluid performance

The following tables provide the flow rate, the head per stage, the brake horsepower per stage, and the pump efficiency for each fluid at the best efficiency point.

Table 12: REDA D2400N, water performance at the respective best efficiency point

Frequency	Fluid	Q (m ³ /h)	H/Stage (m)	BHP/Stage (kW)	Eff. (%)
45 Hz	Freshwater	11.8	4.28	0.235	58.84
45 Hz	1000 ppm	6.7	3.23	0.220	26.70
45 Hz	500 ppm	7.4	3.58	0.223	32.82

4.4 Dynamic Viscosity Measurements

The viscosity at the beginning of the test was lower than expected. This viscosity loss was related to temperature, oxygen, and iron-induced polymer degradation. Further information about the mixture preparation and its transport can be read in Appendix E. Table 13 shows the viscosity measurements conducted with a Brookfield viscometer on the 2 July 2019 and 3 July 2019. The measurements were done immediately after the sampling procedure on site. The company's standard analyses are performed at 30°C with 6 rpm rotational speed using a Brookfield Spindle LV#62. The measurements reveal that the largest viscosity loss occurred during transportation of the fluid as well as when the liquid was filled into the pressure tank. In fact, the higher the concentration was, the higher was this loss. Chapter 5.3 discusses the potential causes of this observation.

Table 13: Viscosity measurements during REDA D2100EZ pump tests, Brookfield at 30°C and 6 rpm

Sampling/Measurement Point and Date	500 ppm (03.07.2019)	1000 ppm (03.07.2019)	2000 ppm (02.07.2019)
IBC Tank – Gänsendorf (26.06.2019)	2.5 cP	5.5 cP	16.0 cP
IBC Tank – Leoben	2.2 cP	4.0 cP	11.0 cP
Pressure Tank (before tests)	2.1 cP	3.9 cP	8.2 cP
35 Hz (at Q _{BEP})	1.9 cP	3.0 cP	8.0 cP
45 Hz (at Q _{BEP})	1.6 cP	3.0 cP	7.0 cP
Pressure Tank (between tests)	1.6 cP	No data	7.5 cP
55 Hz (at Q _{BEP})	1.5 cP	2.6 cP	6.5 cP
Pressure Tank (after tests)	No data	3.5 cP	7 cP

On the 4 July 2019 and 5 July 2019, the same samples were measured a second time at the PCCL (Polymer Competence Center Leoben GmbH). An Anton Paar rheometer with a double gap measuring system was used (see Appendix D). This time, the measurements were performed with the respective test temperature described in the experimental matrix and at different shear rates. In addition, all samples were measured with the initially planned

50°C, in order to have an idea about the fluid viscosity at the reservoir temperature (see Appendix D). The Anton Paar rheometer measurements show the same trend as the Brookfield data (e.g., see Figure 44)

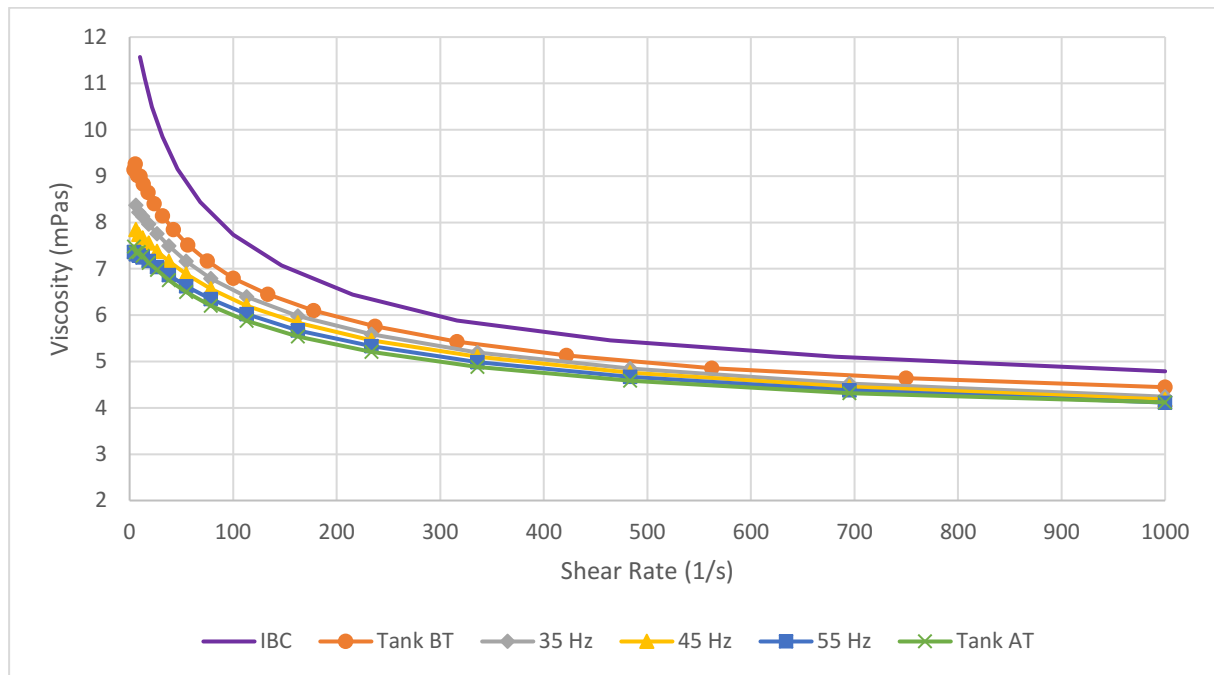


Figure 44: Viscosity profile of the 2000-ppm fluid samples at 25°C (REDA D2100EZ tests)

As mentioned before, due to the oxygen and iron-induced degradation, in the 7-stage experiments, the stainless steel casing was used as a fluid reservoir. In this case, only oxygen during decanting from the IBC may have influenced the polymeric fluid viscosity. Figure 45 shows that the samples taken at 45 Hz (BEP) during the pumping operation show only a minor degradation at low shear rates. At high shear rates, the viscosity is almost identical with the pre-test viscosity.

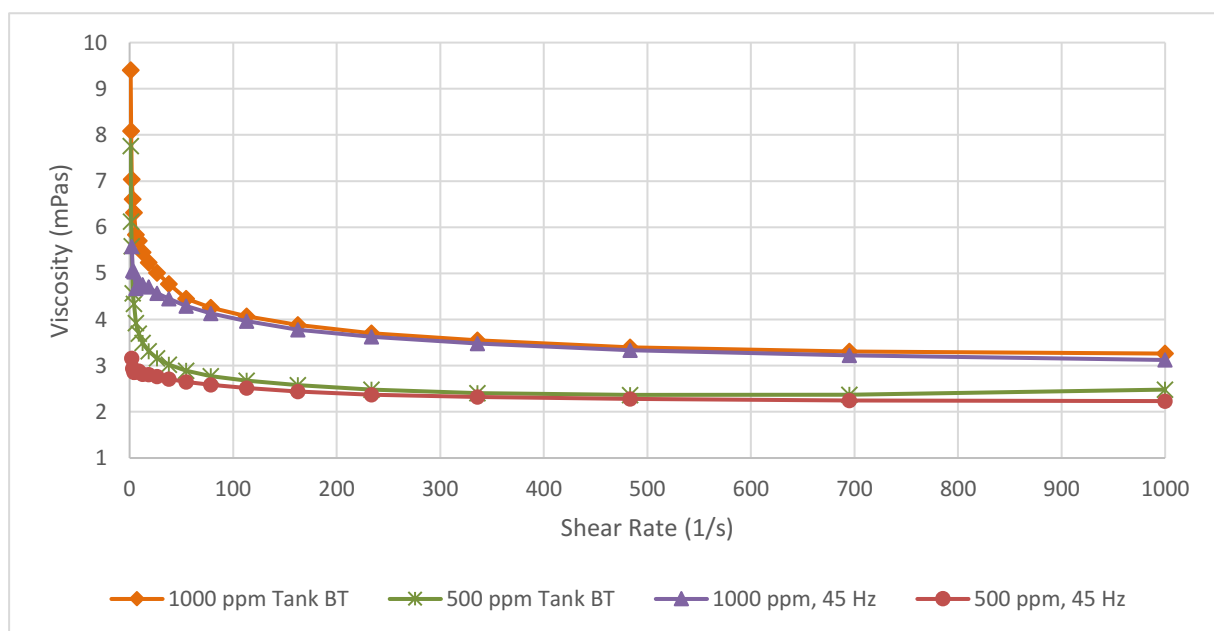


Figure 45: Viscosity profile of the 1000-ppm and 500-ppm fluid samples at 16°C (REDA D2400N tests)

4.5 Investigation of Stage Degradation

The last testing sequence included the investigation of the pressure development within each stage of the 7-stage REDA D2400N pump. The ESP was disassembled in order to connect a pressure sensor to every single stage. The pressure sensing holes were drilled into the upper diffuser section, just before the fluid enters the next impeller.



Figure 46: a) Diffusers with pressure sensing, b) Pressure sensor screwed into the pump casing, c) Pressure sensors connected to each stage of the REDA D2400N pump

First, after reassembling the pump, it was tested with water again. The data showed that the pump still produces the same performance curves as it did before disassembling it (see Appendix C, Figure 92). Therefore, it can be said that the attached sensors do not cause any losses or other inferences. Following the validation tests with water, the pump was tested with a new batch of 1000-ppm HPAM-brine mixture. Two IBCs, each containing 1000 liter, were delivered for these experiments. IBC 1 contained 1000-ppm mixture with a viscosity of 7.5 cP at 6 rpm at 30°C (Brookfield viscometer). IBC 2 contained 1000-ppm mixture with a viscosity of 5.8 cP at 6 rpm at 30°C (Brookfield viscometer). Figure 47 shows the initial pump performance and the pump performance obtained with the reassembled pump (Experiments Head/BHP reassembled 1000 ppm).

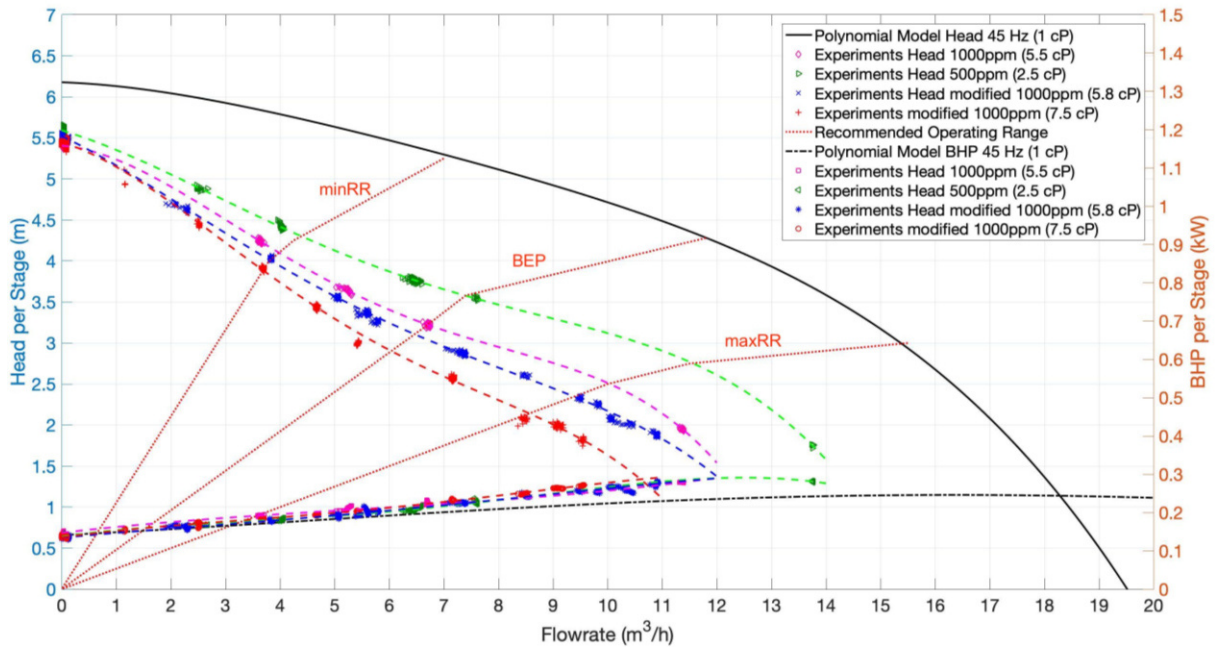


Figure 47: Reassembled REDA D2400N head and brake horsepower curve – 45 Hz polynomial model (water, 1 cP and 1 S.G.) versus polymeric fluid performance

The data show the anticipated viscous performance. Both viscous tests conducted with the reassembled ESP and the new polymer mixtures (5.8/7.5 cP at 6 rpm and 30°C) are below the old 1000-ppm (5.5 cP at 6 rpm and 30°C) performance. It also shows how well the pump performances behave with different fluid viscosities. The efficiency curves (see Appendix C, Figure 94) show that the highest efficiency range is between a rate of 4 m³/h and 9 m³/h for the polymeric liquids. With the connection of pressure sensors to each stage, it was possible to investigate the head development within each stage over a wide flow rate range.

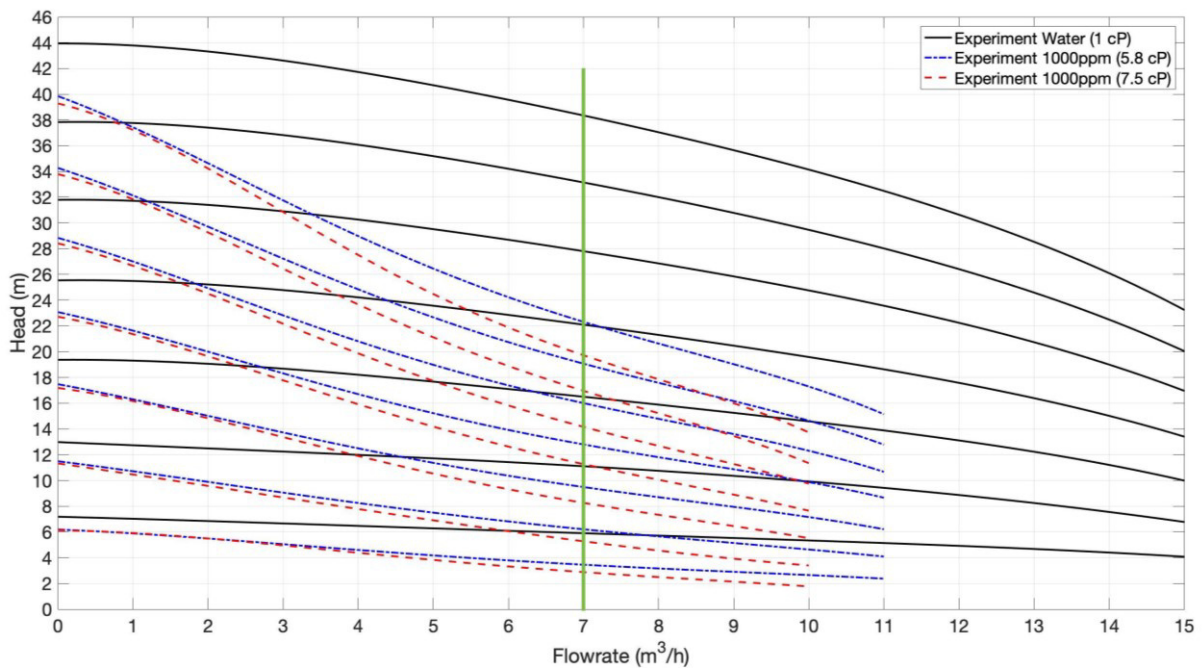


Figure 48: Reassembled REDA D2400N head curve for each stage – 45 Hz polynomial model fit

It can be seen that the head losses start already at stage one and continuously increases up to stage seven. It is interesting that for both viscous performances there is almost no head difference at the shut-in head and low flowrates throughout all stages. However, for flowrates exceeding $2 \text{ m}^3/\text{h}$, the head curve of the 7.5 cP fluid starts deviating from the 5.5 cP head curve. In fact, the higher the flowrate gets, the higher is the head loss, which is adding up over the stages. The following plots may help to understand the observed behavior and gives reasons for it.

For example, in Figure 49, the total pump head development for water and the two polymer-laden fluids is plotted for all seven stages. The rotational speed is 45 Hz at a constant flow rate of $7 \text{ m}^3/\text{h}$.

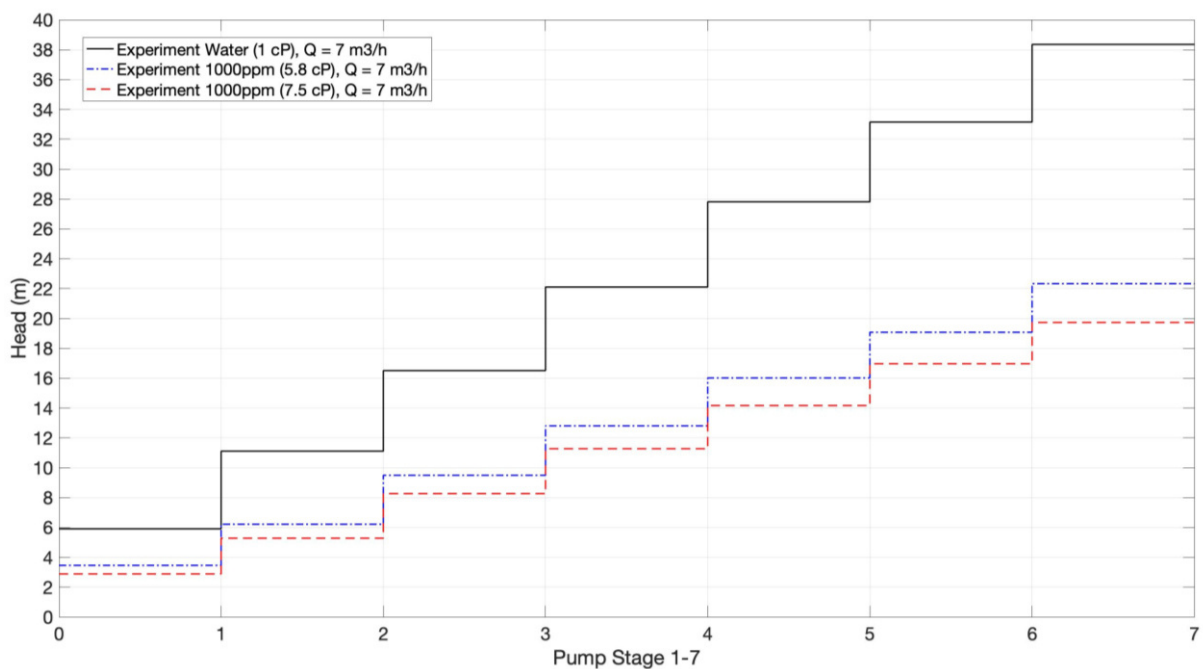


Figure 49: Reassembled REDA D2400N head development from stage 1 to 7 at 45 Hz speed and $7 \text{ m}^3/\text{h}$ flowrate

From stage one to stage seven, the viscous performances increasingly deviate from the water head. In theory, the first assumption would be that the unshereed polymeric fluid entering the pump cause the highest performance degradation at the first stages. Then the polymer would get more sheared stage after stage, causing the actual head performance to increase at stages towards the discharge. Nevertheless, having a look at Figure 50, this assumption cannot be fully confirmed or at least causes only a minor effect. The data show that the pump head produced by each stage is relatively constant for all fluids at a rate of $7 \text{ m}^3/\text{h}$. The head variations of approximately 0.5 m from stage to stage are only about 0.05 bar . Hence, this small increases or decreases could also be a result of the polynomial curve fitting. The head differences in stage one and two a probably caused by the intake pressure and its influence on the pressure reading.

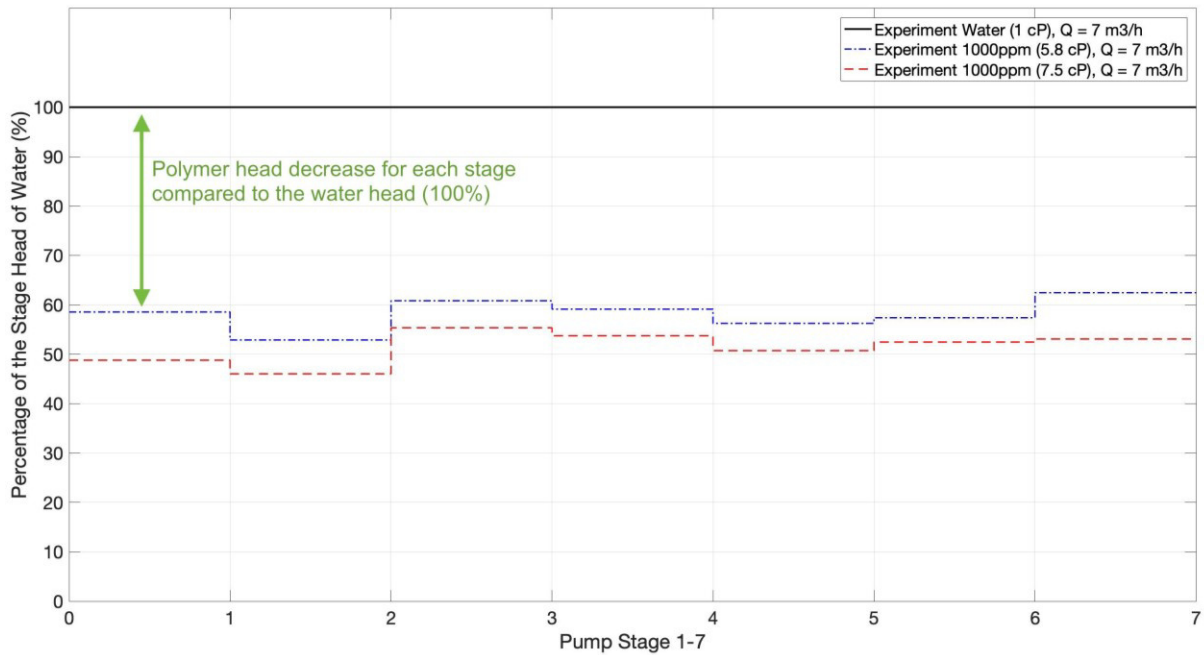


Figure 50: Reassembled REDA D2400N, head difference from stage 1 to 7 at 45 Hz speed and 7 m³/h flowrate

The same result can be observed for other flow rates. There is also no distinctive sign that the viscous pump performance increases along the stages because of polymer shearing. The head produced by each stage remains quite constant for both flowrates.

In addition, the pressure readings during startup suggest that the pressure losses are a function of the number of stages. Each stage contributes a partial performance loss, which adds up over all stages. Furthermore, the data show that for the first two stages, the viscous pressure reading is horizontal like the 1cP-water curve. However, for the upper stages, the viscous pressure reading starts increasing with time. Due to the fact the pump operated against a closed valve, one explanation could be that the viscous fluid is sheared or is compressed in the upper stages.

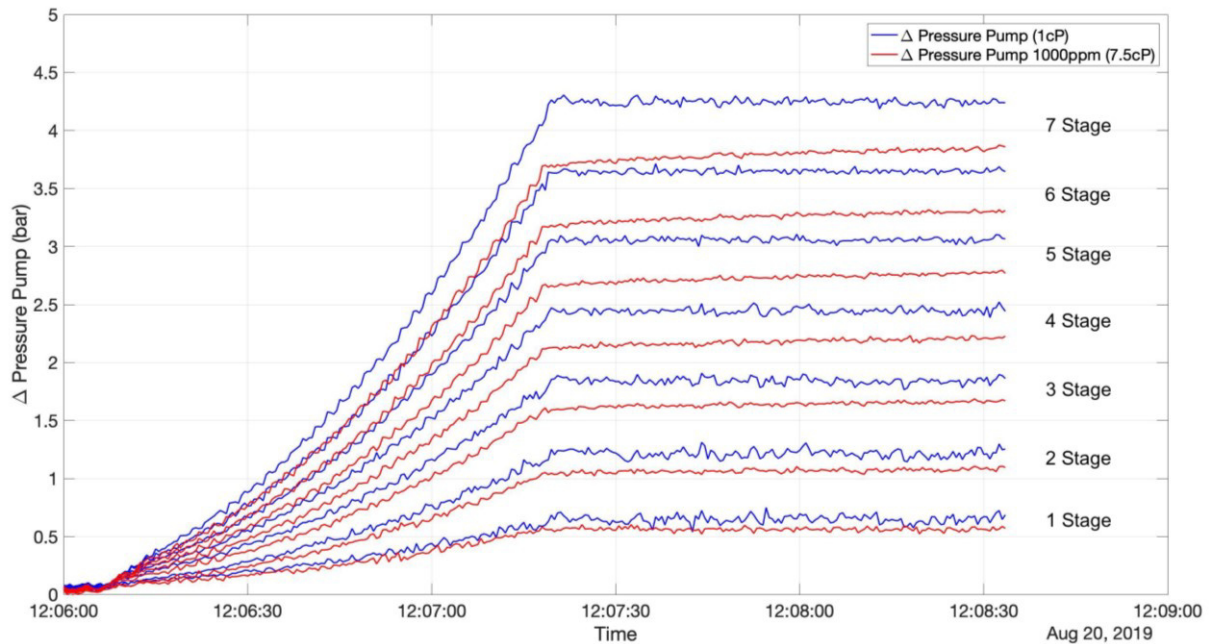


Figure 51: Reassembled REDA D2400N, pressure development from stage 1 to 7 during startup (ramp: 2 s/Hz, final speed: 45 Hz)

4.6 Polymer Loop Circulation

The previous tests showed that the polymer-laden fluid is little to not sheared during the pumping operation within the recommended operating range. Therefore, the decision was to pump the non-Newtonian fluid in a loop for 45 minutes. The pump speed was 45 Hz, the intake pressure 5 bar and a constant choke opening about 65% was set. This resulted in an average flow rate of 5.2 m³/h, which is in the BEP-region of the underlying fluid performance curve. At this flow rate, the fluid volume in the pressure tank was pumped approximately four times in a circle.

It can be observed that over the testing period, the pump's pressure difference steadily increased while also the flowrate slowly increased (see Figure 52). This could be a sign of continuous polymer shearing either by the ESP, by the choke or both. However, it is not clear if only shear forces caused the polymer degradation. There is also the possibility that iron or oxygen inside the tank had a degradation effect and caused the observed behavior. Additionally, the parallel flowrate shift at 19:22 is not fully understood, but the flowrate increase continued after the jump as it did before.

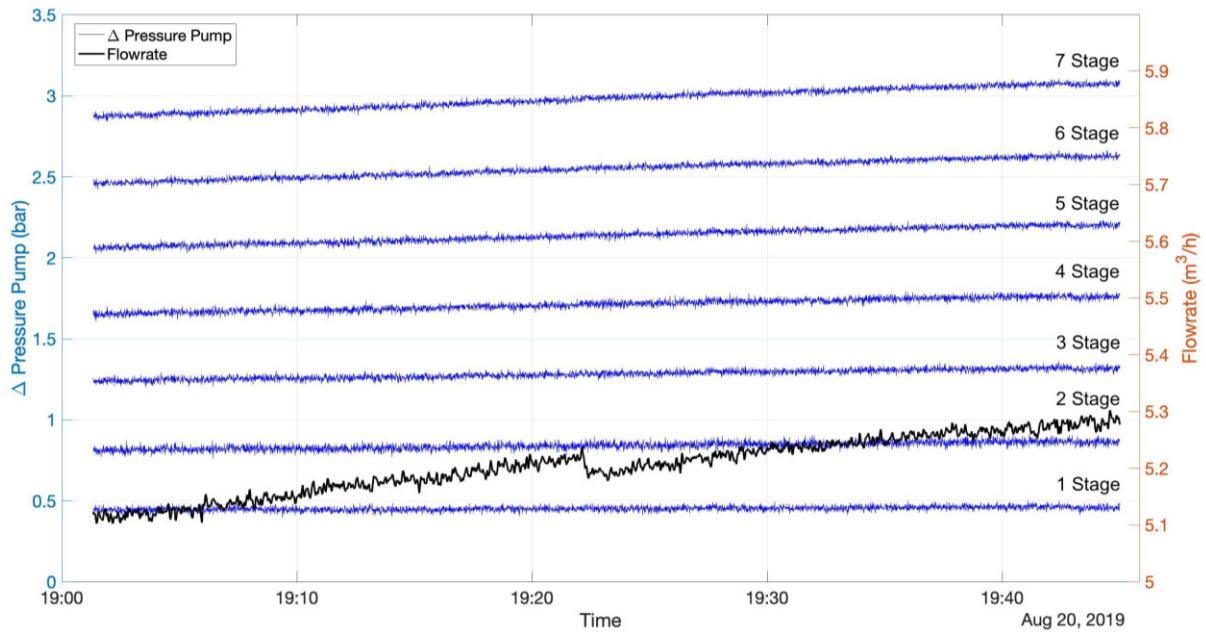


Figure 52: Reassembled REDA D2400N single-stage pressure (discharge minus intake) versus flowrate during loop pumping of a 1000-ppm HPAM solution

Table 14 shows the pressure increase in the stages. In this case, the stage pressure minus the intake pressure was calculated for all stages. Therefore, Δp at the first stages (1 Stage) is the pressure measured at stage one minus the intake pressure. The pressure Δp at the second stage (2 Stage) is the pressure measured at stage two minus the intake pressure and so on.

Table 14: REDA D2400N stage pressure increase over time (loop pumping)

	Start (19:01) $\Delta p_{\text{stage-intake}}$ (bar)	End (19:45) $\Delta p_{\text{stage-intake}}$ (bar)	Increase from Start to End (%)
1 Stage	0.45	0.46	2.2
2 Stage	0.81	0.88	7.3
3 Stage	1.24	1.32	6.5
4 Stage	1.66	1.77	6.6
5 Stage	2.06	2.20	6.8
6 Stage	2.46	2.63	7.0
7 Stage	2.87	3.08	7.3

From Table 14 can be seen that for each stage an increase of around 7% occurs over the period. Only the first stage has a lower increase, which could be caused by intake effects. In addition, the difference between the differential pressures from stage to stage is between 0.4 bar and 0.45 bar. This again would confirm that the shear and fluid effects act equally on all stages. Otherwise, we would see a different differential pressure between the first and

second stage compared to the differential pressure between the sixth and seventh stage. The flow flowrate increases from 5.11 m³/h (19:01) to 5.21 m³/h (19:21), which is about 2% per 20 minutes. After the drop, it rises again from 5.18 m³/h (19:23) to 5.28 m³/h (19:45), which is again about 2% per 20 minutes. This is a quite low increase and like explained before, it is difficult to say if only shearing or also chemical degradation is the cause.

Plotting the data in a head curve diagram, it shows an apparent performance enhancement towards the water performance curve, as shown in Figure 53.

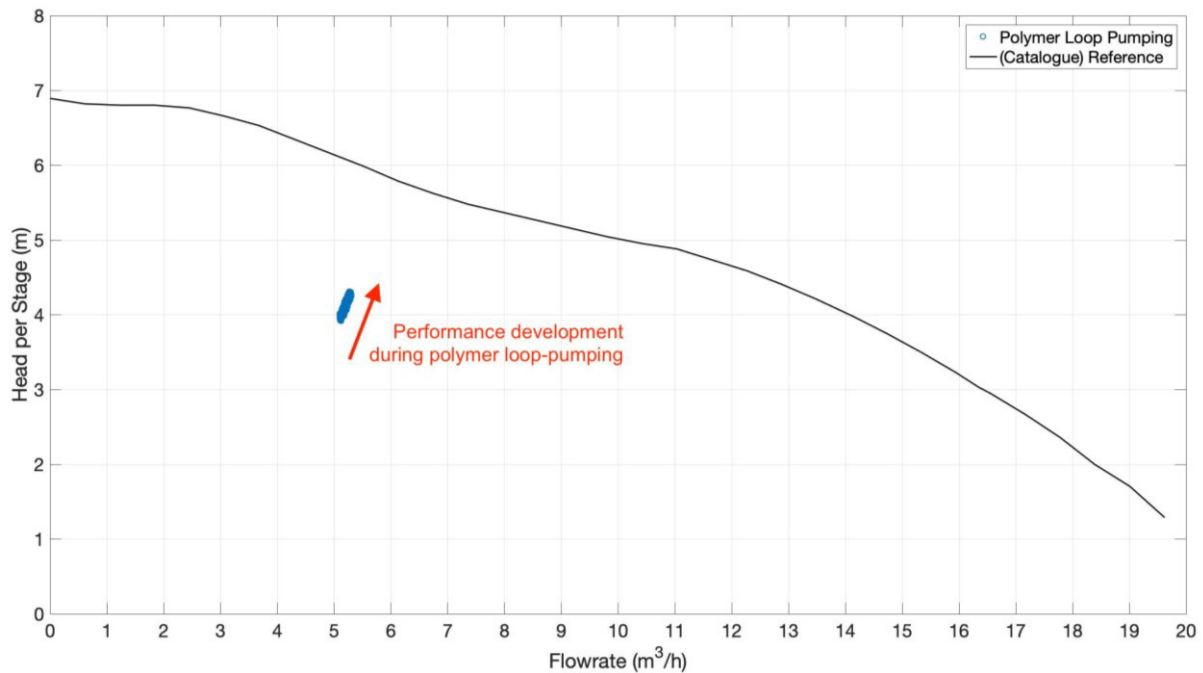


Figure 53: Reassembled REDA D2400N head curve development at a constant choke opening during loop pumping of a 1000-ppm HPAM solution

The mechanical power stayed at a consistent level over the testing period. Only the hydraulic power increased steadily, caused by the pressure and flowrate gain. This means that during the loop pumping the efficiency increased continuously.

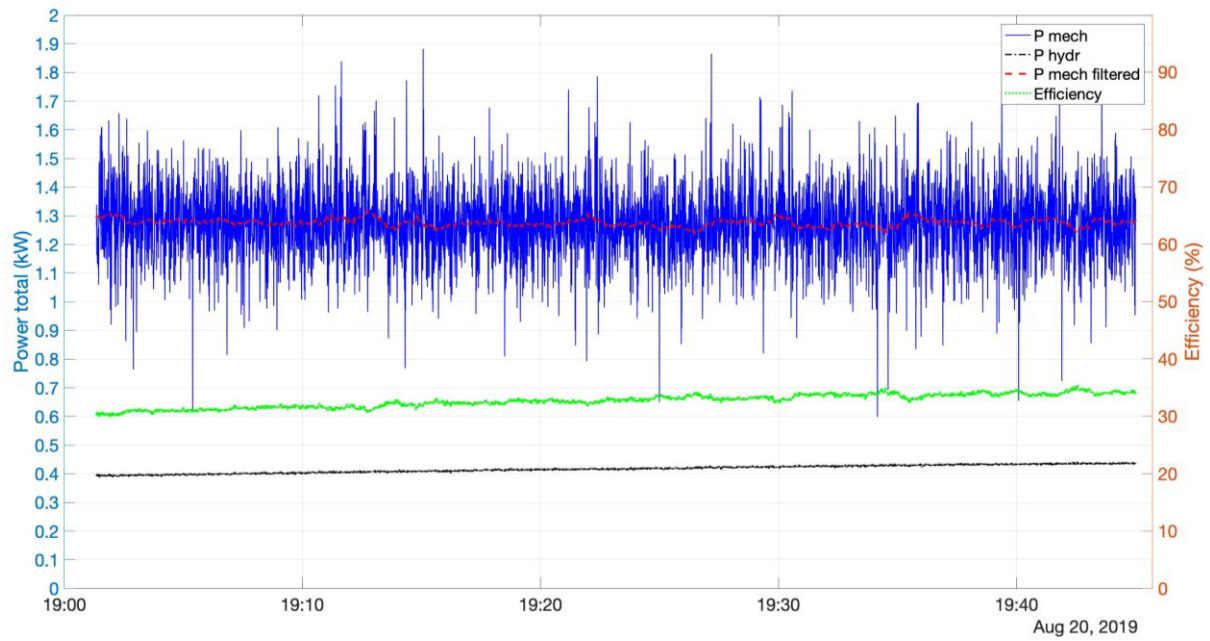


Figure 54: Reassembled REDA D2400N total hydraulic power and total mechanical power during loop pumping of a 1000-ppm HPAM solution

5 Evaluation

In this chapter, the experimental results are discussed in detail.

5.1 Intake Pressure Analysis

The tests performed with three rotational speeds and three intake pressures show that there is no difference using 5, 10 or 15 bar inlet pressure. Indeed, this observation suggests that the minimum required intake pressure might be even below five bars. Nonetheless, all experiments were conducted with five bar intake pressure.

5.2 Derating Factors for polymer-laden Fluids

The performance loss when pumping a non-Newtonian, polymer-laden fluid is much higher than expected. The results show a considerable flow rate and pump head drop, resulting in a tremendous efficiency decrease (see Table 15). The efficiency loss has a magnitude of up to 50%, compared to pumping freshwater. The efficiency change in percentage was calculated by using Eq. 60:

$$\% - \text{Change} = \frac{Data_{visc} - Data_{water}}{Data_{water}} \times 100 \quad (\text{Eq. 60})$$

where %-Change is the relative efficiency change in (%), $Data_{visc}$ is the viscous measurement at the respective BEP, and $Data_{water}$ is the water measurement at the respective BEP.

Table 15: REDA D2100EZ efficiency loss of the viscous tests compared to the water tests at the respective best efficiency point

Frequency	Water (absolute value, $Data_{water}$)	500 ppm (%-Change)	1000 ppm (%-Change)	2000 ppm (%-Change)
35 HZ	53.2%	-21.4%	-37.3%	-51.5%
45 Hz	53.5%	-28.0%	-37.1%	-46.2%
55 Hz	54.5%	-19.6%	-32.6%	-36.0%

Like the 82-stage ESP, the 7-stage pump showed a substantial decrease in efficiency, shown in Table 16. The 7-stage head curve derating is slightly higher than the 82-stage pump derating. This observation suggests that that the 82-stage ESP exerts more turbulence on the fluid, obtaining a more water-like fluid behavior. Nevertheless, the number of stages seems not to have a significant impact on the polymeric fluid performance.

Table 16: REDA D2400N efficiency loss of the viscous tests compared to the water tests at the best efficiency point

Frequency	Water (absolute value, $Data_{water}$)	500 ppm (%-Change)	1000 ppm (%-Change)
45 Hz	58.8%	-44.2%	-54.6%

In order to produce the same rate with the viscous fluid, as with freshwater would mean to run the pump at a higher frequency. However, increasing the rotational speed would result in much higher energy consumption. Besides, not only the energy consumption, which means also higher energy costs, would be affected. The service lifetime of the pump would also be drastically reduced by the changing rotational speed, e.g., due to more vibrations. An article published by Demin et al. (2004) supports the obtained result. He states that after a polymer flood in the Daqing field, the energy efficiency of their ESPs decreased over 50% during back-production of the polymer (550 mg/L PAM) solution. Besides that, the highly viscous fluid reduced the service lifetime of their pumps by one-half (Demin et al. 2004). Considering all these facts, we are profoundly convinced that the non-Newtonian, polymer-laden fluid was responsible for the performance results.

Another interesting finding was the observed starting torque under a 1 Hertz per 2-second ramp. Table 17 exhibits the rise in starting torque between the water and viscous case, calculated by using Eq. 60. The measurements show that the higher the rotational speed, the higher the torque increase. As a result, Starting up an ESP that contains a polymer-laden fluid with a too steep ramp could result in a shaft break. Therefore, a flatter ramp would be recommendable for such situations.

Table 17: Start torque increase when pumping polymer-laden fluids compared to water (REDA D2100EZ tests)

Frequency	500 ppm	1000 ppm	2000 ppm
35 HZ	+11.4%	+15.8%	+10.8%
45 Hz	+19.4%	+18.5%	+11.4%
55 Hz	+ 22.1%	+22.9%	+18.0%

5.3 Input versus Output Viscosities

The shear forces exerted by the ESP on the polymer molecular chains were expected to be highly damaging. This would have meant that the relatively viscous fluid going into the pump would be totally destroyed due to shearing-off of the molecular chains. However, the results revealed a different picture. Indeed, the fluid leaving the pump still has the basic viscosity characteristics of a polymeric liquid. Furthermore, the measurements are inconclusive if

chemical or mechanical degradation was the dominating factor for the minor solution's viscosity alteration. How can that be explained?

The polymer solution's stability was part of many discussions before, during, and after the pump tests. Thomas (2016) states that an oxygen level below 5 ppb is required for excellent stability (Thomas et al. 2012). However, there was oxygen contact during mixing, decanting, and transportation of the polymeric fluid. Additionally, high transporting temperature and iron rust inside the pressure tank in the test facility enhanced the degradation process. Another important fact is that the used HPAM was a high molecular weight polymer with 20 million Daltons, which more instable than a low MW polymer (Thomas et al. 2012). These four factors (oxygen, iron, temperature, high molecular weight) allow giving a potential answer to the observations. Figure 55 shows some of these effects on the polymer mixture's viscosity.

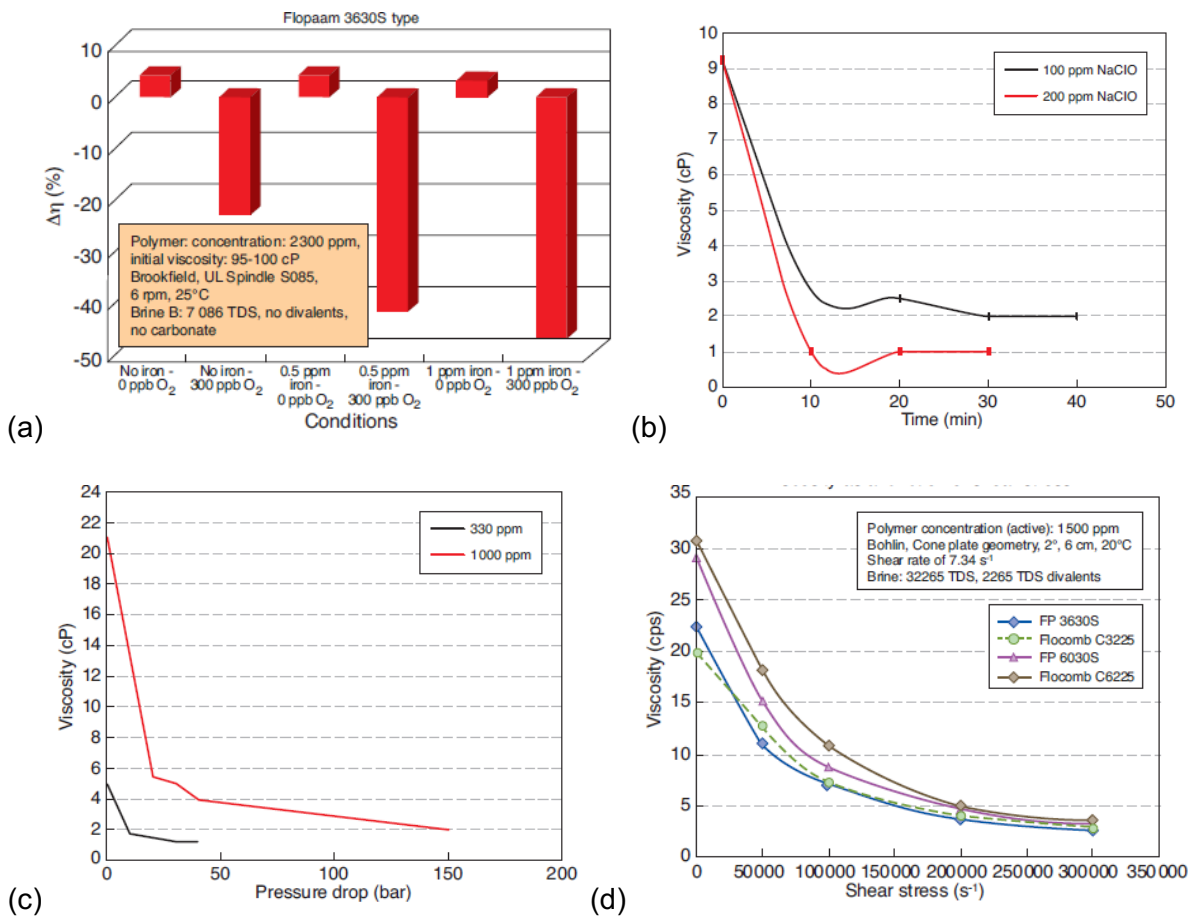


Figure 55: (a) Iron and oxygen-induced polymer viscosity loss over time, (b) chemical degradation of a 10 million g/mole polymer, (c) shear degradation of a 20 million g/mole polymer, (d) polymer solution viscosity versus shear stress¹

¹ Thomas, A., N. Gaillard, and C. Favero. 2012. Some Key Features to Consider When Studying Acrylamide-Based Polymers for Chemical Enhanced Oil Recovery. *Oil & Gas Science and Technology – Revue d'IFP Energies nouvelles* 67(6):887–902.

Thomas (2012) describes in his work that the polymer solution's viscosity shows a steep viscosity drop under chemical and mechanical degradation. However, at some degradation level, the viscosity bottoms out and remains relatively constant in an equilibrium state, as shown in the figures above. It could be that the tested polymer mixtures have reached this converging region before the pump experiments. Therefore, further degradation is relatively little. This phenomenon would explain why the mechanical shearing inside the electric submersible pump had only a minor degradation effect. Nonetheless, the test results are not conclusive if the measured degradation during the pump tests was mainly caused by chemical (iron and oxygen) or mechanical (shear forces) degradation. It seems to be a combination of both.

5.4 Experiments versus Empirical Correlations

Two empirical correlations were chosen to compare them with the experimental results. The first one is the most commonly used correlation, the Hydraulic Institute Method. The second one is the so-called "Morrison's Modified Affinity Law", a relatively new approach which was published the first time in 2017. The detailed theory behind both methods can be found in Chapter 2.5. In order to check the correct setup of the correlation calculations, data published by Le Fur (2015), Patil (2019), and Amaral (2009) were used to backtest the methods.

Le Fur (2015) uses a standard two-stage centrifugal pump (API 610 vertically Suspended (VS1)) for the experiment. The rotational speeds were 1,783 and 1,490 rpm. The tested fluids were water and an ISO VG1000 oil under different temperatures obtaining 486 cP, 1081 cP, and 1639 cP. The author states a clear under-prediction of power and head, as well as an over-predicted flow. The study found a predicted (Hydraulic Institute Method) flow rate deviation between 4 and 16%, a head deviation between 10 and 16% and an efficiency deviation between 13 and 15% from the measured data at the BEP (Le Fur et al. 2015). Amaral (2009) tested a three-stage, semi-axial pump (GN-7000/540™ Model) at 3,500 rpm using 1-cp water and glycerin with 67 to 1,020 cP by variation of the temperature. His study states a predicted (Hydraulic Institute Method) flow rate deviation between 9 and 28%, a head deviation up to 5% and an efficiency deviation between 5.5 and 35% from the measured data at the BEP (Amaral et al. 2009). Patil (2019) used also data from Le Fur (2015) to check the performance of the "Modified Affinity Law" method. He states that the Modified Affinity Law predictions agree with the experimental data from Le Fur (Patil and Morrison 2019).

The studies above used relatively high viscous, Newtonian fluid. In contrast, this study had a relatively low viscous, non-Newtonian liquid under investigation. The main tuning parameter for the correlations is the viscosity. Figure 56 shows the results of the two prediction methods compared with the three concentration performances at 45 Hz. The data exhibits that even if the highest viscosity measurement of all tested polymer solutions (about 11 cP) would be used; the predictions are way off for any experiment.

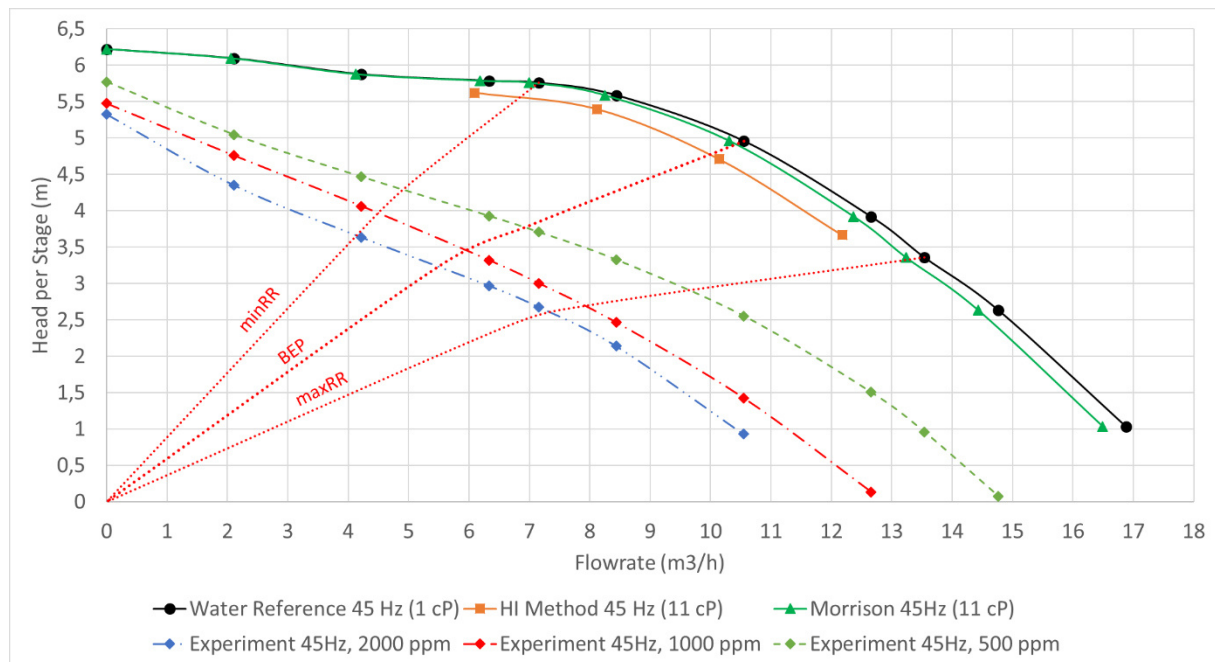


Figure 56: REDA D2100EZ experiments compared with HI and Morrison correlation using real viscosity

Comparing, for example, the Hydraulic Institute prediction with the viscous performances at 45 Hz, the following deviations can be calculated. The head deviates 10% for 500 ppm and 22% for 2000 ppm from the correlation value at the respective BEP, which is actually comparable to the other studies. However, a strong disagreement is present for the flowrate deviation, which is 30% for 500 ppm and 45 % for 2000 ppm at the respective best efficiency point. This observation suggests that the relationships might work relatively accurate for Newtonian liquids but fail to predict non-Newtonian fluid performance, a polymer (HPAM) solution in this case. These findings suggest that pump performance prediction with non-Newtonian fluids is much more complex than with Newtonian fluid.

5.5 Derating Curves for Head Correction

In order to design an ESP based on the manufacturer's reference curve, the following charts can be used. It should be mentioned that they base on the performance test conducted with the ESP REDA D2100EZ 400 Series, other pump types might behave differently. The plots show the water manufacturer's reference curve (100%) and the head of the tested polymer fluids. Therefore, the decrease from the water curve to the viscous fluid curve would be the head degradation in percentage at a given flowrate.

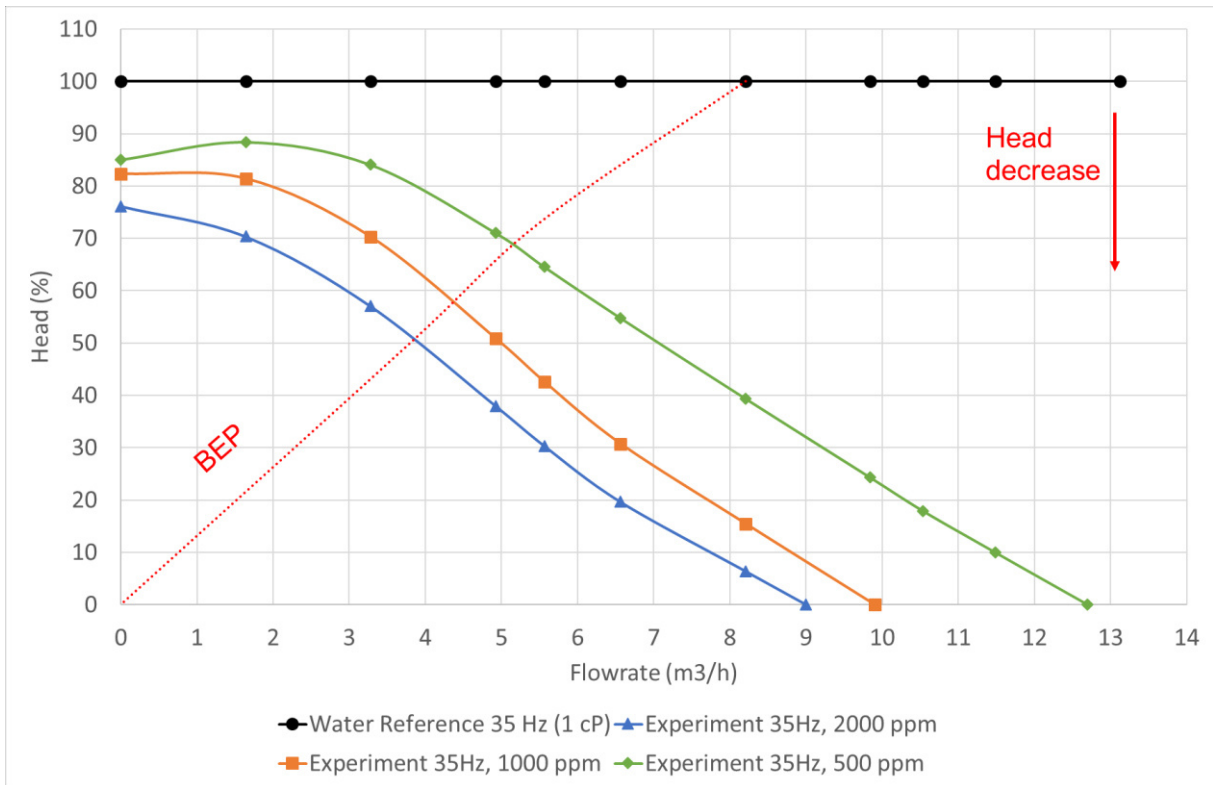


Figure 57: REDA D2100EZ, Derating/Correction chart for 35 Hz

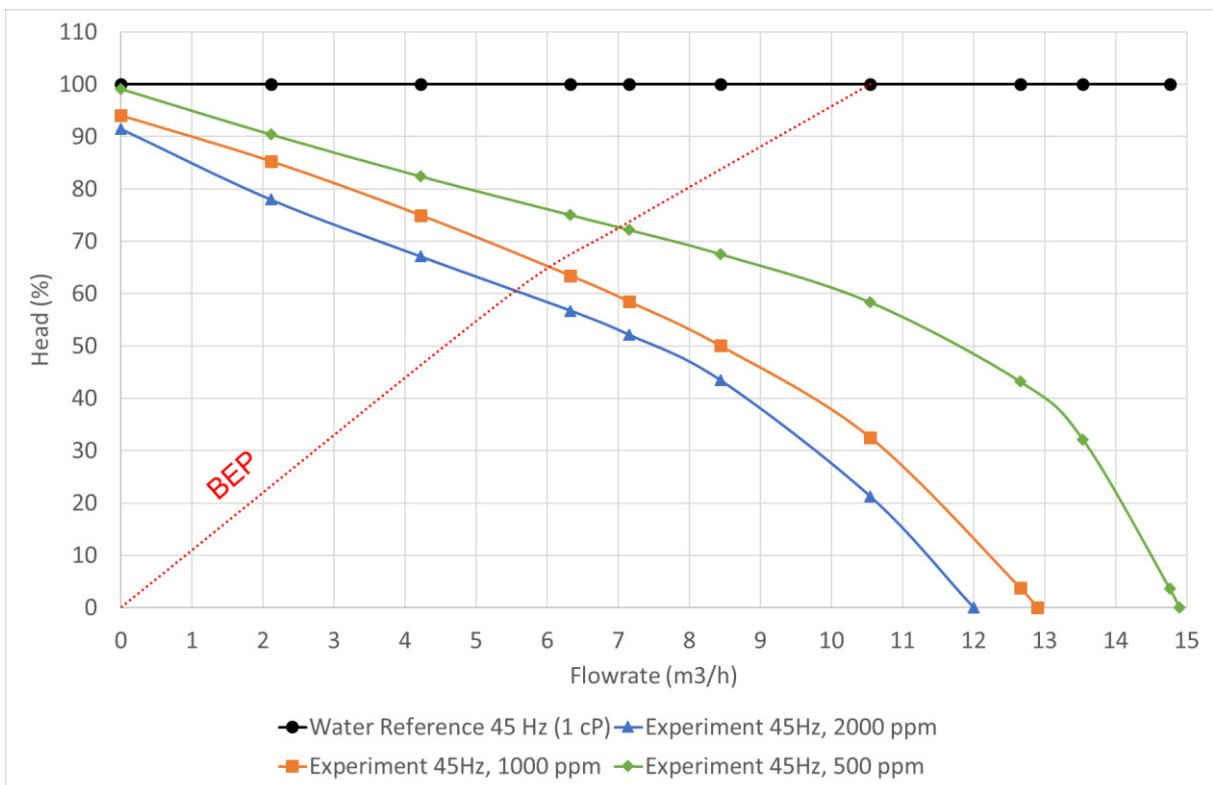


Figure 58: REDA D2100EZ, Derating/Correction chart for 45 Hz

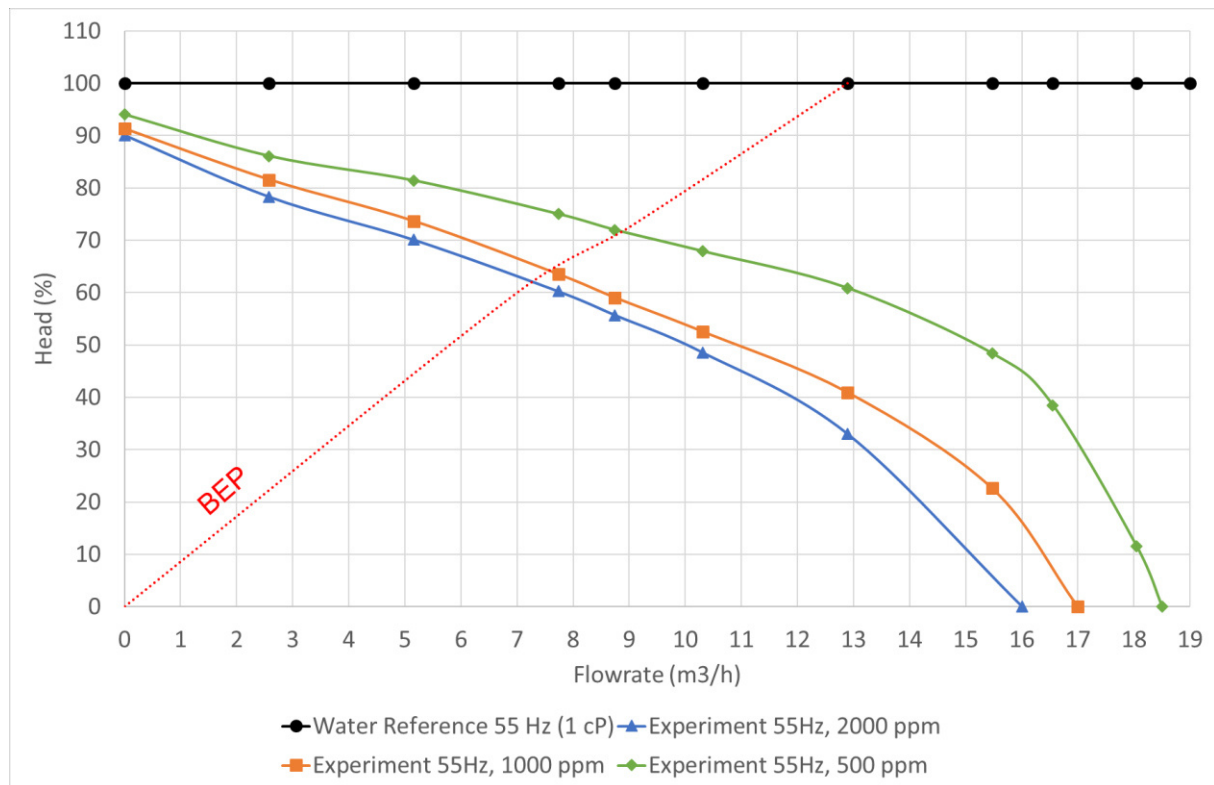


Figure 59: REDA D2100EZ, Derating/Correction chart for 55 Hz

For example, we have 55 Hz rotational speed, and the manufacturer's published water performance curve is 10.3 m³/h with a head of 8.34 m per stage. The 500-ppm performance curve shows a reduction to 68% of the water head, which is 5.67 m per stage. Therefore, compared to water, more stages would be required in order to produce the required head and the desired flow rate. In addition, Figure 35 can be used to see the underlying viscosity for each curve and interpolate between them.

Lastly, Figure 60 shows the head derating curves for the 82-stage REDA D2100EZ compared to the derating curves of the 7-stage REDA D2400N. The curves are based on the experiments with the 500-ppm and the 1000-ppm viscous fluid at 45 Hz rotational speed. It can be seen that the curves differ to some degree. Two main issues could be accountable for this curve differences. First, the rheological complexity of the fluid, like degradation between the tests or also the temperature behavior could have been an issue. The second reason could be the different pumps, specifically the different number of stages and the pump capacity. This observation shows again, how complex the behavior of non-Newtonian liquids is and underpins the necessity of experiments for investigating the pump performance with non-Newtonian liquids.

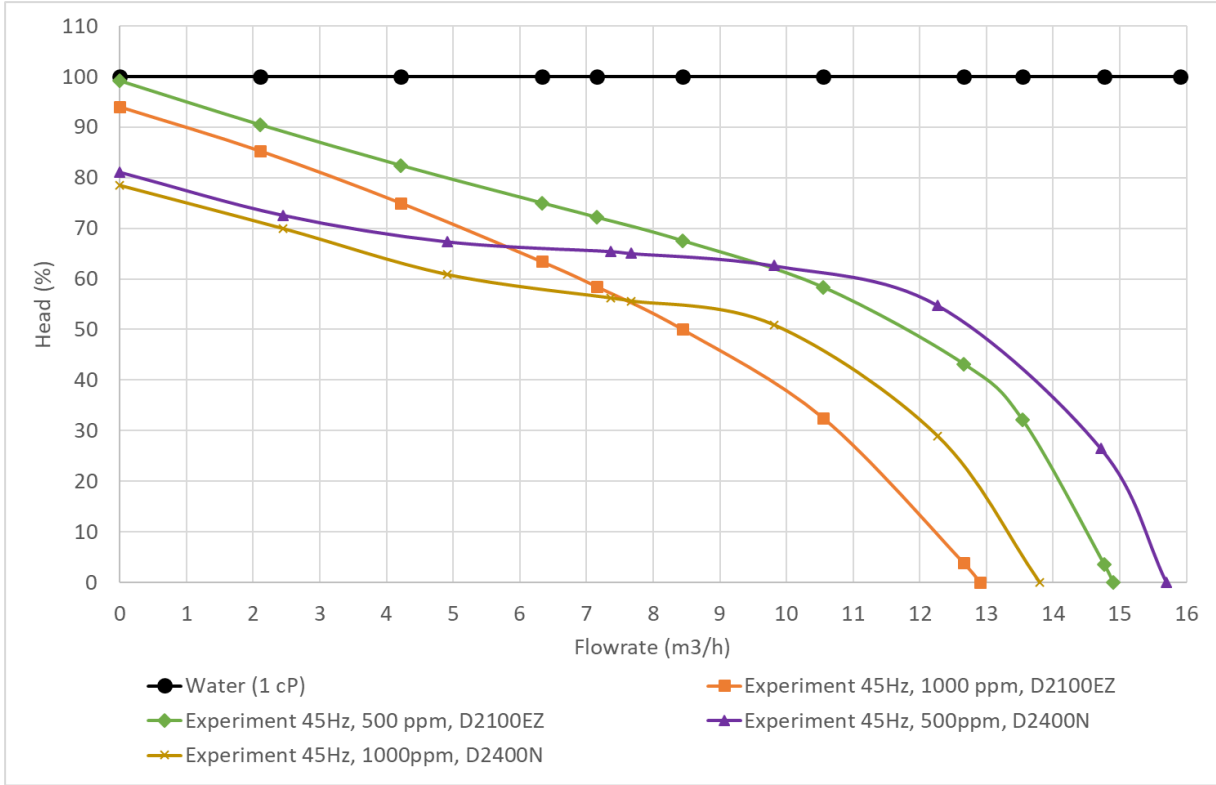


Figure 60: REDA D2100EZ vs REDA D2400N, Derating/Correction chart for 45 Hz

6 Conclusion

Centrifugal pump performance prediction is a very complicated task. Indeed, with the rise of enhanced oil recovery methods such as polymer flooding, it is getting even more difficult. Performance predicting correlations, like the Hydraulic Institute Method, may not hold for these non-Newtonian fluids anymore. In fact, Takacs (2009) recommends complete ESP performance testing with the non-Newtonian fluid under investigation.

This study found that although a low viscous medium was tested, the observed pump performance decrease was substantial as well as unexpected. This has a great impact on the design of electric submersible pumps, especially on the required number of stages required to produce a specific head. The leading cause is expected to be the fluid characteristics of the polymer solution. In addition, there is still no universal correlation for all types of centrifugal pumps for performance prediction available. The tested correlations (Hydraulic Institute Method and Morrison's' Modified Affinity Law) may be applicable for Newtonian liquids but failed for the non-Newtonian HPAM solution.

Furthermore, against all expectations, the viscosity measurements indicate that the electric submersible pump does not heavily shear off the polymer molecular chains. The polymer-laden fluid still shows a recognizable shear-thinning behavior after passing through the pump. An observation that is crucial for the produced water treatment process.

I would highly recommend permanent monitoring of each electric submersible pumps within polymer flooding regions. Collecting data is the key to understand the effects of those fluids better. Additionally, I would suggest continuing electric submersible pump experiments using non-Newtonian liquids. There are still many aspects, which are not understood – for example, the actual forces acting in a pump stage, when non-Newtonian liquids are present. Maybe computational modeling could help to obtain a more in-depth insight into the physics behind the fluid behavior.

References

- Alfa Laval. 2002. Alfa Laval Pump Handbook: All You Need To Know. 2 edition.
- Amaral, G., V. Estevam, and F. A. Franca. 2009. On the Influence of Viscosity on ESP Performance. *SPE Production & Operations* 24(02):303–311. [online] URL: <https://doi.org/10.2118/110661-PA>.
- American Petroleum Institute. 1997. API RP 11S2 - Recommended Practice for Electric Submersible Pump Testing. American Petroleum Institute, Dallas, Texas.
- Anton Paar Wiki. How to measure viscosity. [online] URL: <https://wiki.anton-paar.com/en/how-to-measure-viscosity/>.
- Bellary, S. A., M. H. Siddique, A. Samad, J. S. Sangwai, and B. Chon. 2017. Effects of crude oil-water emulsions at various water-cut on the performance of the centrifugal pump. *International Journal of Oil, Gas and Coal Technology* 16(1):71.
- Bera, A., and A. Mandal. 2015. Microemulsions: a novel approach to enhanced oil recovery: a review. *Journal of Petroleum Exploration and Production Technology* 5(3):255–268. [online] URL: <https://doi.org/10.1007/s13202-014-0139-5>.
- Buijse, M. A., K. Tandon, S. Jain, J.-W. Handgraaf, and J. Fraaije. 2012. Surfactant Optimization for EOR using Advanced Chemical Computational Methods in SPE Improved Oil Recovery Symposium (Tulsa, Oklahoma, USA, 2012-04-14). Society of Petroleum Engineers.
- Buratto, C., M. Occari, N. Aldi, N. Casari, M. Pinelli, P. R. Spina, and A. Suman. 2017. Centrifugal pumps performance estimation with non-Newtonian fluids: review and critical analysis in 12th European Conference on Turbomachinery Fluid Dynamics and hermodynamics (Stockholm, Sweden, 4/3/2017 - 4/7/2017). European Turbomachinery Society.
- Centrilift. 1997. Submersible Pump Handbook. 6th edition, Claremore, Oklahoma.
- Clegg, J. D., and L. W. Lake, editors. 2007. *Petroleum Engineering Handbook: Production Operations*. Society of Petroleum Engineers, Richardson, TX.
- Demin, W., J. Youlin, W. Yan, G. Xiaohong, and W. Gang. 2004. Viscous-Elastic Polymer Fluids Rheology and Its Effect Upon Production Equipment. *SPE Production & Facilities* 19(04):209–216. [online] URL: <https://doi.org/10.2118/77496-PA>.
- Fox, R. W., A. T. McDonald, P. J. Pritchard, and J. C. Leylegian. 2012. *Fluid mechanics*. 8th ed., SI version edition. John Wiley, Hoboken, NJ.
- Graham, L. J. W., L. Pullum, P. Slatter, G. Sery, and M. Rudman. 2009. Centrifugal pump performance calculation for homogeneous suspensions. *The Canadian Journal of Chemical Engineering* 87(4):526–533.
- Grand View Research, I. 2017. Artificial Lift Systems Market Size & Share | Industry Report, 2018-2025. [online] URL: <https://www.grandviewresearch.com/industry-analysis/artificial-lift-systems-market>.
- Gulich, J. F. 1999. Pumping highly viscous fluids with centrifugal pumps — Part 1. *World Pumps* 1999(395):30–34.

- Gulich, J. F. 2014. *Centrifugal Pumps*. 3rd ed. 2014 edition. Springer Berlin Heidelberg, Berlin, Heidelberg, s.l.
- Hammoud, A. H., Yassine K. C., and M. F. Khalil. 2010. Effect of Oil-in-Water Concentration on the Performance of Centrifugal Pump. ICFD10-EG-3067 in Tenth International Congress of Fluid Dynamics (Ain Soukhna, Red Sea, Egypt, 12/16/2010 - 12/19/2010).
- Ippen, A. T. 1946. The influence of viscosity on centrifugal pump performance. *Trans. ASME* 68:823–848. [online] URL: <https://preserve.lehigh.edu/engr-civil-environmental-fritz-lab-reports/1251>.
- Kalombo, J. J. N., R. Haldenwang, R. P. Chhabra, and V. G. Fester. 2014. Centrifugal Pump Derating for Non-Newtonian Slurries. *Journal of Fluids Engineering* 136(3):31302.
- Klier, J., C. J. Tucker, T. H. Kalantar, and D. P. Green. 2000. Properties and Applications of Microemulsions. *Advanced Materials* 12(23):1751–1757. [online] URL: [https://doi.org/10.1002/1521-4095\(200012\)12:23<1751:AID-ADMA1751>3.0.CO;2-I](https://doi.org/10.1002/1521-4095(200012)12:23<1751:AID-ADMA1751>3.0.CO;2-I).
- Lake, L. W. 1989. *Enhanced Oil Recovery*. Prentice Hall, Englewood Cliffs, N.J.
- Le Fur, B., M. Cato Knutsen, and C. Becki. 2015. High Viscosity Test Of A Crude Oil Pump. [online] URL: <http://www.eureka.no/wp-content/uploads/2016/02/lecture-project-V30-2.pdf>.
- Lim, J. S., S. F. Wong, M. C. Law, Y. Samyudia, and S. S. Dol. 2015. A Review on the Effects of Emulsions on Flow Behaviours and Common Factors Affecting the Stability of Emulsions. *Journal of Applied Sciences* 15(2):167–172.
- Menon, E. S., editor. 2011. *Pipeline Planning and Construction Field Manual*. Elsevier/GPP Gulf Professional Publ, Amsterdam.
- Metzner, A. B., and R. E. Otto. 1957. Agitation of non-Newtonian fluids. *AIChE Journal* 3(1):3–10.
- Morales, R., E. Pereyra, S. Wang, and O. Shoham. 2013. Droplet Formation Through Centrifugal Pumps for Oil-in-Water Dispersions. *SPE Journal* 18(01):172–178.
- Morrison, G., W. Yin, R. Agarwal, and A. Patil. 2017. Evaluation of Effect of Viscosity on an Electrical Submersible Pump. Pages V01AT05A010 in *Proceedings of the ASME Fluids Engineering Division Summer Meeting 2017 (Waikoloa, Hawaii, USA, Sunday 30 July 2017)*. American Society of Mechanical Engineers, New York, N.Y.
- Morrison, G., W. Yin, R. Agarwal, and A. Patil. 2018. Development of Modified Affinity Law for Centrifugal Pump to Predict the Effect of Viscosity. *Journal of Energy Resources Technology* 140(9):92005. [online] URL: <https://doi.org/10.1115/1.4039874>.
- Moura Junior, M. D. 2016. *Experimental Study of Water-Oil Two-Phase Flow in an 8-Stage Electric Submersible Pump*. Dissertation. Univeristy of Campinas, Campinas.
- Ofuchi, E. M., H. Stel, T. Sirino, R. Dunaiski, and R. E. M. Morales. 2015. Numerical Analysis of Performance Degradation in Multistage Electric Submersible Pumps in H. S. d. C. Mattos, editor. 23rd ABCM International Congress of Mechanical Engineering (Rio de Janeiro, Brazil, 06.12.2015 - 11.12.2015). ABCM Brazilian Society of Mechanical Sciences and Engineering Rio de Janeiro, Brazil.
- Ott, H. 2018. *Enhanced Oil Revocery Lecture Slides: Polymer Methods*, Montanuniversität Leoben.

- Pal, R. 1996. Effect of droplet size on the rheology of emulsions. *AIChE Journal* 42(11):3181–3190.
- Paternost, G. M., A. C. Bannwart, and V. Estevam. 2015. Experimental Study of a Centrifugal Pump Handling Viscous Fluid and Two-Phase Flow. *SPE Production & Operations* 30(02):146–155. [online] URL: <https://doi.org/10.2118/165028-PA>.
- Patil, A., and G. Morrison. 2019. Affinity Law Modified to Predict the Pump Head Performance for Different Viscosities Using the Morrison Number. *Journal of Fluids Engineering* 141(2):21203.
- Patil, A., G. Morrison, A. Delgado, and H. Casillas. 2018. Centrifugal Pump Head Prediction using Affinity Laws Modified for Viscosity in SPE Artificial Lift Conference and Exhibition - Americas (The Woodlands, Texas, USA, 2018-08-20). Society of Petroleum Engineers.
- Petrowiki. Oil emulsions. [online] URL: https://petrowiki.org/Oil_emulsions.
- Polymerdatabase. 2017. Flow Properties of Polymers. [online] URL: <http://polymerdatabase.com/polymer%20physics/Viscosity2.html>.
- Prince, L. M. 1977. *Microemulsions: Theory and practice*. Academic Press, New York.
- Pullum, L., L. Graham, and M. Rudman. 2007. Centrifugal pump performance calculation for homogeneous and complex heterogeneous suspensions. *The Journal of The Southern African Institute of Mining and Metallurgy* 107:373–379. [online] URL: https://journals.co.za/content/saimm/107/6/AJA0038223X_3327.
- pumps.org. Classification by Specific Speed. [online] URL: <http://pumps.org/Source/Wireframes/PumpBasicsDiagramPage.aspx?pageid=2535>.
- Sheng, J. J. 2011. *Modern Chemical Enhanced Oil Recovery: Theory and Practice*. Gulf Professional Publ, Burlington, Mass.
- Sheng, J. J. 2013. *Enhanced Oil Recovery Field Case Studies*. Elsevier/GPP Gulf Professional Publ, Amsterdam.
- Sorbie, K. S. 1991. *Polymer-Improved Oil Recovery*. Springer Netherlands, Dordrecht, s.l.
- Stel, H., T. Sirino, P. R. Prohmann, F. Ponce, S. Chiva, and R. E. M. Morales. 2014. CFD Investigation of the Effect of Viscosity on a Three-Stage Electric Submersible Pump. Pages V01BT10A029 in *Proceedings of the ASME Fluids Engineering Division summer meeting - 2014: Presented at the ASME 2014 4th Joint US-European Fluids Engineering Division Summer Meeting; August 3-7, 2014, Chicago, Illinois, USA (Chicago, Illinois, USA, Sunday 3 August 2014)*. ASME, New York, NY.
- Stepanoff, A. J. 1957. *Centrifugal and axial flow pumps: Theory, design, and application*. Krieger, Malabar (Florida).
- Tagavifar, M., S. Herath, U. P. Weerasooriya, K. Sepehrnoori, and G. Pope. 2018. Measurement of Microemulsion Viscosity and Its Implications for Chemical Enhanced Oil Recovery. *SPE Journal* 23(01):66–83. [online] URL: <https://doi.org/10.2118/179672-PA>.
- Takács, G. 2009. *Electrical submersible pumps manual: Design, operations, and maintenance*. Gulf Professional Publ./Elsevier, Amsterdam.
- Thomas, A. 2016. Polymer Flooding in L. Romero-Zeron, editor. *Chemical Enhanced Oil Recovery (cEOR) - a Practical Overview*. InTech.

Thomas, A., N. Gaillard, and C. Favero. 2012. Some Key Features to Consider When Studying Acrylamide-Based Polymers for Chemical Enhanced Oil Recovery. *Oil & Gas Science and Technology – Revue d'IFP Energies nouvelles* 67(6):887–902.

Trevisan, F. E., and M. Prado. 2011. Experimental Investigation of the Viscous Effect on Two-Phase-Flow Patterns and Hydraulic Performance of Electrical Submersible Pumps. *Journal of Canadian Petroleum Technology* 50(04):45–52. [online] URL: <https://doi.org/10.2118/134089-PA>.

Turzo, Z., G. Takacs, and J. Zsuga. 2000. Equations correct centrifugal pump curves for viscosity. *Oil and Gas Journal* 98.

Walker, C. I., and A. Goulas. 1984. Performance Characteristics of Centrifugal Pumps When Handling Non-Newtonian Homogeneous Slurries. *Proceedings of the Institution of Mechanical Engineers, Part A: Power and Process Engineering* 198(1):41–49.

White, F. M. 2011. *Fluid mechanics*. 7. ed. in SI units edition. McGraw-Hill, Singapore.

List of Tables

Table 1: Summary of polymer types	7
Table 2: Emulsion types and classification	12
Table 3: Acceptance limits for the manufacturer's published performance curves	18
Table 4: Centrifugal viscosity correction factors	29
Table 5: Experimental Matrix and Boundary Conditions	35
Table 6: Measurements	36
Table 7: REDA D2100EZ, water performance at the respective best efficiency point	50
Table 8: REDA D2100EZ, 500-ppm performance at the respective best efficiency point	50
Table 9: REDA D2100EZ, 1000-ppm performance at the respective best efficiency point	50
Table 10: REDA D2100EZ, 2000-ppm performance at the respective best efficiency point	50
Table 11: REDA D2100EZ, Pressure development (increase) at shut-in	51
Table 12: REDA D2400N, water performance at the respective best efficiency point	55
Table 13: Viscosity measurements during REDA D2100EZ pump tests, Brookfield at 30°C and 6 rpm	55
Table 14: REDA D2400N stage pressure increase over time (loop pumping)	62
Table 15: REDA D2100EZ efficiency loss of the viscous tests compared to the water tests at the respective best efficiency point	65
Table 16: REDA D2400N efficiency loss of the viscous tests compared to the water tests at the best efficiency point	66
Table 17: Start torque increase when pumping polymer-laden fluids compared to water (REDA D2100EZ tests)	66
Table 18: Pump Test Facility Equipment	86
Table 19: Pump Test Facility Sensors	86
Table 20: REDA D2100EZ Experiments	113
Table 21: REDA D2400N Experiments	114

List of Figures

Figure 1: (a) Head degradation of a Newtonian fluid (b) and a non-Newtonian fluid	1
Figure 2: Schematic illustration of an electric submersible pump installation	3
Figure 3: Electric submersible pump stage	4
Figure 4: Pump performance curve and the associated losses.....	5
Figure 5: Enhanced oil recovery methods overview.....	6
Figure 6: (a) Xanthan gum (b) Partially hydrolyzed polyacrylamide (HPAM).....	7
Figure 7: Effect of polymer concentration on polymer viscosity.....	8
Figure 8: Shear stress versus shear rate - behavior types.....	9
Figure 9: Comparison of power-law and Carrerau model.....	10
Figure 10: Viscosity of different polymers versus concentration and different molecular weights.....	11
Figure 11: Micro-emulsion types and phase behavior.....	13
Figure 12: Winsor ratio concept and the interfacial curvature	13
Figure 13: Microemulsion viscosity as a function of oil/water content	14
Figure 14: Emulsion viscosity versus shear rate	15
Figure 15: (a) 3000 ppm HPAM 70°F,(b) 2000 ppm HPAM 60°C	15
Figure 16: API RP 11S2 - Five performance test points, modified from Takács (2009).....	16
Figure 17: API – pump test acceptance limits.....	18
Figure 18: Impeller type vs. specific speed (n_s and n_q).....	20
Figure 19: Typical Hydraulic Institute viscosity correction chart for 2 – 8-inch pumps.....	21
Figure 20: Illustration of the Hydraulic Institute correction method.....	22
Figure 21: Correction factors for head and efficiency.....	24
Figure 22: Morrison's modified affinity law charts with data based on Le Fur.....	28
Figure 23: Viscoelastic fluid effect on centrifugal pumps.....	31
Figure 24: Pump test facility – flow loop	33
Figure 25: (a) Sampling device mounted in the facility, (b) Schematic of the sampling device	38
Figure 26: Intake pressure analysis with 35Hz rotational speed (REDA D2100EZ)	40

Figure 27: REDA D2100EZ head and brake horsepower curve – catalog versus 3500 RPM closed-loop experiments with water (1 cP and 1 S.G.)	41
Figure 28: REDA D2100EZ head Curve – catalog versus 35, 45 and 55 Hz closed loop Experiments with water (1 cP and 1 S.G.)	42
Figure 29: REDA D2100EZ brake horsepower curve – catalog versus 35, 45 and 55 Hz closed-loop experiments with water (1 cP and 1 S.G.)	43
Figure 30: REDA D2100EZ efficiency curve – catalog versus 35, 45 and 55 Hz closed-loop experiments with water (1 cP and 1 S.G.)	43
Figure 31: REDA D2400N head and brake horsepower curve – catalog versus 2917 RPM closed-loop experiments with water (1 cP and 1 S.G.)	45
Figure 32: REDA D2400N head Curve – catalog versus 35, 45 and 55 Hz closed loop Experiments with water (1 cP and 1 S.G.)	45
Figure 33: REDA D2400N brake horsepower curve – catalog versus 35, 45 and 55 Hz closed-loop experiments with water (1 cP and 1 S.G.)	46
Figure 34: REDA D2400N efficiency curve – catalog versus 35, 45 and 55 Hz closed-loop experiments with water (1 cP and 1 S.G.)	46
Figure 35: Viscosity profile for each polymer (HPAM) concentration at its test temperature (sample taken from the pressure tank before each test), REDA D2100EZ experiments	48
Figure 36: REDA D2100EZ head and brake horsepower curve – 45 Hz polynomial model (water, 1 cP and 1 S.G.) versus polymeric fluid performance (2000 ppm at 30°C)	48
Figure 37: REDA D2100EZ efficiency curve – 45 Hz polynomial model (water, 1 cP and 1 S.G.) versus polymeric fluid performance (2000 ppm at 30°C)	49
Figure 38: REDA D2100EZ shut-in pressure for water, 500 ppm, 1000 ppm, and 2000-ppm HPAM solution at 35 and 45 Hz.....	51
Figure 39: REDA D2100EZ hydraulic and mechanical power (open loop water test with 45 Hz)	52
Figure 40: REDA D2100EZ hydraulic and mechanical power (open loop 1000-ppm HPAM with 45 Hz)	52
Figure 41: REDA D2100EZ startup torque measurements	53
Figure 42: Viscosity profile for each polymer (HPAM) concentration at its test temperature (sample from the 200-liter casing before each test), REDA D2400N experiments	54
Figure 43: REDA D2400N head and brake horsepower curve – 45 Hz polynomial model (water, 1 cP and 1 S.G.) versus polymeric fluid performance	54
Figure 44: Viscosity profile of the 2000-ppm fluid samples at 25°C (REDA D2100EZ tests)	56
Figure 45: Viscosity profile of the 1000-ppm and 500-ppm fluid samples at 16°C (REDA D2400N tests)	56

Figure 46: a) Diffusers with pressure sensing, b) Pressure sensor screwed into the pump casing, c) Pressure sensors connected to each stage of the REDA D2400N pump	57
Figure 47: Reassembled REDA D2400N head and brake horsepower curve – 45 Hz polynomial model (water, 1 cP and 1 S.G.) versus polymeric fluid performance	58
Figure 48: Reassembled REDA D2400N head curve for each stage – 45 Hz polynomial model fit	58
Figure 49: Reassembled REDA D2400N head development from stage 1 to 7 at 45 Hz speed and 7 m ³ /h flowrate	59
Figure 50: Reassembled REDA D2400N, head difference from stage 1 to 7 at 45 Hz speed and 7 m ³ /h flowrate	60
Figure 51: Reassembled REDA D2400N, pressure development from stage 1 to 7 during startup (ramp: 2 s/Hz, final speed: 45 Hz)	61
Figure 52: Reassembled REDA D2400N single-stage pressure (discharge minus intake) versus flowrate during loop pumping of a 1000-ppm HPAM solution	62
Figure 53: Reassembled REDA D2400N head curve development at a constant choke opening during loop pumping of a 1000-ppm HPAM solution	63
Figure 54: Reassembled REDA D2400N total hydraulic power and total mechanical power during loop pumping of a 1000-ppm HPAM solution	64
Figure 55: (a) Iron and oxygen-induced polymer viscosity loss over time, (b) chemical degradation of a 10 million g/mole polymer, (c) shear degradation of a 20 million g/mole polymer, (d) polymer solution viscosity versus shear stress	67
Figure 56: REDA D2100EZ experiments compared with HI and Morrison correlation using real viscosity	69
Figure 57: REDA D2100EZ, Derating/Correction chart for 35 Hz	70
Figure 58: REDA D2100EZ, Derating/Correction chart for 45 Hz	70
Figure 59: REDA D2100EZ, Derating/Correction chart for 55 Hz	71
Figure 60: REDA D2100EZ vs REDA D2400N, Derating/Correction chart for 45 Hz	72
Figure 60: Pneumatic regulating valve and sampling device	87
Figure 61: Electric motor and torque sensor	87
Figure 62: Pump discharge (REDA D2100EZ)	88
Figure 63: Flowmeter, emergency shut-in valve and pump intake (REDA D2100EZ)	88
Figure 64: Open-loop setup with pressure tank, IBC and air-pressure bottle system	89
Figure 65: REDA D2400N installed in the facility	89
Figure 66: REDA D2100EZ – Pump Performance Curve 60 Hz	90

Figure 67: REDA D2100EZ – Pump Performance Curve 50 Hz	90
Figure 68: REDA D2400N – Pump Performance Curve.....	91
Figure 69: REDA D2400N – Pump Performance Curve for different Speeds.....	92
Figure 70: REDA D2100EZ pump	93
Figure 71: REDA D2400N pump	93
Figure 72: Dismantled REDA D2400N pump.....	94
Figure 73: Intake Pressure Analysis with 45Hz Rotational Speed (REDA D2100EZ).....	95
Figure 74: Intake Pressure Analysis with 35Hz Rotational Speed (REDA D2100EZ).....	95
Figure 75: REDA D2100EZ Efficiency Curve – Catalogue versus 3500 RPM Closed Loop Experiments with Water (1 cP and 1 S.G.)	96
Figure 76: REDA D2100EZ Head Curve – 35, 45 and 55 Hz Open Loop Experiments compared with Closed Loop Polynomial Fits using Water as Test Fluid (1 cP and 1 S.G.)	96
Figure 77: REDA D2100EZ Break Horsepower Curve – 35, 45 and 55 Hz Open Loop Experiments compared with Closed Loop Polynomial Fit using Water as Test Fluid (1 cP and 1 S.G.).....	97
Figure 78: REDA D2100EZ Efficiency Curve – 35, 45 and 55 Hz Open Loop Experiments compared with Closed Loop Polynomial Fit using Water as Test Fluid (1 cP and 1 S.G.)	97
Figure 79: REDA D2100EZ 3 rd order polynomial model (head) from 35, 45 and 55 Hz experiments with water (1 cP and 1 S.G.)	98
Figure 80: REDA D2100EZ 4 th order polynomial model (brake horsepower) from 35, 45 and 55 Hz experiments with water (1 cP and 1 S.G.)	98
Figure 81: REDA D2100EZ Polynomial Model (Efficiency) from 35, 45 and 55 Hz Experiments with Water (1 cP and 1 S.G.)	99
Figure 82: REDA D2400N Efficiency Curve – Catalogue versus 2917 RPM Closed Loop Experiments with Water (1 cP and 1 S.G.)	99
Figure 83: REDA D2100EZ 4 th order polynomial model (head) from 35, 45 and 55 Hz experiments with water (1 cP and 1 S.G.)	100
Figure 84: REDA D2100EZ 4 th order polynomial model (brake horsepower) from 35, 45 and 55 Hz experiments with water (1 cP and 1 S.G.)	100
Figure 85: REDA D2400N Polynomial Model (Efficiency) from 35, 45 and 55 Hz Experiments with Water (1 cP and 1 S.G.).....	101
Figure 86: REDA D2100EZ head and brake horsepower curve – 35 Hz polynomial model (water, 1 cP and 1 S.G.) versus polymeric fluid performance (2000 ppm at 25°C)	101

Figure 87: REDA D2100EZ efficiency curve – 35 Hz polynomial model (water, 1 cP and 1 S.G.) versus polymeric fluid performance (2000 ppm at 25°C).....	102
Figure 88: REDA D2100EZ head and brake horsepower curve – 55 Hz polynomial model (water, 1 cP and 1 S.G.) versus polymeric fluid performance (2000 ppm at 30°C)	102
Figure 89: REDA D2100EZ efficiency curve – 55 Hz polynomial model (water, 1 cP and 1 S.G.) versus polymeric fluid performance (2000 ppm at 30°C).....	103
Figure 90: REDA D2400N efficiency curve – 45 Hz polynomial model (water, 1 cP and 1 S.G.) versus polymeric fluid performance	103
Figure 92: Reassembled REDA D2400N head and brake horsepower curve – 45 Hz test points versus initial experimental polynomial model (water, 1 cP and 1 S.G.).....	104
Figure 92: Reassembled REDA D2400N efficiency curve – 45 Hz test points versus initial experimental polynomial model (water, 1 cP and 1 S.G.)	104
Figure 94: Reassembled REDA D2400N efficiency curve – 45 Hz polynomial model (water, 1 cP and 1 S.G.) versus polymeric fluid performance	105
Figure 94: Double-gap measuring systems	107
Figure 95: Temperature profile of the three polymer concentrations at 6 rpm	108
Figure 96: Viscosity profile of the 1000-ppm fluid samples at 15 °C (REDA D2100EZ tests)	108
Figure 97: Viscosity profile of the 500-ppm fluid samples at 20 °C (REDA D2100EZ tests)	109
Figure 98: Viscosity profile for each polymer (HPAM) concentration at 50 °C (sample from the pressure tank prior to each test), REDA D2100EZ experiments	109
Figure 99: Viscosity profile of the 2000-ppm fluid samples at 50 °C (REDA D2100EZ tests)	110
Figure 100: Viscosity profile of the 1000-ppm fluid samples at 50 °C (REDA D2100EZ tests)	110
Figure 101: Viscosity profile of the 500-ppm fluid samples at 50 °C (REDA D2100EZ tests)	111

Abbreviations

API	American Petroleum Institute
AT	After Test
BEP	Best Efficiency Point
BHP	Brake Horsepower
BT	Before Test
DPE	Department of Petroleum Engineering
ESP	Electric Submersible Pump
HI	Hydraulic Institute
HPAM	Partially Hydrolysed Polyacrylamide
IBC	Intermediate Bulk Container (1,000 liter)
IFT	Interfacial Tension
maxRR	Maximum recommended operating range
minRR	Minimum recommended operating range
PAM	Polyacrylamide
PCCL	Polymer Competence Center Leoben GmbH
PLC	Programmable Logic Controller
PPP	Petroleum Production and Processing
RP	Recommended Practise
SPE	Society of Petroleum Engineers
SRP	Sucker Rod Pump
SSU	Saybolt Seconds Universal Unit
VSD	Variable Speed Drive

Nomenclature

BHP	Brake horsepower [kW or hp]
c	Polymer concentration [g/dl]
D	Pump impeller diameter
EFF	Pump efficiency [%]
g	Earth acceleration [m/s^2]
H	Pump head [m or ft]
M	Molecular weight [g/mol]
N	Pump speed [rpm]
n_s	Pump specific speed in US notation
n_q	Pump specific speed in European notation
P_{hydr}	Pump hydraulic power
Q	Flow rate [m^3/h or bpd]
T	Torque [Nm]
ΔP_{pump}	Pressure developed by the pump, discharge minus intake pressure [Pa]
ρ	Density [kg/m^3]
μ	Dynamic viscosity [$N.s/m^2$ or cP]
μ_∞	Limitng Viscosity at high shear rates [$N.s/m^2$ or cP]
μ_p	Apparent viscosity [$N.s/m^2$ or cP]
ν	Kinematic viscosity [m^2/s or cSt]
$[\eta]$	Intrinsic viscosity [dl/g]
γ	Specific gravity, S.G. [-]
$\dot{\gamma}$	Shear rate [$1/s$]
ω	Rotational speed [rad/s]
ψ	Head coefficient
π	Power coefficient
ϕ	Flow coefficient

Appendices

Appendix A – Pump Test Facility

Table 18 shows the different components of the pump testing facility:

Table 18: Pump Test Facility Equipment

Equipment	Type/Model	Specifications
Pressure Tank		1,500 liter volume
Heat exchanger		20 kW
Air-pressure bottle system	Air Liquide	600 liter, 200 bar battery
Variable Speed Drive	Bosch Rexroth – EFC 5610	
Electric Motor	Siemens	55 kW
Pneumatic Control Valve	RTK – PV 6411	
Pneumatic Control Valve Control	Bürkert 8793	
Programmable Logic Controller	Bosch Rexroth – IndraContol L25	

Table 19 shows the different measurement devices used in the facility:

Table 19: Pump Test Facility Sensors

Equipment	Type/Model	Specifications/Purpose
Level Sensor	OLS – C20	Liquid level inside pressure tank
Flowmeter	FLOWMAG 3000	Magnetic flowmeter
Temperature Sensor		4... 20 mA-Output
Pressure Sensor		4... 20 mA-Output
Torque Sensor	HBM – T40B	



Figure 61: Pneumatic regulating valve and sampling device



Figure 62: Electric motor and torque sensor



Figure 63: Pump discharge (REDA D2100EZ)

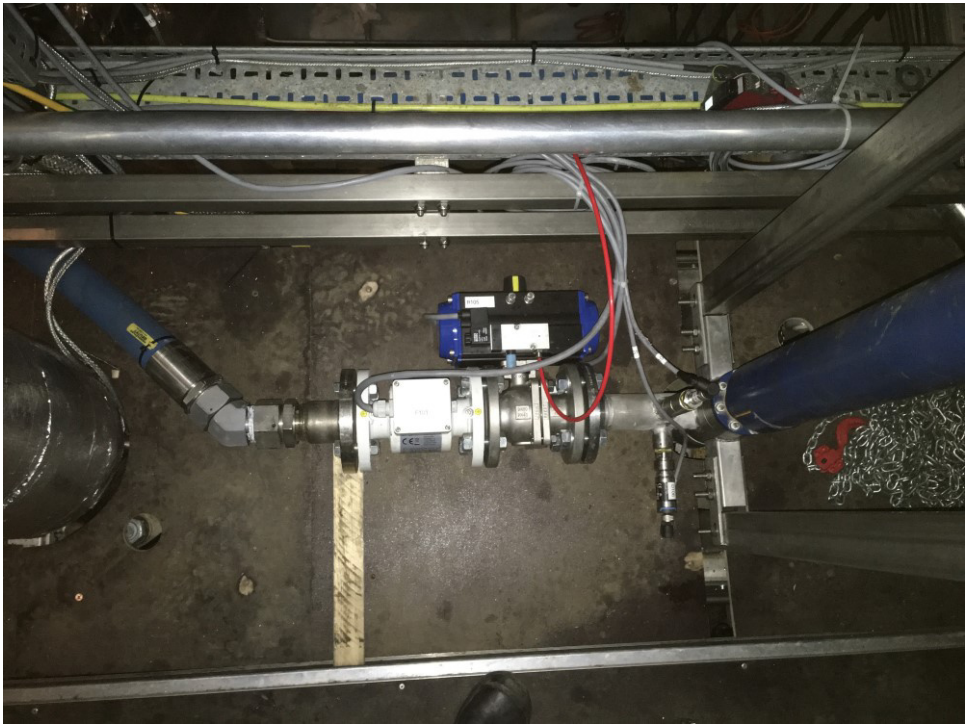


Figure 64: Flowmeter, emergency shut-in valve and pump intake (REDA D2100EZ)

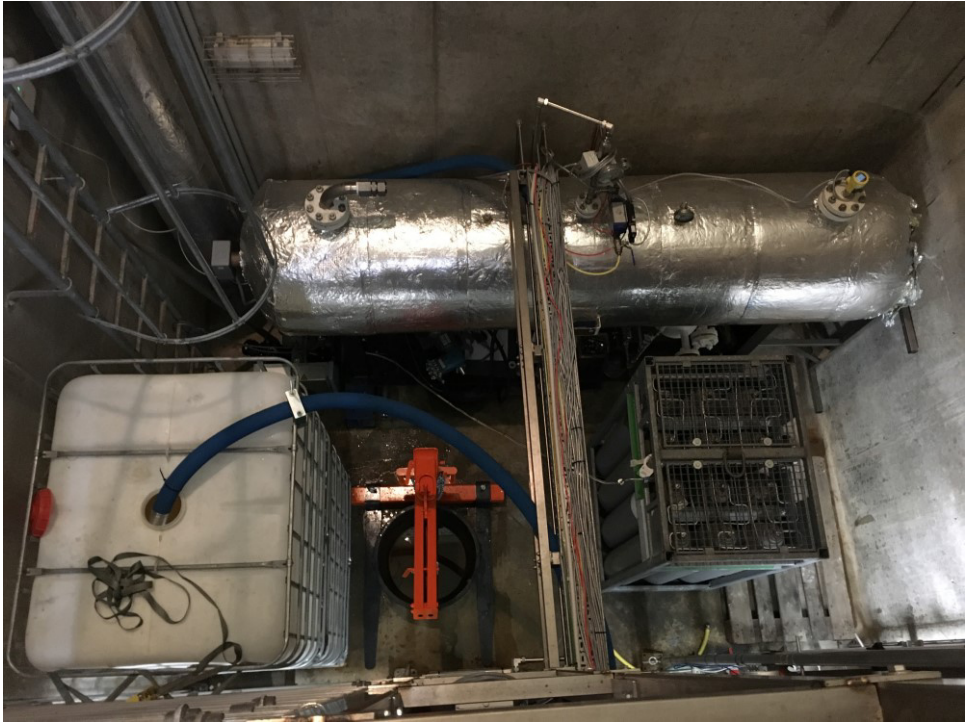


Figure 65: Open-loop setup with pressure tank, IBC and air-pressure bottle system



Figure 66: REDA D2400N installed in the facility

Appendix B – Electric Submersible Pumps

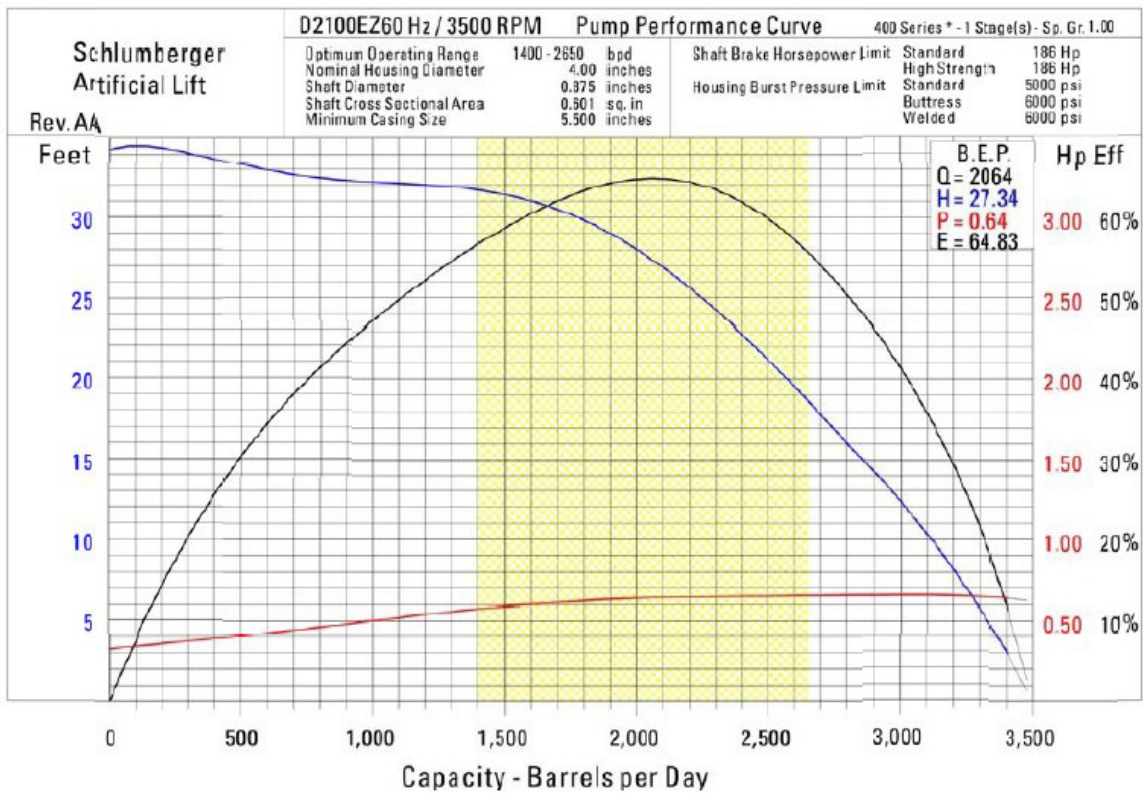


Figure 67: REDA D2100EZ – Pump Performance Curve 60 Hz

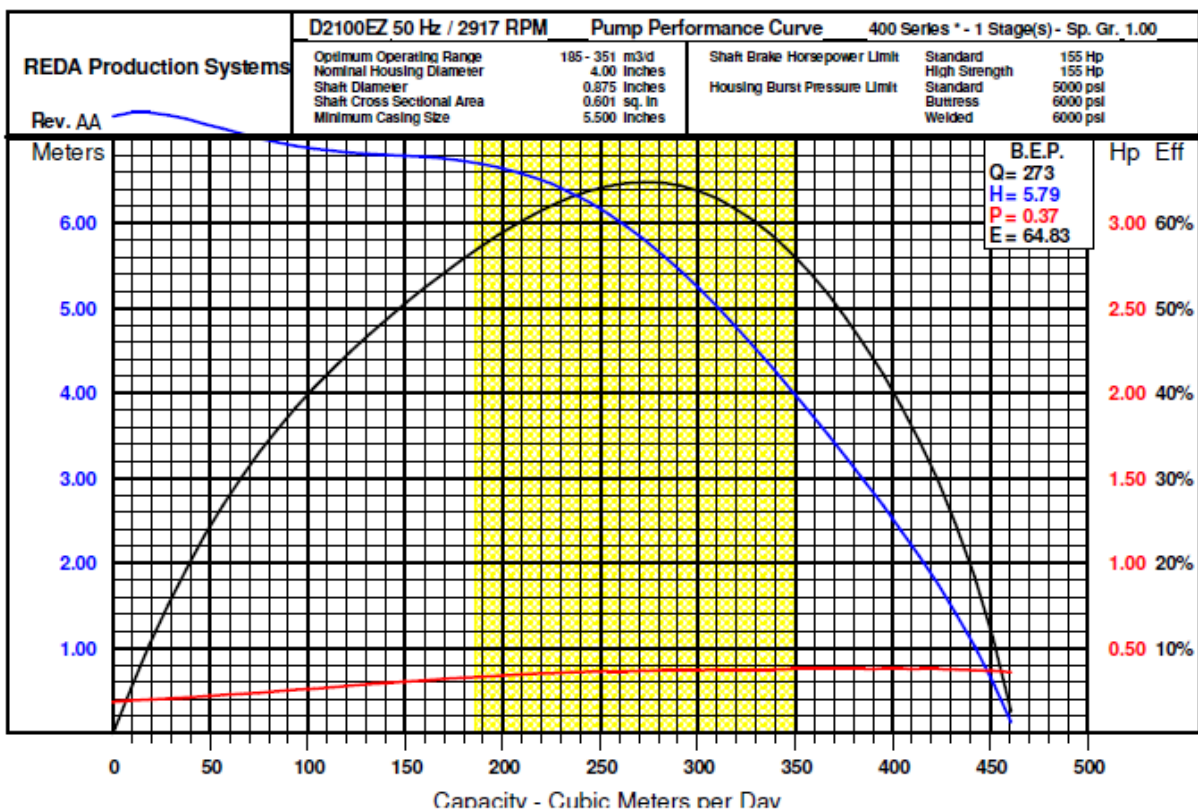


Figure 68: REDA D2100EZ – Pump Performance Curve 50 Hz

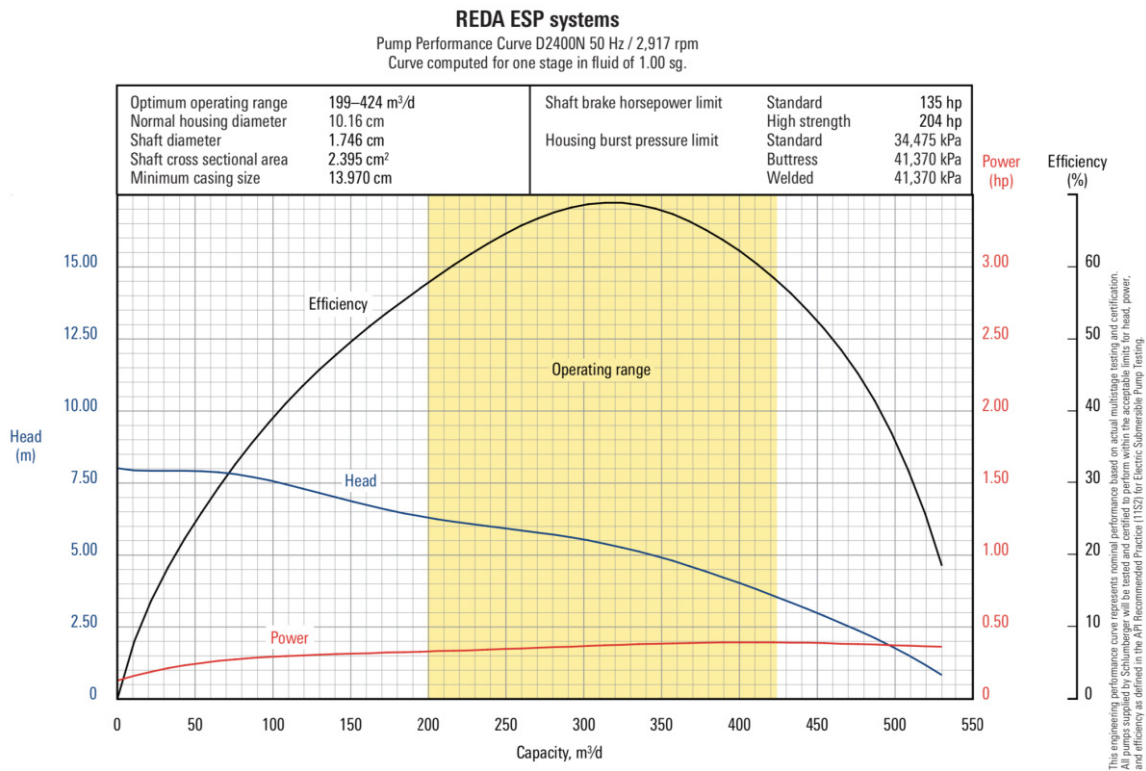


Figure 69: REDA D2400N – Pump Performance Curve

REDA ESP systems
 Pump Performance Curve D2400N
 Curve computed for one stage in fluid of 1.00 sg.

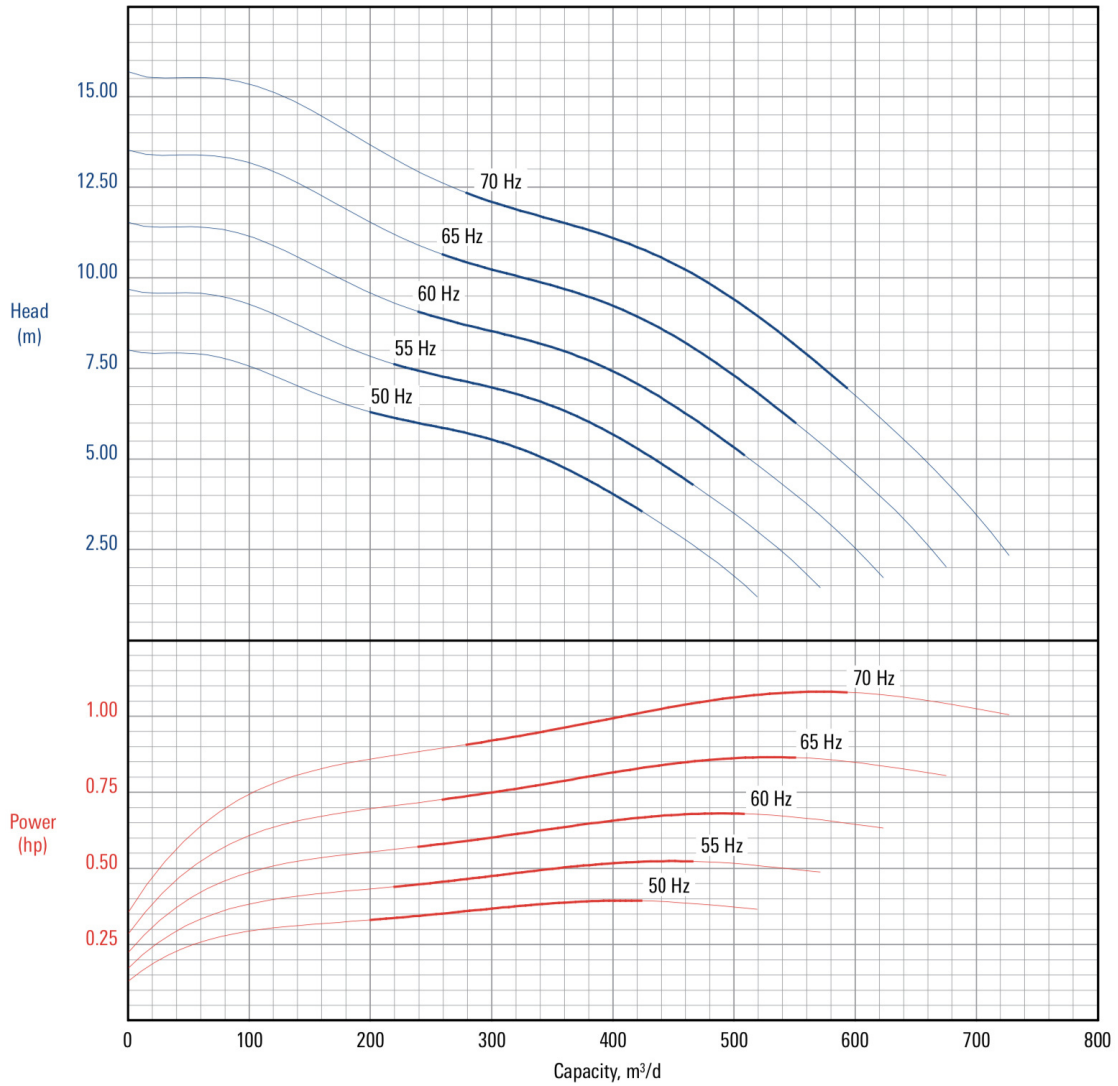


Figure 70: REDA D2400N – Pump Performance Curve for different Speeds



Figure 71: REDA D2100EZ pump



Figure 72: REDA D2400N pump



Figure 73: Dismantled REDA D2400N pump

Appendix C – Additional Pump Test Plots

REDA D2100EZ intake pressure analysis:

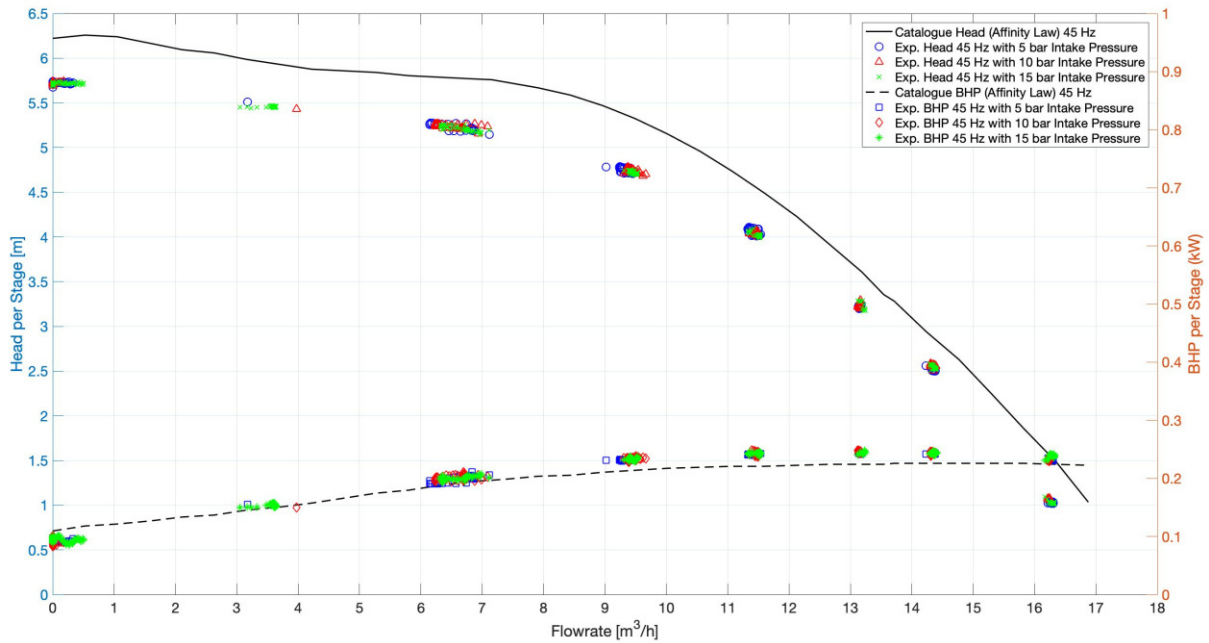


Figure 74: Intake Pressure Analysis with 45Hz Rotational Speed (REDA D2100EZ)

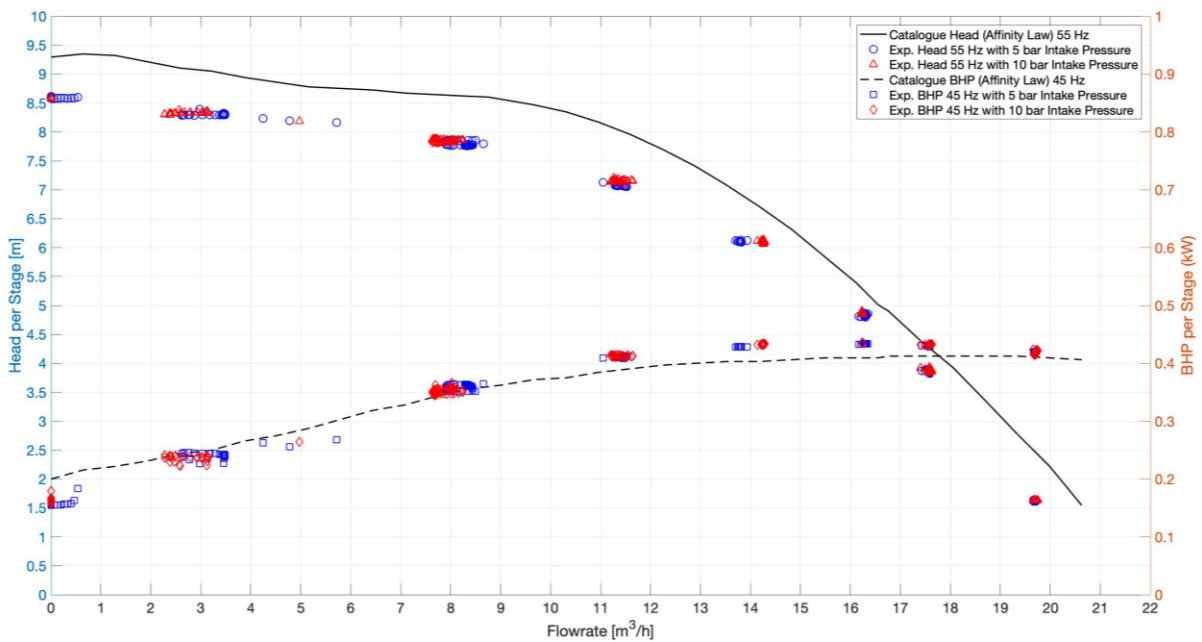


Figure 75: Intake Pressure Analysis with 35Hz Rotational Speed (REDA D2100EZ)

REDA D2100EZ water performance plots:

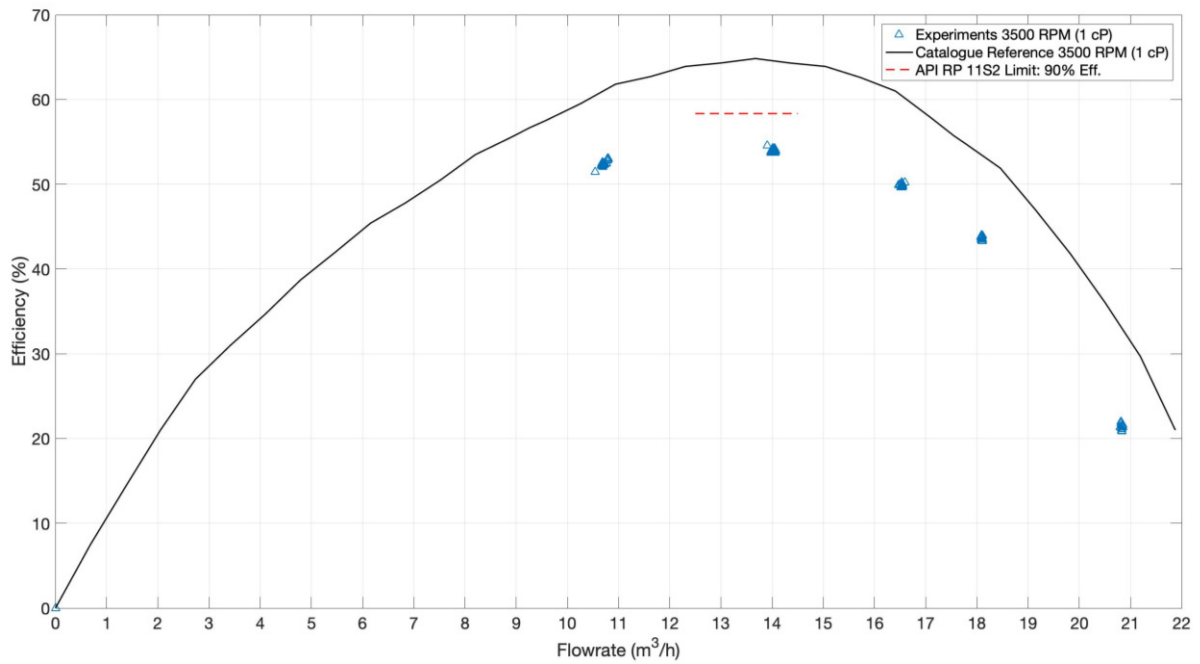


Figure 76: REDA D2100EZ Efficiency Curve – Catalogue versus 3500 RPM Closed Loop Experiments with Water (1 cP and 1 S.G.)

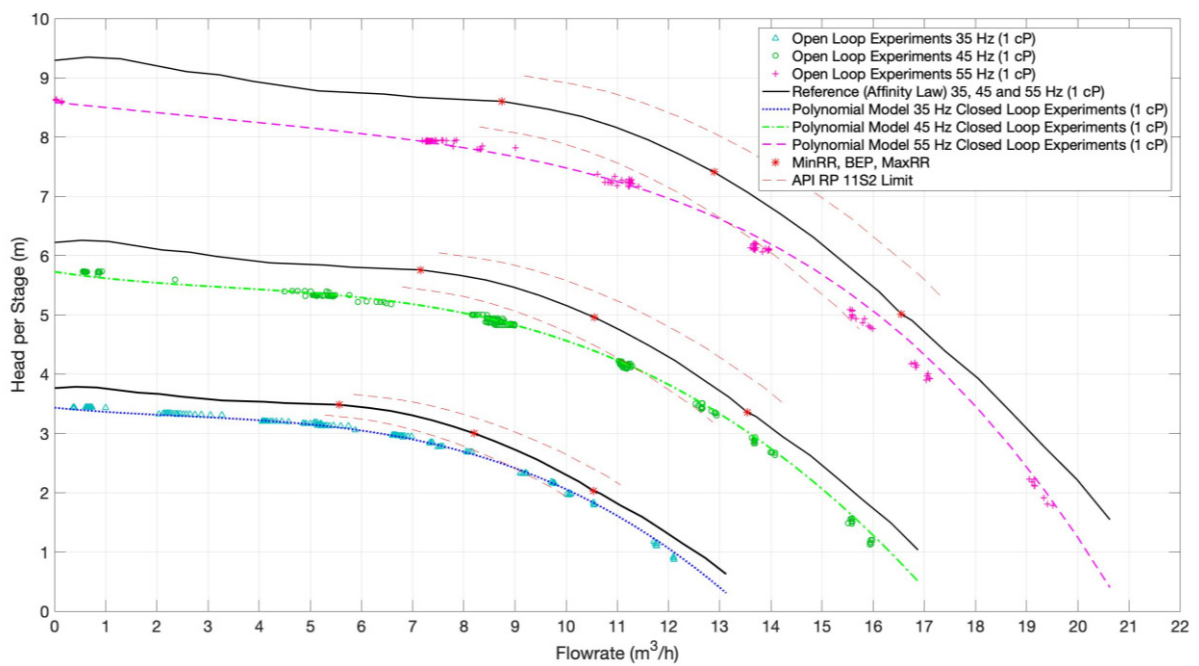


Figure 77: REDA D2100EZ Head Curve – 35, 45 and 55 Hz Open Loop Experiments compared with Closed Loop Polynomial Fits using Water as Test Fluid (1 cP and 1 S.G.)

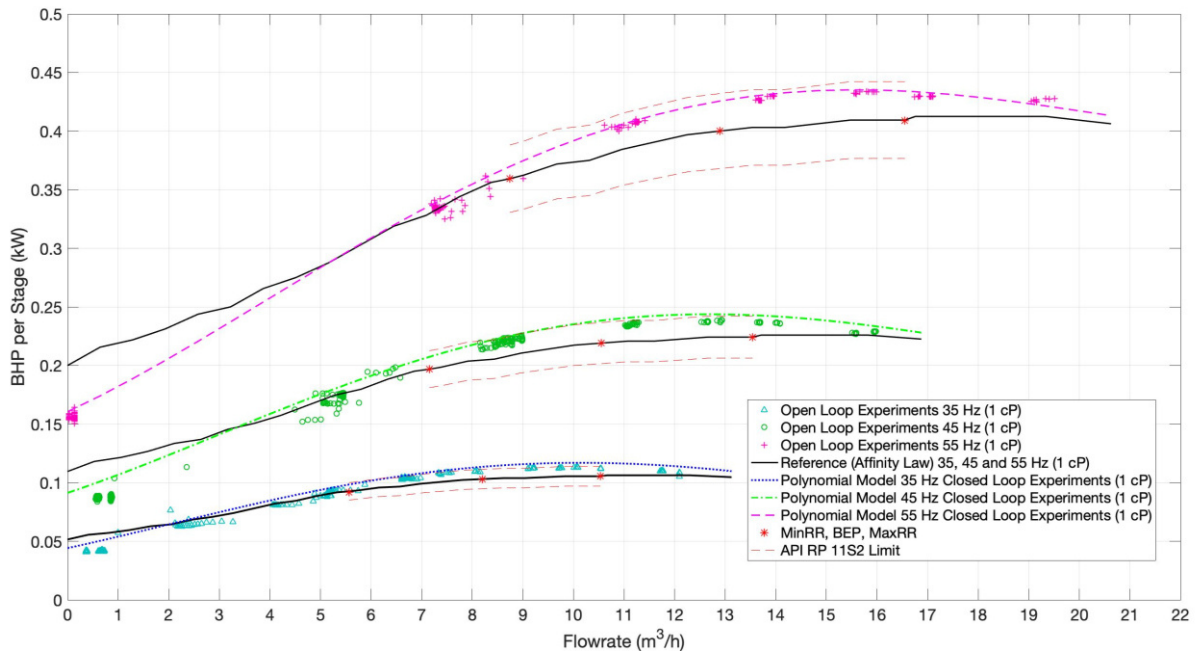


Figure 78: REDA D2100EZ Break Horsepower Curve – 35, 45 and 55 Hz Open Loop Experiments compared with Closed Loop Polynomial Fit using Water as Test Fluid (1 cP and 1.S.G)

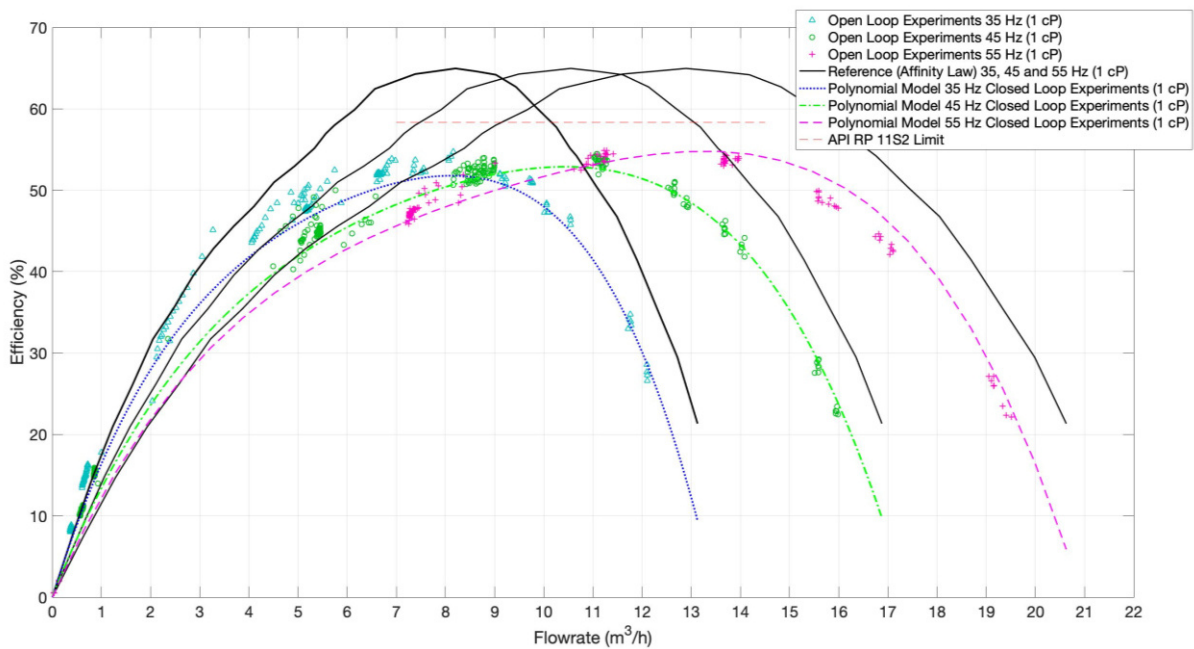


Figure 79: REDA D2100EZ Efficiency Curve – 35, 45 and 55 Hz Open Loop Experiments compared with Closed Loop Polynomial Fit using Water as Test Fluid (1 cP and 1.S.G)

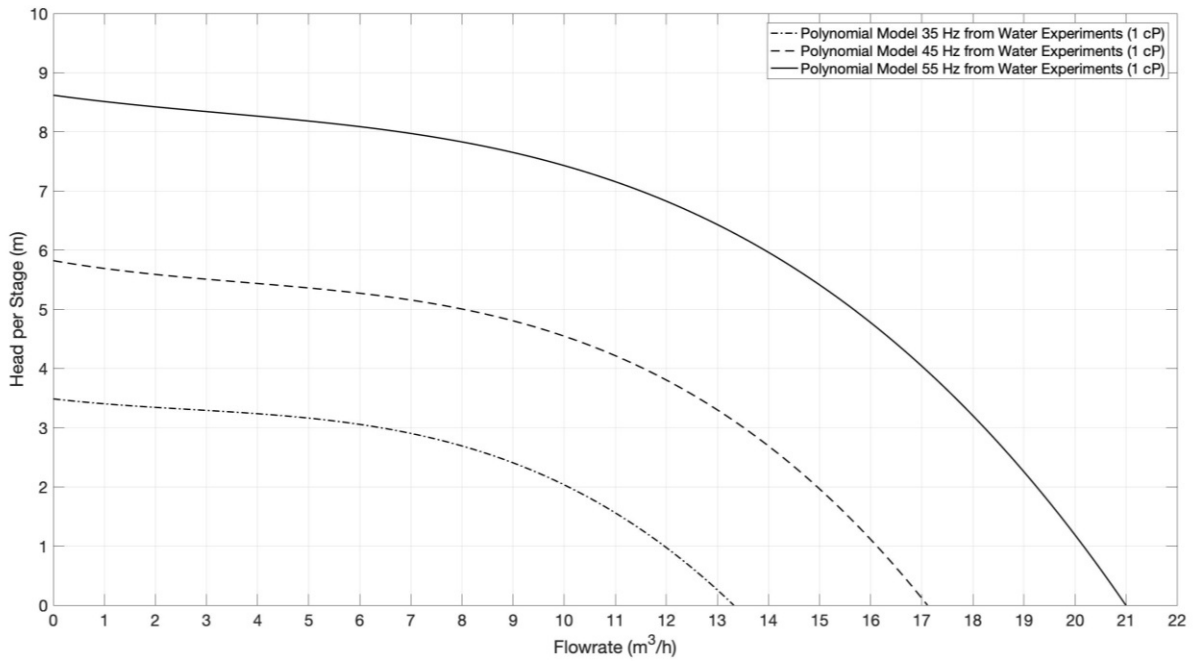


Figure 80: REDA D2100EZ 3rd order polynomial model (head) from 35, 45 and 55 Hz experiments with water (1 cP and 1 S.G.)

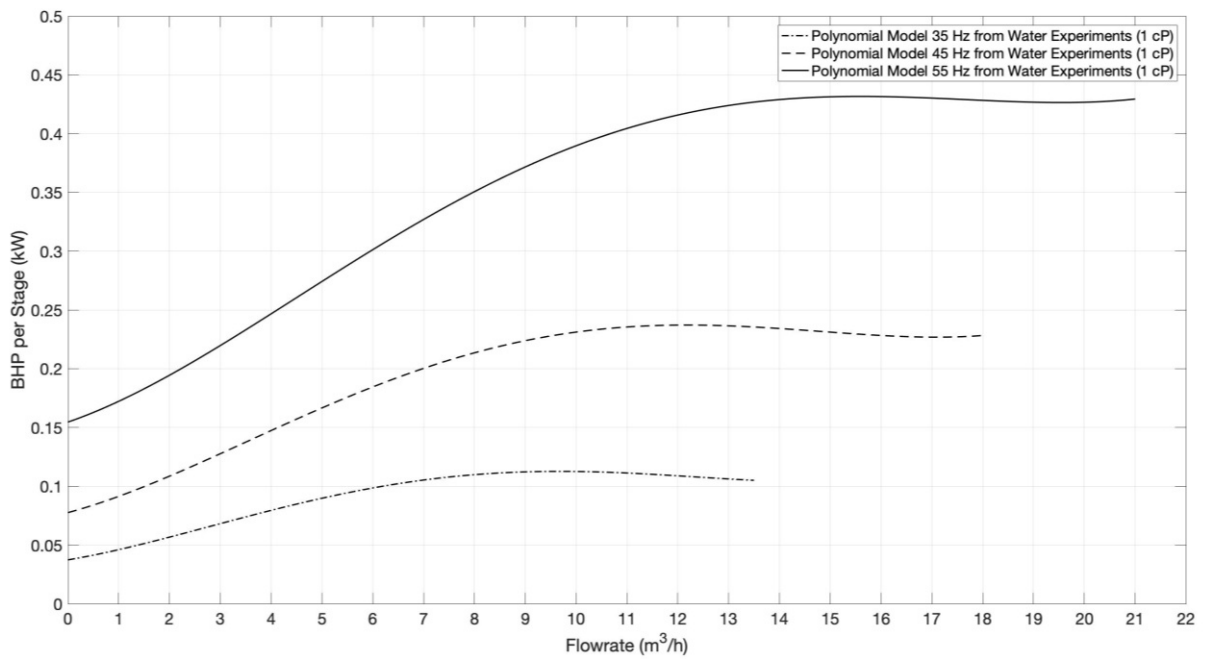


Figure 81: REDA D2100EZ 4th order polynomial model (brake horsepower) from 35, 45 and 55 Hz experiments with water (1 cP and 1 S.G.)

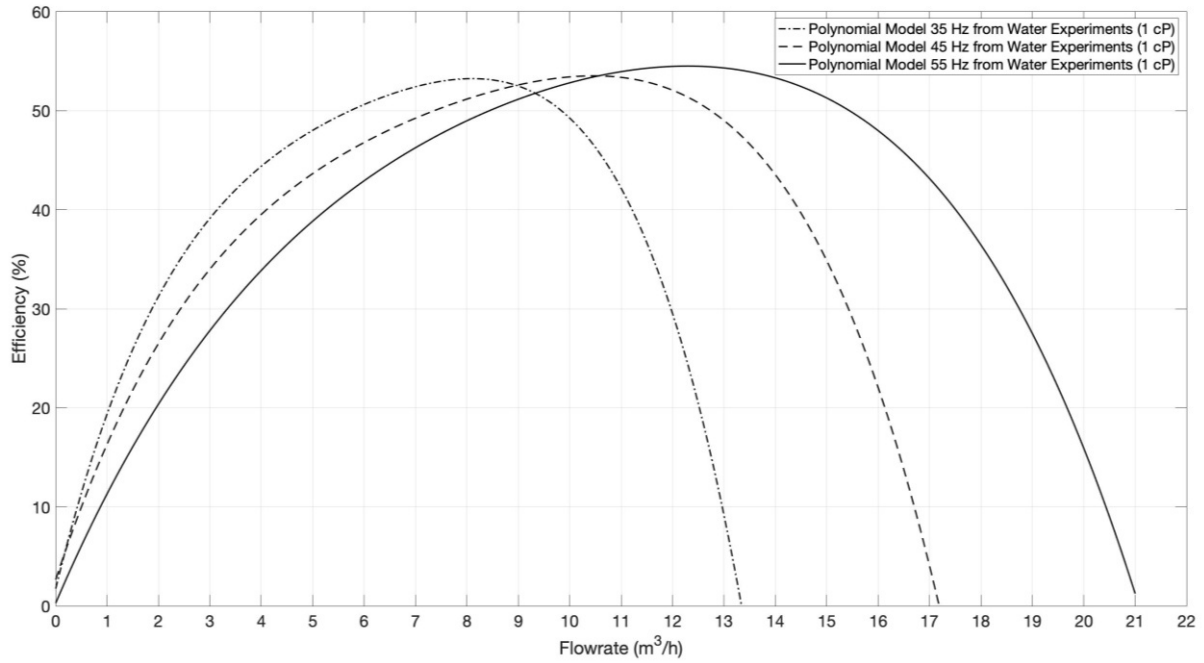


Figure 82: REDA D2100EZ Polynomial Model (Efficiency) from 35, 45 and 55 Hz Experiments with Water (1 cP and 1 S.G.)

REDA D2400N water performance plots:

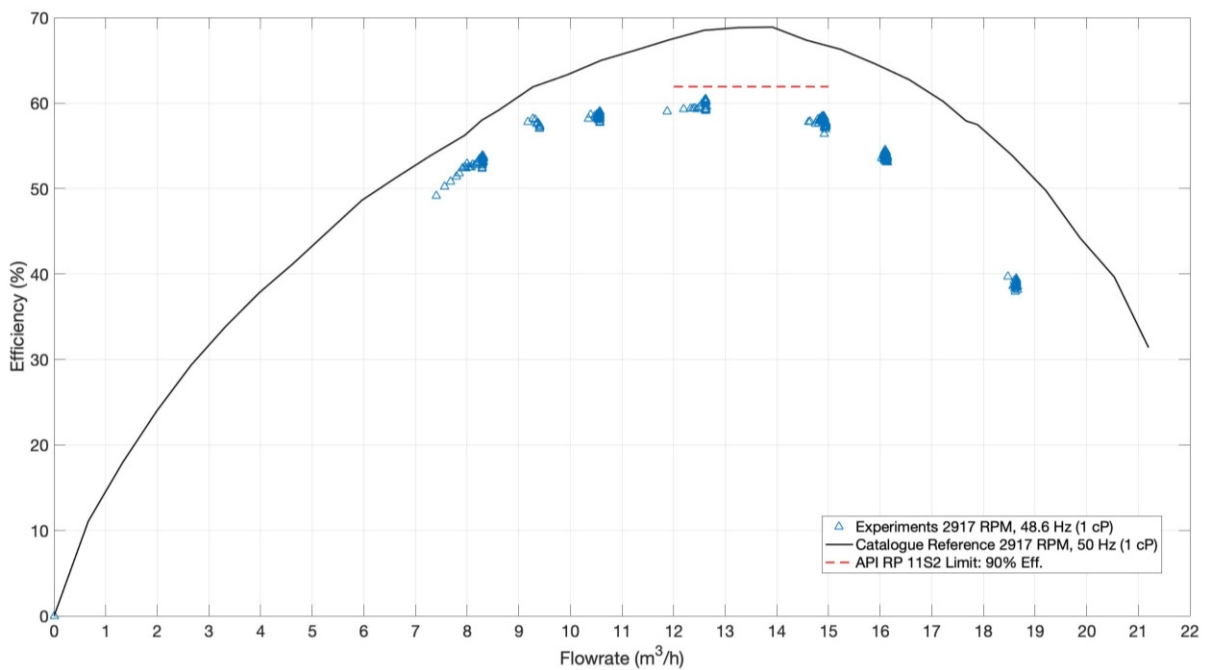


Figure 83: REDA D2400N Efficiency Curve – Catalogue versus 2917 RPM Closed Loop Experiments with Water (1 cP and 1 S.G.)

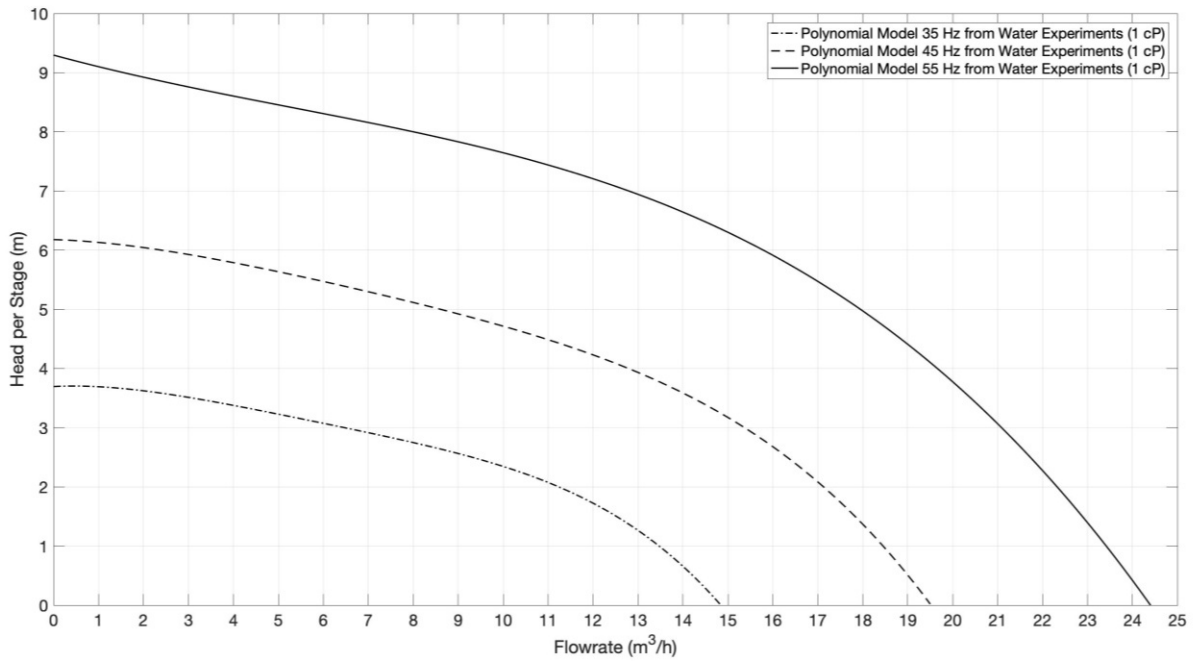


Figure 84: REDA D2100EZ 4th order polynomial model (head) from 35, 45 and 55 Hz experiments with water (1 cP and 1 S.G.)

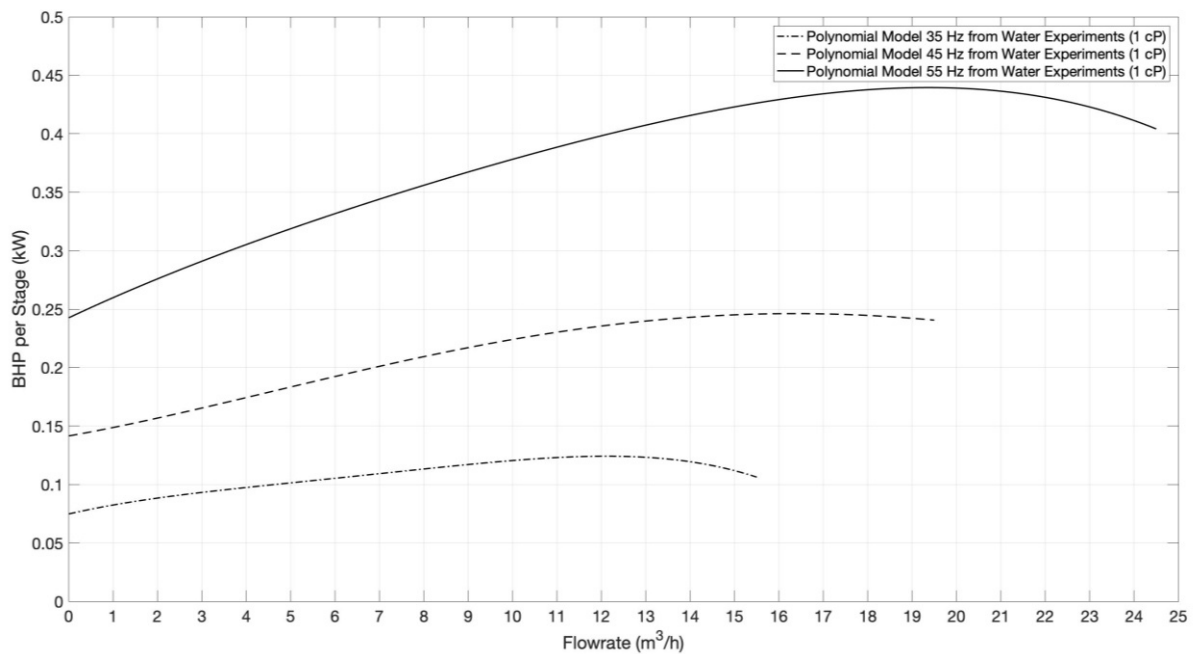


Figure 85: REDA D2100EZ 4th order polynomial model (brake horsepower) from 35, 45 and 55 Hz experiments with water (1 cP and 1 S.G.)

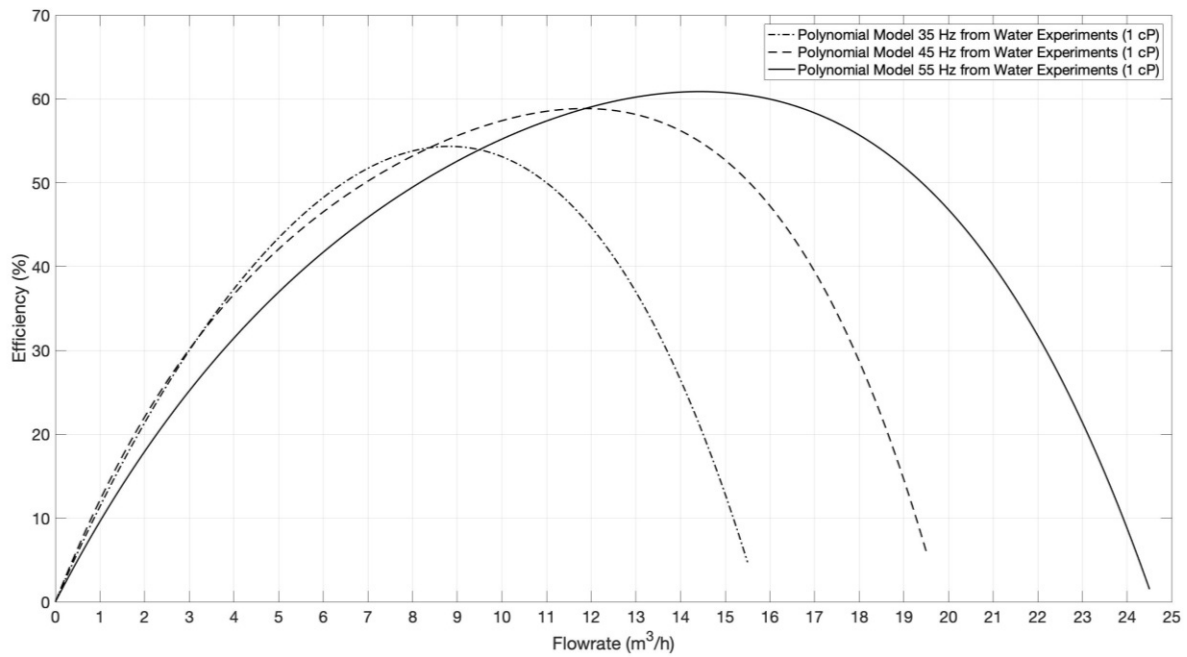


Figure 86: REDA D2400N Polynomial Model (Efficiency) from 35, 45 and 55 Hz Experiments with Water (1 cP and 1 S.G.)

REDA D2100EZ viscous (polymer) performance plots:

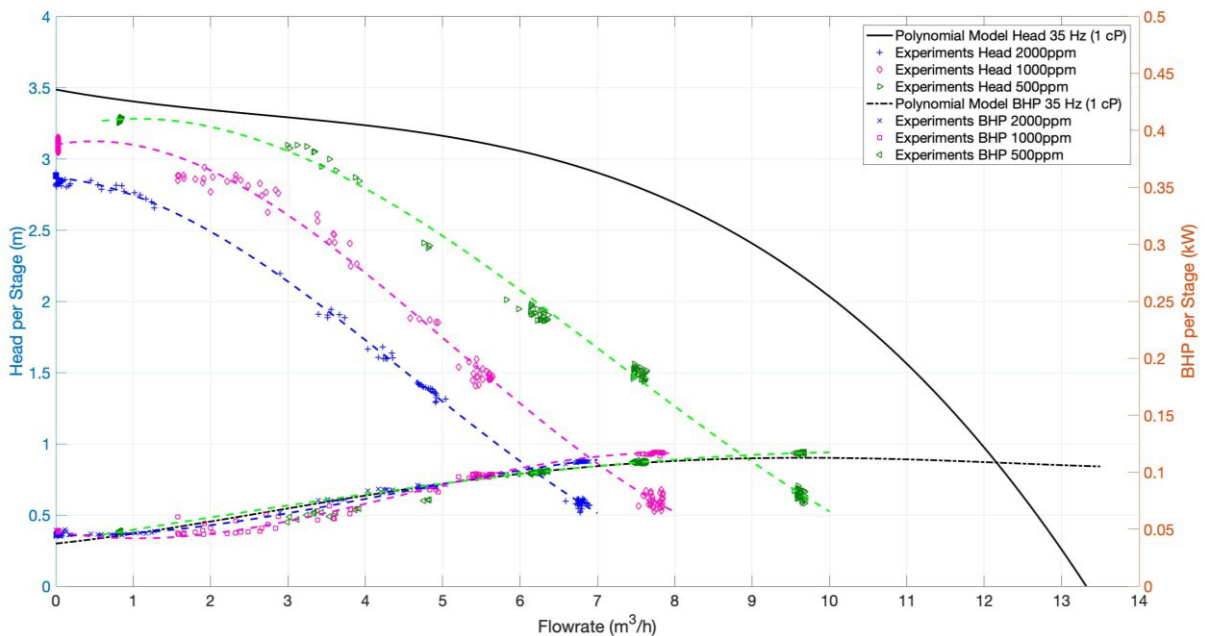


Figure 87: REDA D2100EZ head and brake horsepower curve – 35 Hz polynomial model (water, 1 cP and 1 S.G.) versus polymeric fluid performance (2000 ppm at 25°C)

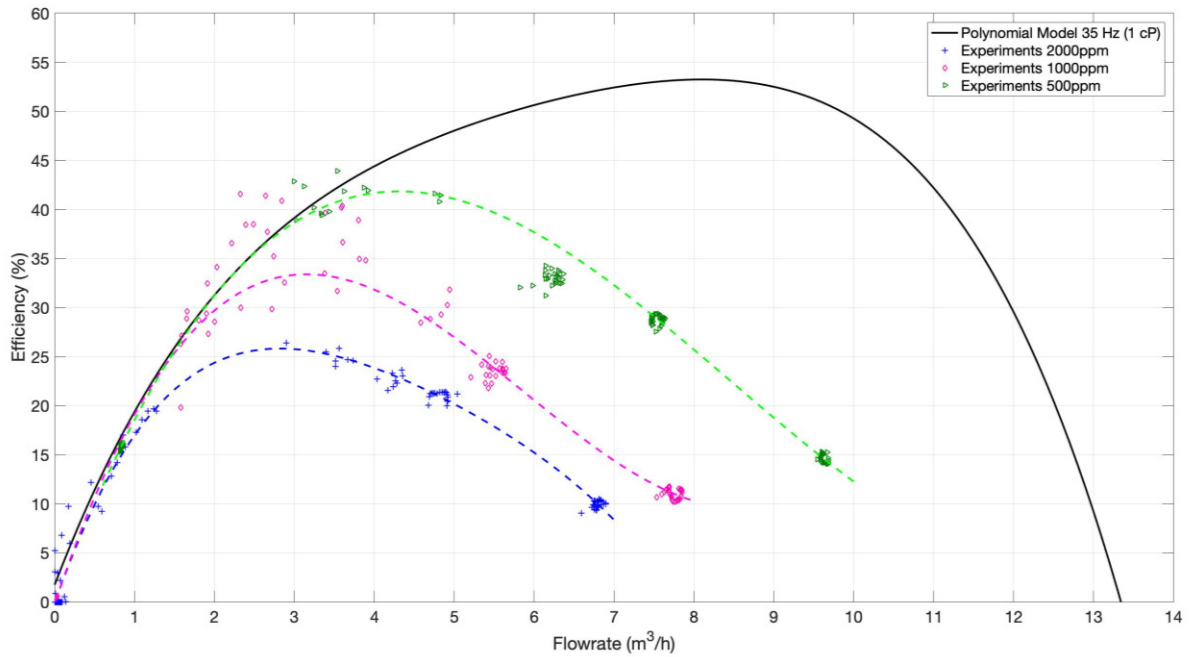


Figure 88: REDA D2100EZ efficiency curve – 35 Hz polynomial model (water, 1 cP and 1 S.G.) versus polymeric fluid performance (2000 ppm at 25°C)

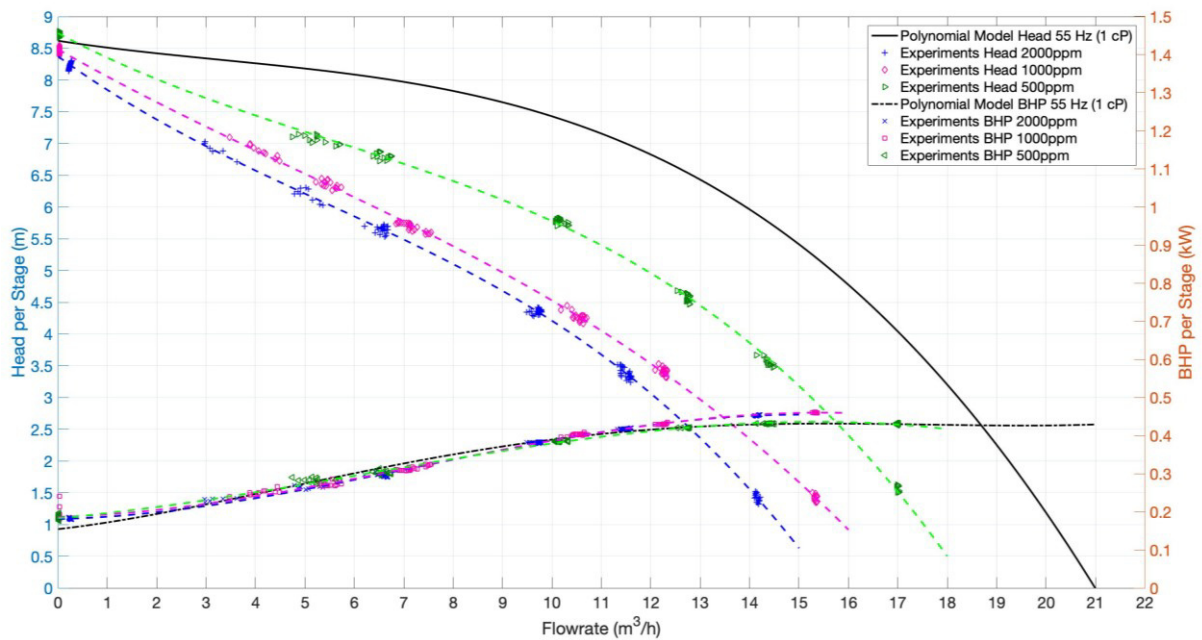


Figure 89: REDA D2100EZ head and brake horsepower curve – 55 Hz polynomial model (water, 1 cP and 1 S.G.) versus polymeric fluid performance (2000 ppm at 30°C)

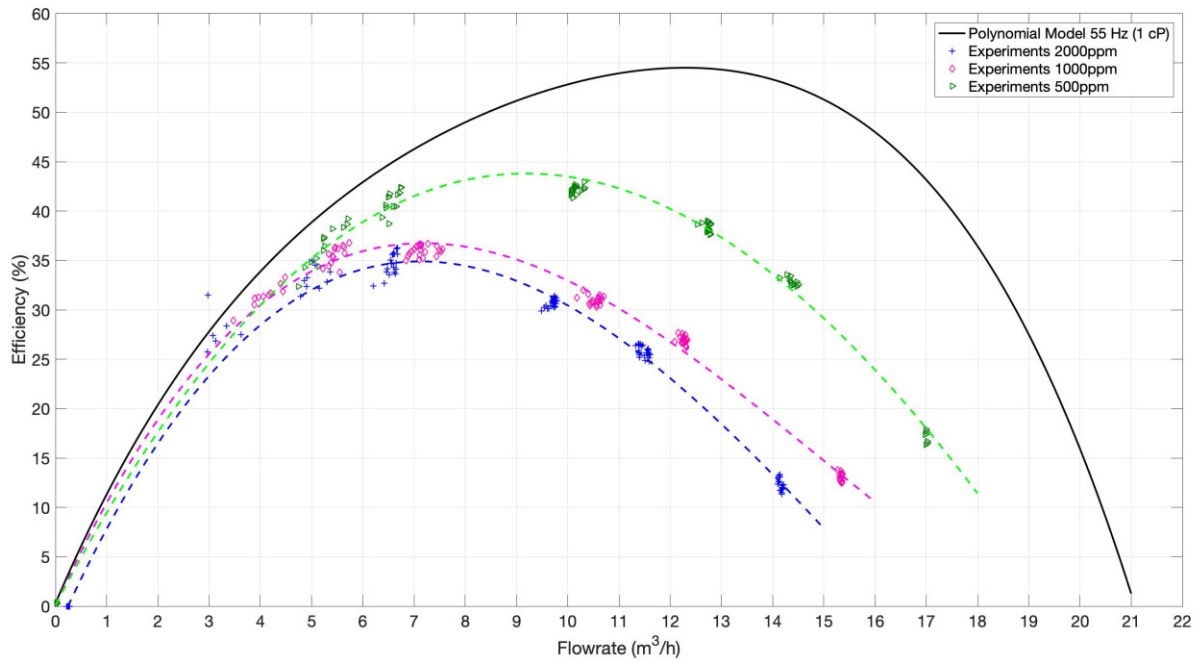


Figure 90: REDA D2100EZ efficiency curve – 55 Hz polynomial model (water, 1 cP and 1 S.G.) versus polymeric fluid performance (2000 ppm at 30°C)

REDA D2400N viscous (polymer) performance plots:

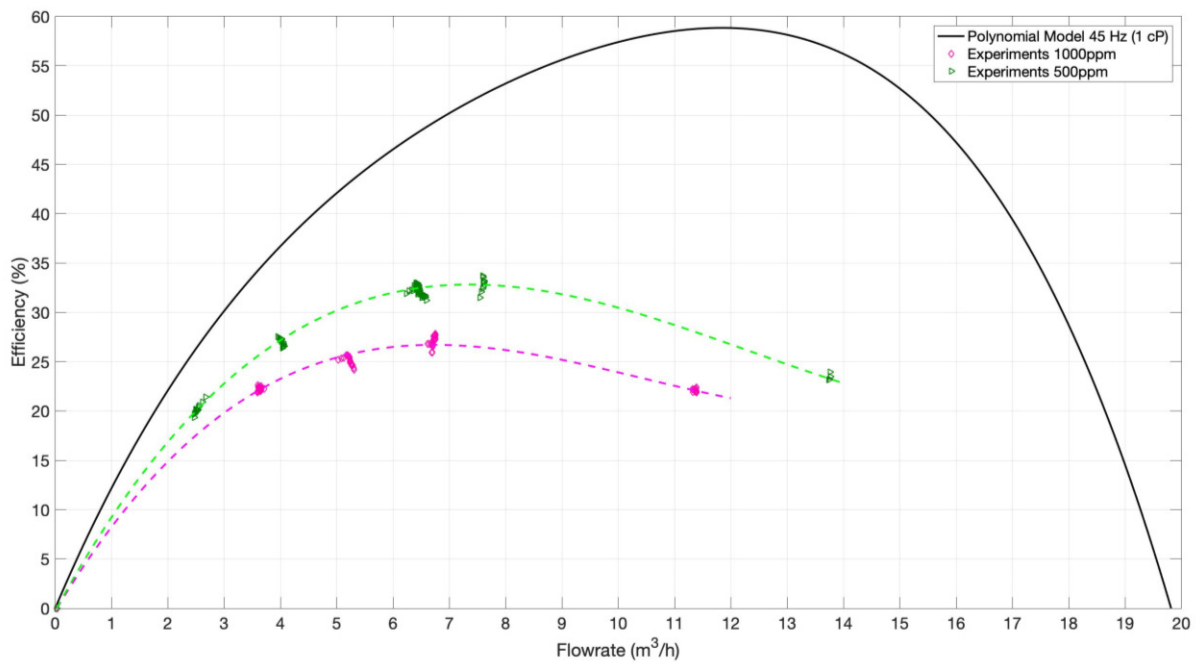


Figure 91: REDA D2400N efficiency curve – 45 Hz polynomial model (water, 1 cP and 1 S.G.) versus polymeric fluid performance

REDA D2400N water and viscous performance plots after disassembling, connecting pressure sensor to each stage and reassembling:

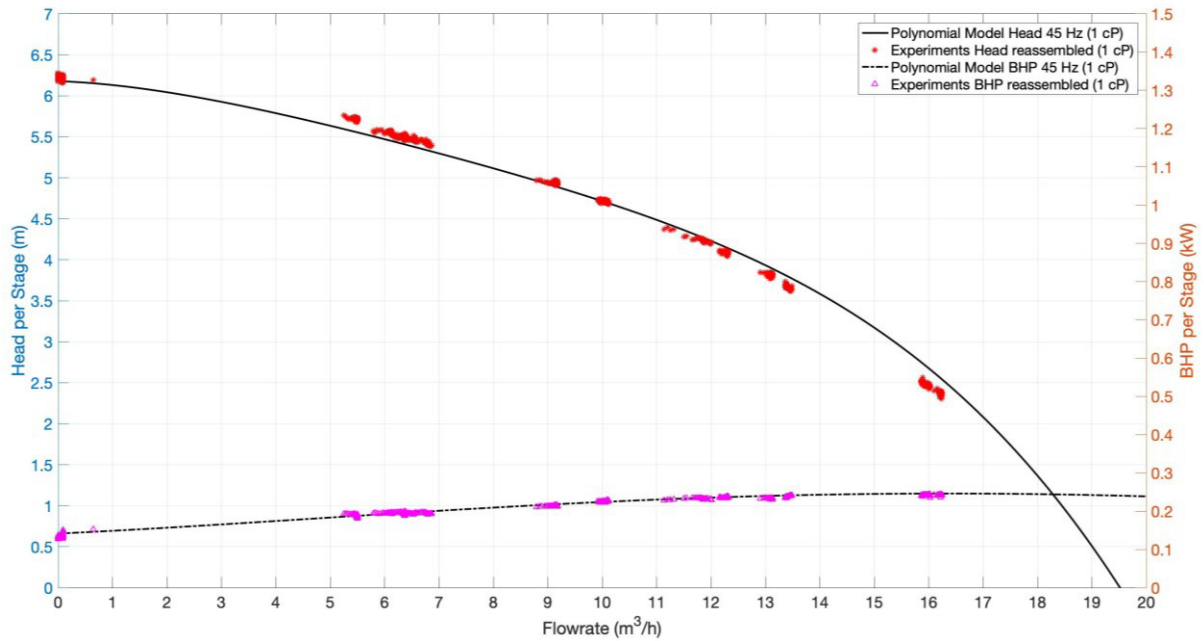


Figure 92: Reassembled REDA D2400N head and brake horsepower curve – 45 Hz test points versus initial experimental polynomial model (water, 1 cP and 1 S.G.)

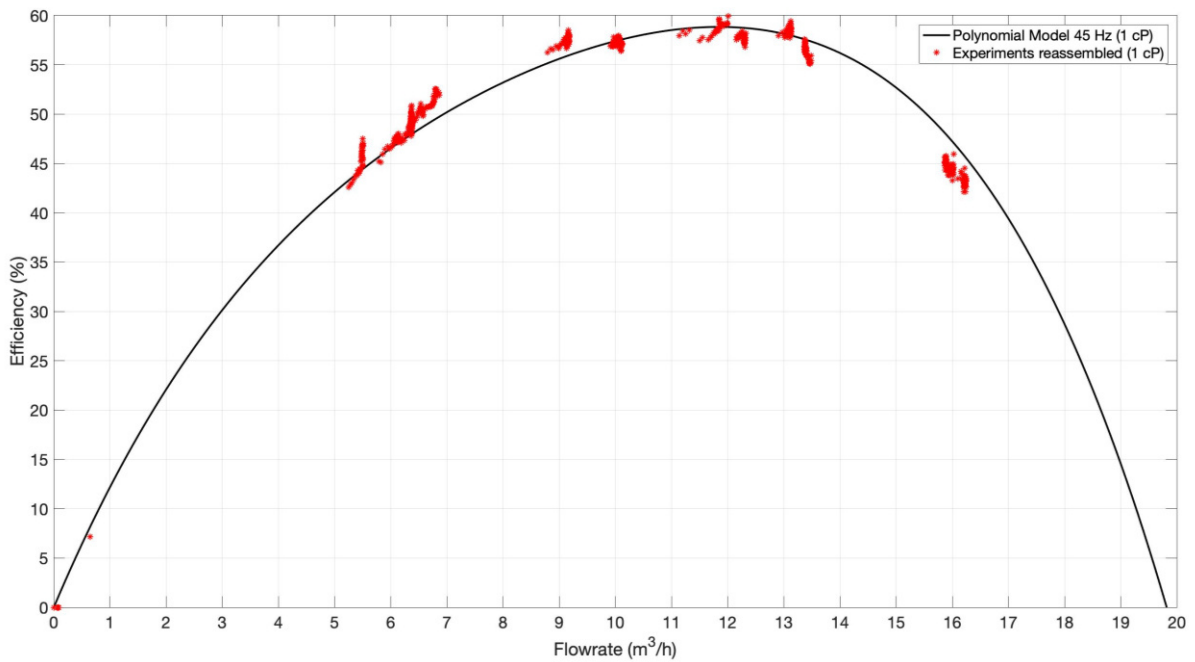


Figure 93: Reassembled REDA D2400N efficiency curve – 45 Hz test points versus initial experimental polynomial model (water, 1 cP and 1 S.G.)

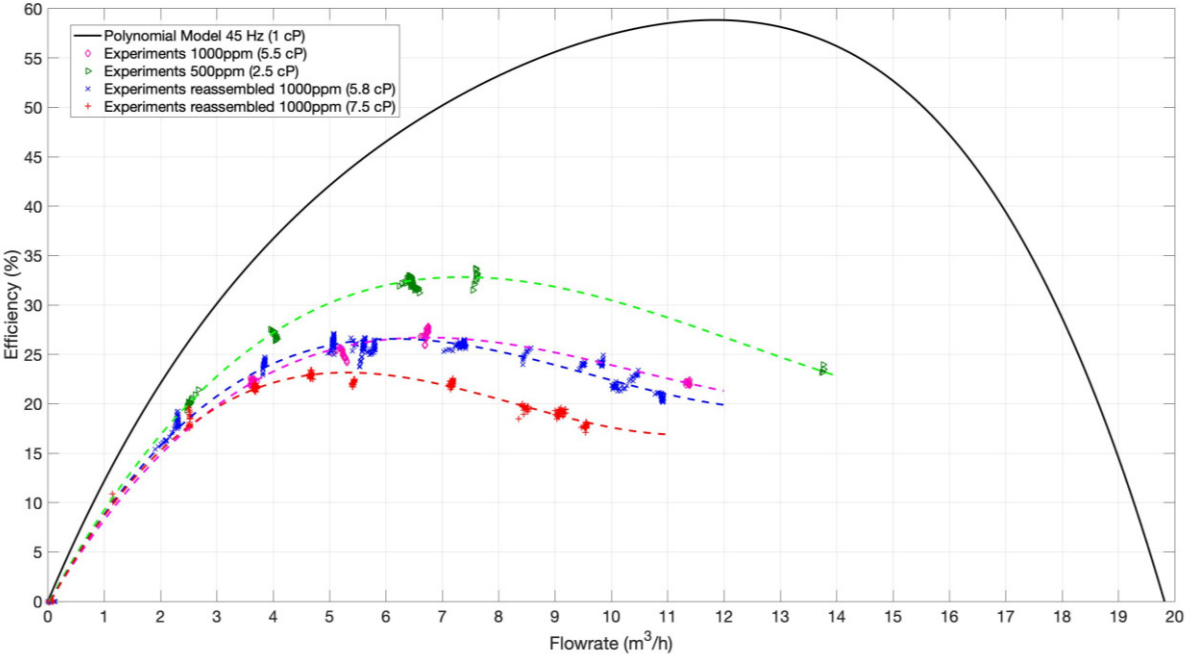


Figure 94: Reassembled REDA D2400N efficiency curve – 45 Hz polynomial model (water, 1 cP and 1 S.G.) versus polymeric fluid performance

Appendix D – Rheology Measurements

First polymer delivery: On-site Brookfield viscometer measurements after mixing and during the viscous pump tests:

- Measured by an OMV Employer using a Brookfield viscometer (2 and 3 July 2019)
- Additionally measured with an Anton Paar rheometer in the PCCL lab

ESP - Polymer Scherversuch UNI Leoben						
Abfüllung 26.06.2019						
				Viskosität [broofield Spindel LV#62] [cps]	Konzentration	Viskosität [30°C/6rpm] [cps]
Mothersolution	maturation tank	11500ppm		3800	MUL IBC#1	500ppm 2,5
Mothersolution	IBC für Abfüllung	11500ppm		3050	MUL IBC#2	500ppm 2,5
					MUL IBC#3	1000ppm 5,5
					MUL IBC#4	1000ppm 5,5
					MUL IBC#5	2000ppm 16,0
					MUL IBC#6	2000ppm 16,0
ESP Pumpversuche MUL 02./03.07.2019						
Datum	Uhrzeit	Bezeichnung	Probennummer	BROOKFIELD UL- Adapter Viskosität [30°C, 6rpm] [cps]		
02.07.2019	09:00	IBC # 5		11,0	Umfüllen der 2000ppm Polymerlösung in Vorlagetank der Testanlage	
02.07.2019	09:30	IBC # 6		11,0	Umfüllen der 2000ppm Polymerlösung in Vorlagetank der Testanlage	
02.07.2019	10:42	min RR	1	7,0	1. TESTLAUF ESP mit 35 Hz 2000ppm Polymer	
02.07.2019	10:45	BEP	2	7,5	1. TESTLAUF ESP mit 35 Hz 2000ppm Polymer	
02.07.2019	11:05	min RR	3	8,3	2. TESTLAUF ESP mit 45 Hz 2000ppm Polymer	
02.07.2019	11:06	BEP	4	7,0	2. TESTLAUF ESP mit 45 Hz 2000ppm Polymer	
02.07.2019	11:23	min RR	5	6,0	3. TESTLAUF ESP mit 55 Hz 2000ppm Polymer	
02.07.2019	11:24	BEP	6	6,5	3. TESTLAUF ESP mit 55 Hz 2000ppm Polymer	
02.07.2019	11:35	Vorlagetank	7	8,2	Vorlagetank 50°C für ca. 3h	
02.07.2019	Vorlagetank Inhalt gegen Wasser ausgetauscht alte 2000ppm Polymerlösung in IBC's abgelassen					
02.07.2019	TESTLAUF mit Wasser bei ESP 35Hz (ident mit Wasser-Testläufen bisher)					
02.07.2019	Mischung aus 800 Liter 2000ppm Lösung (1xTank) + 500 Liter 2000ppm NEU Mischung gesamt 1300Liter					
02.07.2019	15:17	min RR	8	9,0	4. TESTLAUF ESP mit 35 Hz 2000ppm Polymer	
02.07.2019	15:19	BEP	9	8,0	4. TESTLAUF ESP mit 35 Hz 2000ppm Polymer	
02.07.2019	15:27	min RR	10	6,2	5. TESTLAUF ESP mit 45 Hz 2000ppm Polymer	
02.07.2019	15:29	BEP	11	7,0	5. TESTLAUF ESP mit 45 Hz 2000ppm Polymer	
02.07.2019	15:32	Vorlagetank	14	7,5	Vorlagetank zwischen TESTLAUF #5 und #6	
02.07.2019	15:36	min RR	12	5,5	6. TESTLAUF ESP mit 55 Hz 2000ppm Polymer	
02.07.2019	15:38	BEP	13	6,5	6. TESTLAUF ESP mit 55 Hz 2000ppm Polymer	
02.07.2019	15:50	Vorlagetank	15	7,0	Vorlagetank nach TESTLAUF #6	
03.07.2019	08:00	IBC # 1	16	2,2	Umfüllen der 500ppm Polymerlösung in Vorlagetank	
03.07.2019	08:00	IBC # 2	17	2,2	Umfüllen der 500ppm Polymerlösung in Vorlagetank	
03.07.2019	09:15	Vorlagetank	18	2,1	Vorlagetank vor START TESTLAUF #7	
03.07.2019	09:45	BEP	19	1,9	7. TESTLAUF ESP mit 35 Hz 500ppm Polymer	
03.07.2019	09:53	min RR	20	1,5	8. TESTLAUF ESP mit 45 Hz 500ppm Polymer	
03.07.2019	09:55	BEP	21	1,6	8. TESTLAUF ESP mit 45 Hz 500ppm Polymer	
03.07.2019	10:05	Vorlagetank	23	1,6	Vorlagetank vor START TESTLAUF #9	
03.07.2019	10:15	BEP	22	1,5	9. TESTLAUF ESP mit 55 Hz 500ppm Polymer	
03.07.2019	11:00	IBC # 3	24	3,6	Umfüllen der 1000ppm Polymerlösung in Vorlagetank	
03.07.2019	11:00	IBC # 4	25	4,0	Umfüllen der 1000ppm Polymerlösung in Vorlagetank	
03.07.2019	12:00	Vorlagetank	26	3,9	Vorlagetank vor TESTLAUF #10 1000ppm Polymer	
03.07.2019	12:06	min RR	27	3,0	10. TESTLAUF ESP mit 35 Hz 1000ppm Polymer	
03.07.2019	12:07	BEP	28	3,0	10. TESTLAUF ESP mit 35 Hz 1000ppm Polymer	
03.07.2019	12:14	min RR	29	3,0	11. TESTLAUF ESP mit 45 Hz 1000ppm Polymer	
03.07.2019	12:15	BEP	30	3,0	11. TESTLAUF ESP mit 45 Hz 1000ppm Polymer	
03.07.2019	12:26	BEP	31	2,6	12. TESTLAUF ESP mit 55 Hz 1000ppm Polymer	
03.07.2019	12:45	Vorlagetank	32	3,5	Vorlagetank nach TESTLAUF #12	

Second polymer delivery – Viscosity measurement in Gänserndorf after mixing:

- Fluids for the 7-stage pump tests with pressure sensor drilled into each stage

ESP - Polymer Scherversuch UNI Leoben		
Abfüllung 13.08.2019		
Viscometer: Brookfield	Konzentration	Viskosität [30°C/6rpm] [cps]
MUL IBC#1	1000ppm	7,5
MUL IBC#2	1000ppm	5,8

Laboratory (PCCL) Anton Paar Physica MCR501 rheometer viscosity measurements:

- Last rheometer calibration date: 2 July 2019
- Viscosity measurement dates: 4 and 5 July 2019
- Measured shear rates: 1 – 1000 1/s
- Measuring temperature: test temperatures
- Number of test points: 20
- Measuring system: Double-gap measuring systems (according to DIN 54453)

Double-gap measuring systems according to DIN 54453 (Anton Paar Wiki):

- For samples with very low viscosities (water-like), below 10mPas
- DG26.7, gap size = 0.4mm

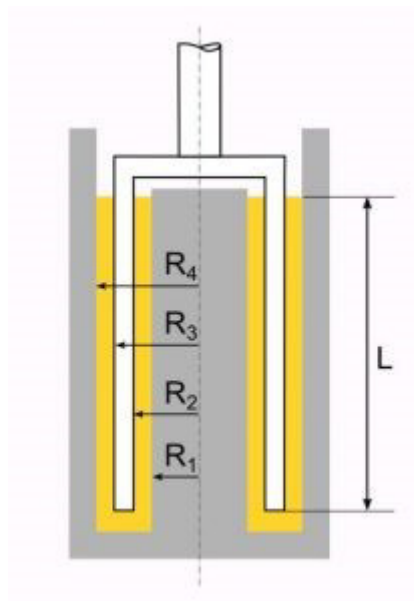


Figure 95: Double-gap measuring systems¹

¹ Anton Paar Wiki. How to measure viscosity. [online] URL: <https://wiki.anton-paar.com/en/how-to-measure-viscosity/>.

First polymer delivery – Anton Paar rheometer measurements on the 4 and 5 July:

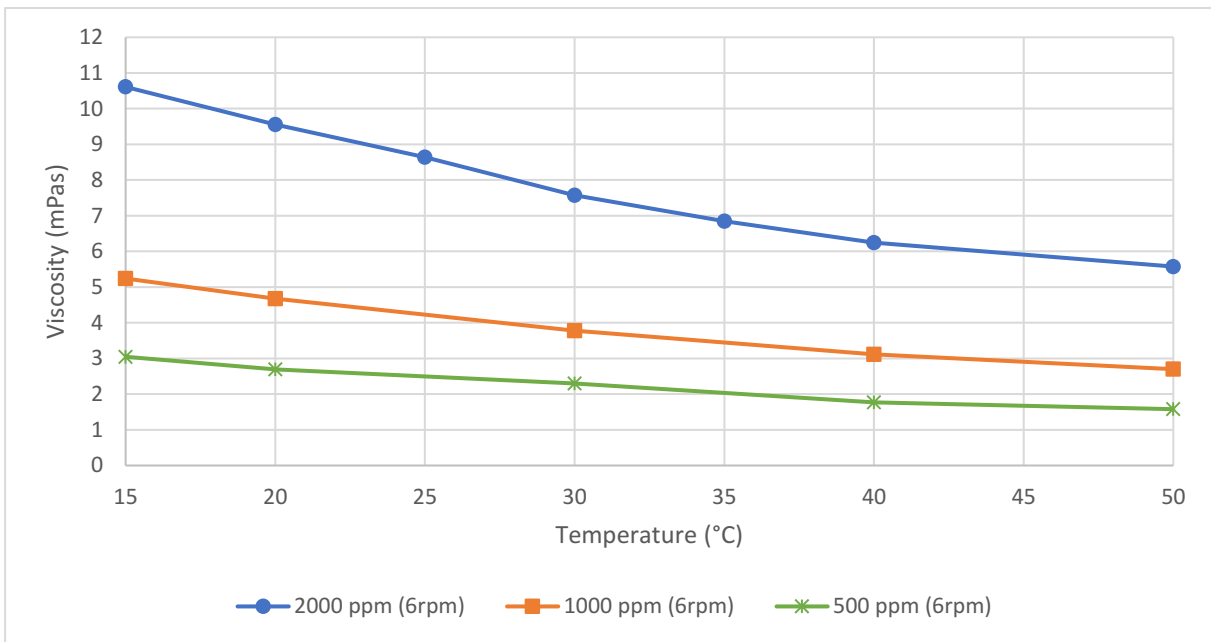


Figure 96: Temperature profile of the three polymer concentrations at 6 rpm

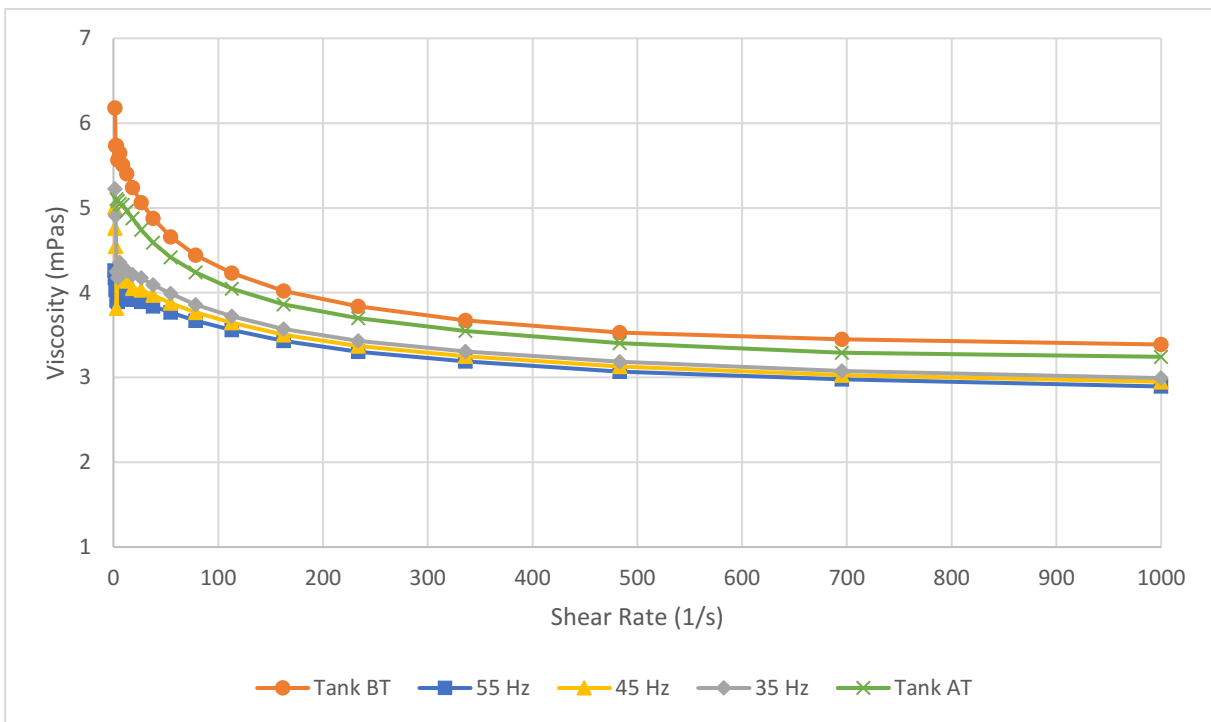


Figure 97: Viscosity profile of the 1000-ppm fluid samples at 15 °C (REDA D2100EZ tests)

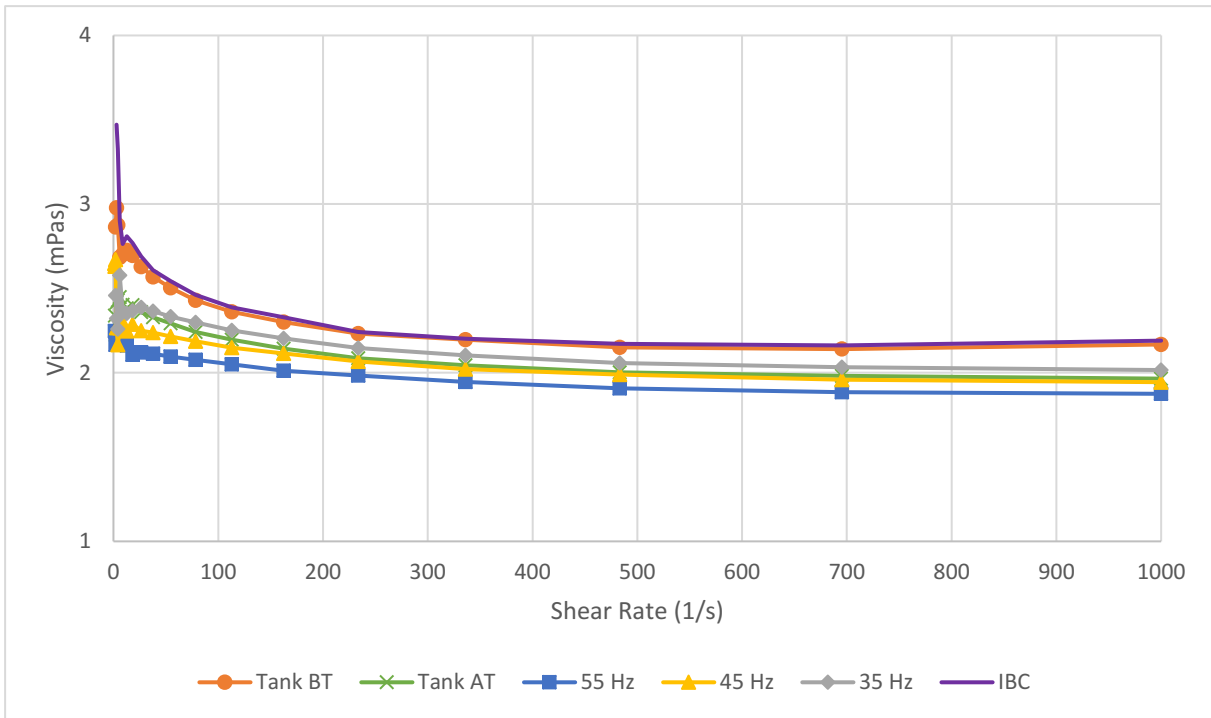


Figure 98: Viscosity profile of the 500-ppm fluid samples at 20 °C (REDA D2100EZ tests)

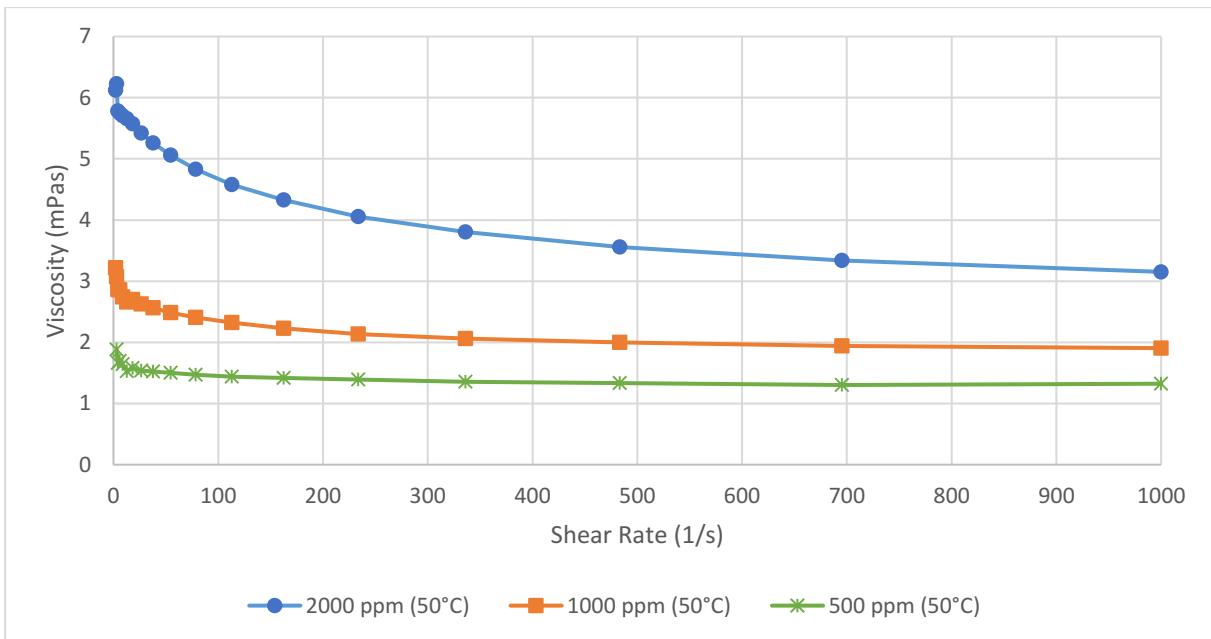


Figure 99: Viscosity profile for each polymer (HPAM) concentration at 50 °C (sample from the pressure tank prior to each test), REDA D2100EZ experiments

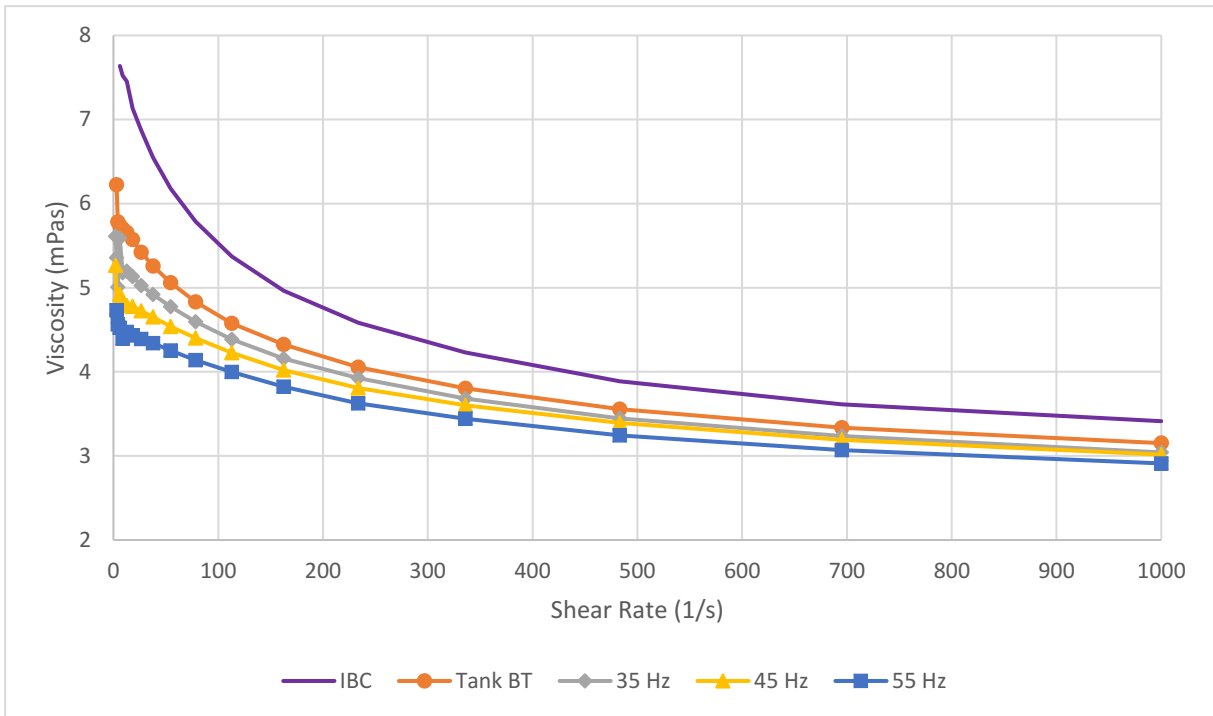


Figure 100: Viscosity profile of the 2000-ppm fluid samples at 50 °C (REDA D2100EZ tests)

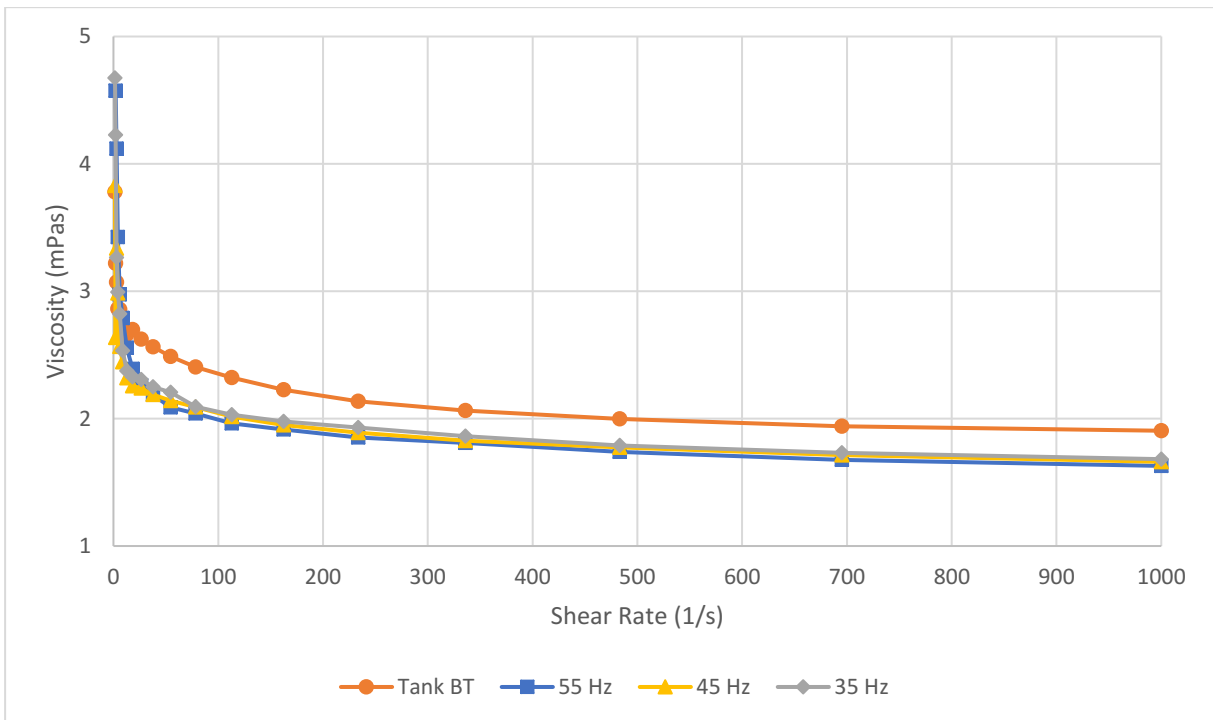


Figure 101: Viscosity profile of the 1000-ppm fluid samples at 50 °C (REDA D2100EZ tests)

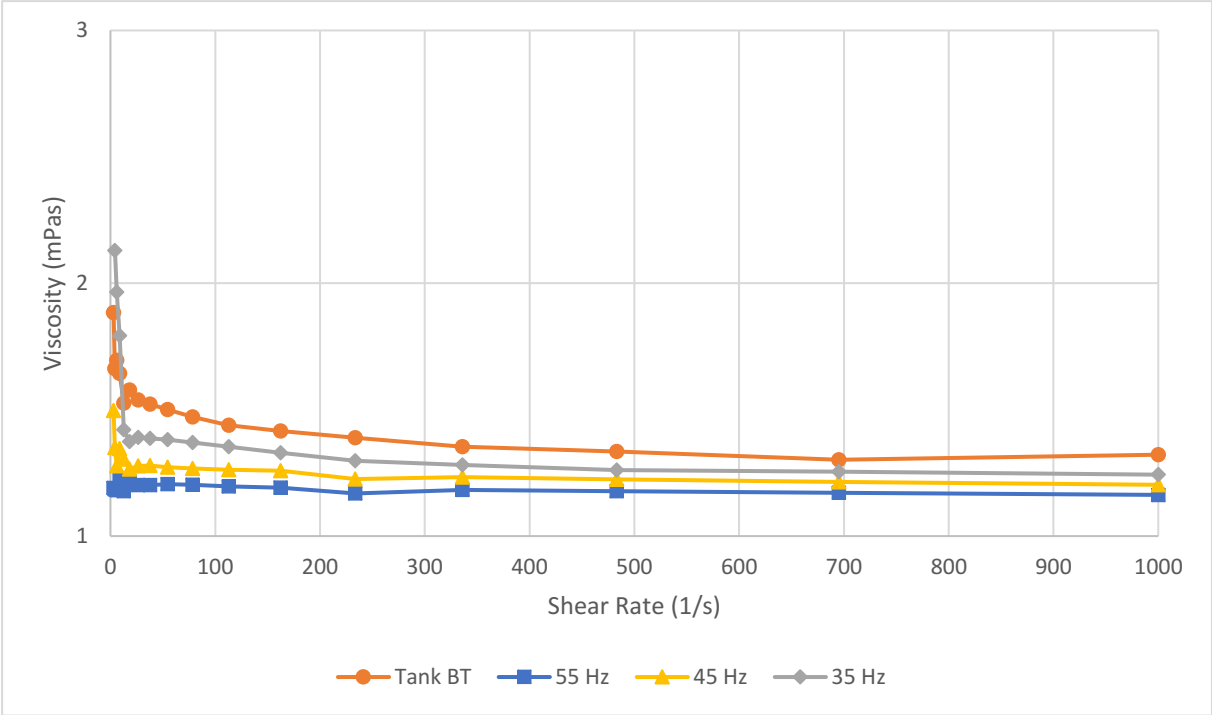


Figure 102: Viscosity profile of the 500-ppm fluid samples at 50 °C (REDA D2100EZ tests)

Appendix E – Polymer Solution Preparation and Transport

The polymer solutions were prepared on June 26, 2019 in Gänserndorf at the polymer flooding plant. First, a mother solution with 11,500 ppm from the plant's maturation tank was filled into an IBC (1000-liter container). During the decanting process, the solution degraded from 3,800 to 3,050 cP (Brookfield, 6 rpm at 30 °C). Next, the 11,500 ppm solution was diluted with artificially made 3%-KCl brine. For each concentration (500/1,000/2,000ppm), two 1000-liter tanks were prepared. The measured viscosities are shown in Appendix D. It should be mentioned that the day of mixing was very hot, between 35 and 40 °C.

On June 27, 2019, a carrier picked up all six containers and shipped them to Leoben. The carrier had one overnight stop. Due to the hot summer days, it is possible that it had up to 60 °C inside the shipping space during the transport. On June 28, 2019, the IBCs arrived in Leoben at the IZR building. The containers were brought in the basement, where the temperature is about 15 to 20°C. There they were stored until the pump experiments started, which was July 2, 2019.

Appendix F – Pump Testing Table

The pneumatic control valve was mainly regulated via the D104 pressure sensor (IST/SOLL), expect it is said to be different in the additional notes.

Table 20: REDA D2100EZ Experiments

	Test Fluid	Test Loop	Frequ.	Intake Press.	Additional Notes	Date	Time
1	Water	Closed	35 Hz	5 bar	D107 control	22.05.2019	13:22-13:29
2	Water	Closed	35 Hz	5 bar	D107 control	22.05.2019	13:33-13:39
3	Water	Closed	45 Hz	5 bar	D107 control	22.05.2019	13:42-13:49
4	Water	Closed	35 Hz	10 bar	D107 control	22.05.2019	13:54-14:00
5	Water	Closed	35 Hz	10 bar	D107 control	22.05.2019	14:11-14:16
6	Water	Closed	45 Hz	10 bar	D107 control	22.05.2019	14:02-14:09
7	Water	Closed	35 Hz	15 bar	D107 control	22.05.2019	14:21-14:27
8	Water	Closed	45 Hz	15 bar	D107 control	22.05.2019	14:28-14:35
9	Water	Closed	35 Hz	5 bar		22.05.2019	15:20-15:26
10	Water	Closed	35 Hz	10 bar		22.05.2019	15:05-15:11
11	Water	Closed	45 Hz	10 bar		22.05.2019	15:12-15:17
12	Water	Closed	35 Hz	15 bar		22.05.2019	14:51-14:57
13	Water	Closed	45 Hz	15 bar		22.05.2019	14:58-15:04
14	Water	Closed	35 Hz	5 bar		29.05.2019	13:29-13:35
15	Water	Closed	45 Hz	5 bar		29.05.2019	13:37-13:43
16	Water	Closed	50 Hz	5 bar		29.05.2019	14:08-14:14
17	Water	Closed	35 Hz	5 bar	With sampling	29.05.2019	14:21-14:27
18	Water	Closed	35 Hz	5 bar		11.06.2019	10:38-10:45
19	Water	Closed	45 Hz	5 bar		11.06.2019	11:09-11:15
20	Water	Closed	55 Hz	5 bar		11.06.2019	10:45-10:52
21	Water	Closed	55 Hz	10 bar		11.06.2019	10:58-11:05
22	Water	Closed	58.3 Hz	5 bar		11.06.2019	11:23-11:29
23	Water	Open	35 Hz	5 bar	First open trial	13.06.2019	10:17-10:22
24	Water	Open	45 Hz	5 bar		18.06.2019	11:19-11:25
25	Water	Open	35 Hz	5 bar	With sampling	19.06.2019	10:31-10:36
26	Water	Open	55 Hz	5 bar	With sampling	19.06.2019	09:52-09:59
27	Water	Open	35 Hz	5 bar		25.06.2019	14:21-14:27
28	Water	Open	45 Hz	5 bar		25.06.2019	14:34-14:40
29	Water	Open	55 Hz	5 bar		25.06.2019	14:47-14:53
30	Water	Open	35 Hz	5 bar	With sampling	01.07.2019	14:40-14:45
31	Water	Open	45 Hz	5 bar	With sampling	01.07.2019	14:47-14:52
32	Water	Open	55 Hz	5 bar	With sampling	01.07.2019	14:55-15:00
33	Polymer	Open	35 Hz	5 bar	2000 ppm, initial, 25°C	02.07.2019	10:43-10:48

34	Polymer	Open	45 Hz	5 bar	2000 ppm, initial, 30°C	02.07.2019	11:04-11:10
35	Polymer	Open	55 Hz	5 bar	2000 ppm, initial, 35°C	02.07.2019	11:23-11:29
36	Polymer	Open	35 Hz	5 bar	2000 ppm, refill, 25°C	02.07.2019	15:17-15:24
37	Polymer	Open	45 Hz	5 bar	2000 ppm, refill, 25°C	02.07.2019	15:26-15:33
38	Polymer	Open	45 Hz	5 bar	2000 ppm, refill, 30°C	02.07.2019	15:51-15:58
39	Polymer	Open	55 Hz	5 bar	2000 ppm, refill, 30°C	02.07.2019	15:36-15:43
40	Polymer	Open	35 Hz	5 bar	1000 ppm, 15°C	03.07.2019	12:06-12:14
41	Polymer	Open	45 Hz	5 bar	1000 ppm, 15°C	03.07.2019	12:14-12:21
42	Polymer	Open	45 Hz	5 bar	1000 ppm, 15°C	03.07.2019	12:39-12:46
43	Polymer	Open	55 Hz	5 bar	1000 ppm, 15°C	03.07.2019	12:22-12:29
44	Polymer	Open	35 Hz	5 bar	500 ppm, 20°C	03.07.2019	09:28-09:33
45	Polymer	Open	35 Hz	5 bar	500 ppm, 20°C	03.07.2019	09:42-09:49
46	Polymer	Open	45 Hz	5 bar	500 ppm, 20°C	03.07.2019	09:53-10:00
47	Polymer	Open	55 Hz	5 bar	500 ppm, 20°C	03.07.2019	10:14-10:21
48	Water	Open	35 Hz	5 bar	Possible polymer residues	02.07.2019	13:10-13:16
49	Water	Open	45 Hz	5 bar	Possible polymer residues	03.07.2019	15:31-15:37
50	Water	Open	55 Hz	5 bar	Possible polymer residues	03.07.2019	15:37-15:43

Table 21: REDA D2400N Experiments

	Test Fluid	Test Loop	Frequ.	Intake Press.	Additional Notes	Date	Time
1	Water	Closed	35 Hz	5 bar		10.07.2019	13:47-13:53
2	Water	Closed	35 Hz	5 bar		10.07.2019	14:03-14:11
3	Water	Closed	45 Hz	5 bar		10.07.2019	13:54-14:00
4	Water	Closed	45 Hz	5 bar		10.07.2019	14:12-14:21
5	Water	Closed	45 Hz	5 bar	Not finished test	10.07.2019	14:40-14:46
6	Water	Closed	45 Hz	5 bar		10.07.2019	14:48-14:57
7	Water	Closed	48.6 Hz	5 bar		10.07.2019	14:21-14:30
8	Water	Closed	55 Hz	5 bar		10.07.2019	14:31-14:40
9	Water	Closed	45 Hz	5 bar	Tests from 200 L casing (no rust)	23.07.2019	09:23-09:27
10	Water	Closed	45 Hz	5 bar	Tests from 200 L	23.07.2019	11:56-12:00

					casing (no rust)		
11	Water	Closed	45 Hz	5 bar	Tests from 200 L casing (no rust)	23.07.2019	13:10-13:15
12	Polymer	Open	45 Hz	5 bar	1000 ppm tests from 200 L casing (no rust)	23.07.2019	15:51-15:57
13	Polymer	Open	45 Hz	5 bar	500 ppm tests from 200 L casing (no rust)	23.07.2019	16:31-16:36
14	Polymer	Open	45 Hz	5 bar	500 ppm tests from 200 L casing (no rust)	23.07.2019	17:05-17:10
15	Water	Closed	35 Hz	5 bar	Pressure measurement at each stage	20.08.2019	11:40-11:48
16	Water	Closed	35 Hz	5 bar	Pressure measurement at each stage	20.08.2019	11:56-12:05
17	Water	Closed	45 Hz	5 bar	Pressure measurement at each stage	20.08.2019	12:06-12:15
18	Water	Closed	45 Hz	5 bar	Pressure measurement at each stage	20.08.2019	12:27-12:37
19	Water	Closed	48.6 Hz	5 bar	Pressure measurement at each stage	20.08.2019	12:18-12:28
20	Polymer	Open	45 Hz	5 bar	1000 ppm (IBC2), pressure measurement at each stage	20.08.2019	16:12-16:18
21	Polymer	Open	45 Hz	5 bar	1000 ppm (IBC2), pressure measurement at each stage	20.08.2019	16:19-16:25
22	Polymer	Open	45 Hz	5 bar	1000 ppm (IBC2), pressure measurement at each stage	20.08.2019	16:29-16:37
23	Polymer	Open	45 Hz	5 bar	1000 ppm (IBC1), pressure measurement at	20.08.2019	17:47-17:55

					each stage		
24	Polymer	Open	45 Hz	5 bar	1000 ppm (IBC1), pressure measurement at each stage	20.08.2019	18:00-18:07
25	Polymer	Closed	45 Hz	5 bar	Loop circulation 1000pp (IBC1) at a constant rate, pressure measurement at each stage	20.08.2019	19:01-19:45